Fast contact line motion:

fundamentals and applications

Koen G. Winkels

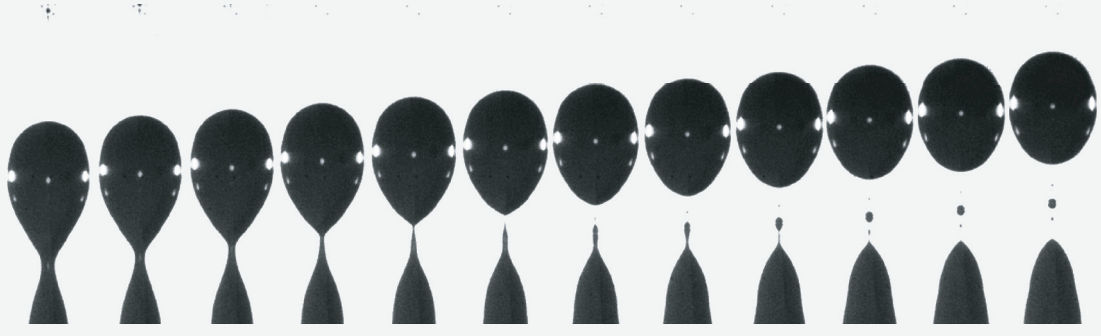

Fast contact line motion: fundamentals and applications

Koen G. Winkels

Samenstelling promotiecommissie:

Prof. dr. G. van der Steenhoven (voorzitter)	Universiteit Twente
Prof. dr. rer. nat. D. Lohse (promotor)	Universiteit Twente
Dr. J. H. Snoeijer (assistent-promotor)	Universiteit Twente
Prof. dr. L. Limat	Université Paris 7 Diderot
Prof. dr. A. A. Darhuber	Technische Universiteit Eindhoven
Prof. dr. J.P.H. Benschop	Universiteit Twente & ASML
Prof. dr. R.M. van der Meer	Universiteit Twente
Dr. R. Badie	ASML

The work in this thesis was carried out at the Physics of Fluids group of the Faculty of Science and Technology of the University of Twente. It is part of the research programme 'Contact Line Control during Wetting and Dewetting' (CLC) of the 'Stichting voor Fundamenteel Onderzoek der Materie (FOM)', which is financially supported by the 'Nederlandse Organisatie voor Wetenschappelijk Onderzoek (NWO)'. The CLC programme is cofinanced by ASML and Océ.

Nederlandse titel:
Snel bewegende contactlijnen.

Publisher:
Koen G. Winkels, Physics of Fluids, University of Twente,
P.O. Box 217, 7500 AE Enschede, The Netherlands
pof.tnw.utwente.nl

© Koen G. Winkels, Enschede, The Netherlands 2013
No part of this work may be reproduced by print
photocopy or any other means without the permission
in writing from the publisher
ISBN: 978-90-365-3517-5
DOI: 10.3990/1.9789036535175

FAST CONTACT LINE MOTION: FUNDAMENTALS AND APPLICATIONS

PROEFSCHRIFT

ter verkrijging van
de graad van doctor aan de Universiteit Twente,
op gezag van de rector magnificus,
Prof. dr. H. Brinksma,
volgens besluit van het College voor Promoties
in het openbaar te verdedigen
op donderdag 14 februari 2013 om 16.45 uur

door

Koen Gerhardus Winkels
geboren op 8 juli 1984
te Warnsveld

Dit proefschrift is goedgekeurd door de promotor:

Prof. dr. rer. nat. Detlef Lohse

en de assistent-promotor:

Dr. Jacco H. Snoeijer

Contents

1 Introduction

1.1 Contact line dynamics

Wetting and dewetting phenomena are ubiquitous in every day life, such as drops sliding off a leaf (Fig. 1.1a), soaking of a sponge or wetting of the human eye. Typically these phenomena involve a contact line, i.e. the boundary where the three phases meet. Although the dynamic contact line acts down to the microscopic scale, it strongly affects the bulk hydrodynamics. The consequence is that the physics involves many length scales, from nanometer to millimeter.

A striking example illustrating the multi-scale nature of contact line dynamics emerges in the splash resulting from a sphere impacting a water surface [1, 2]. This is displayed in figure 1.1, where two snapshots are shown of such an impact of a sphere in water. Both identical spheres have a similar impact velocity and differ only in wettability by a coating on the surface of a few nanometer thick. Surprisingly, the resulting splash is completely different. For the hydrophilic sphere, only a small jet is observed and the sphere enters the water smoothly. By contrast, for the hydrophobic coated sphere, the impact is much more violent with the formation of a large air cavity behind the sphere. Additionally a large splash results at the free surface. Hence, there exist a significant coupling between several decades in scale: the wettability is determined in the range of molecular interactions, yet it controls the splashing dynamics at the centimeter scale (splash). It turns out that the critical velocity at

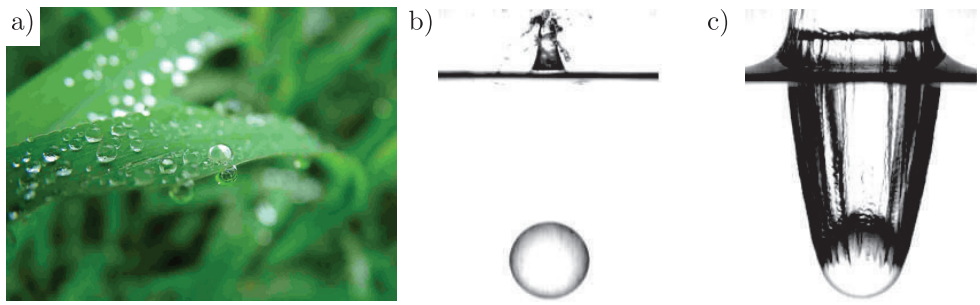

Figure 1.1: a) drop on/sliding off a leaf (adapted from Bonn et al. [8]). b-c) The impact of two identical spheres on a water surface with impact velocity U = 5 m/s and size $\sim$ 10 mm. Only the coating of the spheres is different and changes the wettability. Clearly the contact line dynamics has a significant effect on the macroscopic phenomena. b) Snapshot of a hydrophilic sphere at t = 15.5 ms after impact. c) Snapshot of a hydrophobic sphere at t = 15.0 ms (adapted from Bocquet et al. [1].

which contact lines can move across a substrate are key in the macroscopic splash.

While for a long time research focused on static situations only [3–5], studies on contact lines became a more and more challenging topic of broad interest [6–9]. As shown in the example of impacting spheres, the dynamics of the contact line can have tremendous influences and evokes typical research questions as: what limits fast contact line motion? What sets the maximum speed for a drop sliding off a leaf? What happens when the contact line becomes unstable? These topics are not only of fundamental interest, but are also highly relevant for industrial applications such as printing, immersion lithography and coating. This thesis addresses fast contact line motion and related phenomena from both a fundamental and industrial perspective.

1.2 A closer look at the contact line

A more detailed view on the fluid mechanics near the contact line reveals the complexity of wetting dynamics. Figure 1.2 [9] shows a sketch of dip coating, which is a common simple configuration to study contact line dynamics. In dip coating, two cases can be considered: a plate withdrawn from (Fig. 1.2a) or plunged into (Fig. 1.2b) a liquid bath with velocity U. The streamlines are sketched for the fluid motion close to the moving substrate. In both cases, the no slip boundary condition at the moving substrate induces a flow inside the liquid. Since the fluids are immiscible, the flow is essentially confined to a wedge-shaped domain. Remarkably, such a geometry leads to a problem that was first acknowledged by Huh and Scriven in

1971 [10]. They realised that with the no-slip boundary condition, the viscous dissipation diverges at a moving contact line due to the singular gradients in the velocity field. This observation becomes apparent from the streamlines shown in figure1.2a. Following one of the streamlines, the line remains parallel to the plate at first, until a sharp turn has to be made close to the contact line to satisfy conservation of mass. Streamlines closer to the contact line make increasingly sharp turns, resulting in a diverging velocity gradient. Or in terms of the shear stress: $\tau \sim \mu U/h$ diverges for $h(x)$ going to zero. Hence, it would take an infinite force to move a contact line over a solid, such that "not even Herakles could sink a solid if the physical model were entirely valid, which is not" [10]. In other words, there should exist a regularisation at some small scale such that liquid is no longer prohibited to move across a substrate. Since, as observed in every day life, drops can in fact slide of a leaf. Typical regularizations used in models come from, for example, a finite slip-length, a precursor film, or evaporation [11],

Although the simplified view of a straight wedge does give insight into the singular behaviour of contact lines, it is not a complete hydrodynamic description of the problem. In fact, as is shown in Fig. 1.2c, the interface is deformable. A model that does take into account the deformation of the interface and regularisation at small scale is the well-known Cox-Voinov law [12–15]. From a hydrodynamic balance between viscous and capillary forces, this law describes the curved surface by the dynamic contact angle as a function of position from the contact line, $\theta_d(x)$:

$$\theta_d^3 = \theta_{eq}^3 \pm 9\mathrm{Ca}\ln\left(\frac{x}{\ell}\right). \tag{1.1}$$

The plus corresponds to advancing contact lines and the minus to receding contact lines. From scaling the dimensionless velocity,

$$\mathrm{Ca} = \frac{\eta U}{\gamma}, \tag{1.2}$$

appears naturally in the equation. In this definition, η, γ and U, are respectively, the viscosity, liquid/gas surface tension and velocity. From equation 1.1 one observes that the dynamic contact angle θ_d on large scale, depends on the wettability of the substrate, characterised by θ_{eq}, the dimensionless velocity Ca, and the distance from the contact line $\ln(x/\ell)$. The logarithm contains a microscopic length ℓ which is the cut-off of the singularity at molecular scale, where the discrete character of the molecules becomes noticeable (typically $\sim$ 1 - 10 nm). Although this equation was originally derived using the lubrication approximation, it turns out that this equation is a good approximation up to moderately large angles ($\approx 135^\circ$).

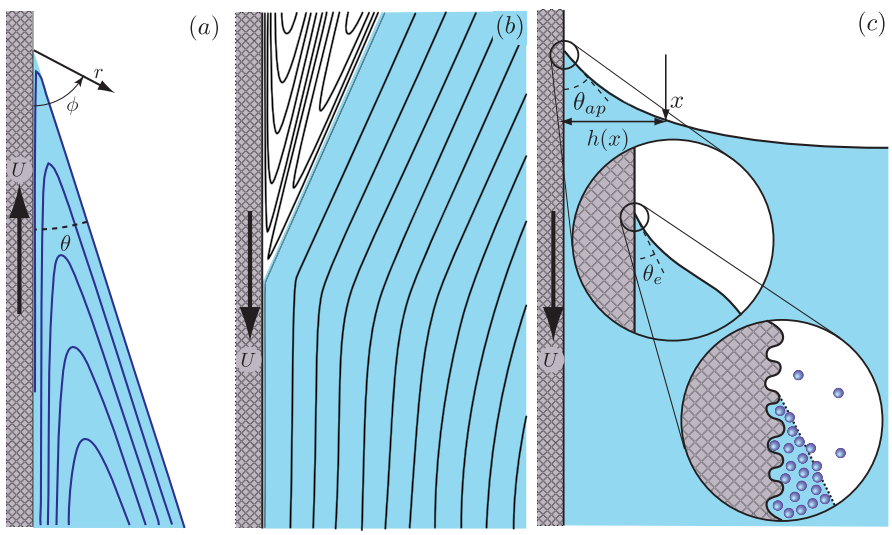

Figure 1.2: Schematic of the multi scale nature of the problem. Streamlines in a perfect wedge [10] of angle θ for (a) a receding contact line, and for (b) an advancing contact line. Strong confined circulation inside the wedge results in large viscous dissipation. (c) Interface profile $h(x)$ for a plunging plate under partial wetting conditions. The interface near the contact line is curved so that the apparent contact angle θ_{ap} on the macroscopic scale is much larger than the true contact angle θ_{eq} at nano meter scale. The intermediate zoom represents the hydrodynamic regime that is governed by viscosity and surface tension. From Snoeijer and Andreotti [9], and Bonn et al. [8].

Equation (1.1) describes contact line motion from a balance of forces. However it turns out that there exist a maximum velocity at which the balance can no longer be achieved: if the contact line is forced to move faster than this critical velocity it will undergo a (forced) wetting transition. Such a wetting transition results in for example bubble entrainment or droplet deposition. The Cox-Voinov law suggests that the maximum contact line velocity of for example receding contact lines, is reached when $\theta_d \to 0$. However, this does not take into account several important nuances. First, the macroscopic (outer) scale affects the critical dewetting dynamics [16, 17]. Namely, it determines the effective outer scale "x" that appears in equation 1.1. This was shown rigorously for the case of dip-coating [18]. Second, the Cox-Voinov relation is a two-dimensional approach and therefore does not take into account that most contact line problems develop three dimensional geometries. It was first reported by Blake and Ruschak that a saw-tooth shaped contact line precedes the entrainment of a film [19]. The inclination of the contact line with respect to the direction of motion effectively reduces the velocity of the contact line in the forced direction of motion. For the receding contact line this can be expressed as: $U_{normal} \sim 1/\sin\phi$ (see figure 1.3c). This three dimensional aspect is also observed and well studied for the case of sliding drops under the effect of gravity [20–23] . Although the effective contact line velocity is reduced, there still exists a critical speed where the contact line becomes unstable, leading to so called pearling, i.e. the deposition of small droplets from the sliding drop [20, 21, 24].

Finally we note that nearly all descriptions for contact line hydrodynamics assume Stokes flow. However, despite the small length scales, the Reynolds numbers in these problems can be larger than unity for fast contact line motion [1, 25, 26]. For example, the impacting sphere of Fig. 1.1 has $Re \sim 10^3 - 10^5$, so that inertia can clearly not be ignored. Even in very common problems, inertia could be relevant, e.g. for spreading of a low viscosity drop [27–29] or in capillary rise [26]. It is a challenging field with many open questions very relevant for contact line dynamics and wetting transitions.

1.3 Immersion Lithography

Contact line dynamics is not only of fundamental interest, but also plays an important role in many industrial applications, such as printing, immersion lithography, coating, cleaning and pattern formation. In case of immersion lithography, the critical velocity of moving contact lines is an important factor since it determines up to what speed contact lines remain stable as they move over a substrate. Hence contact line

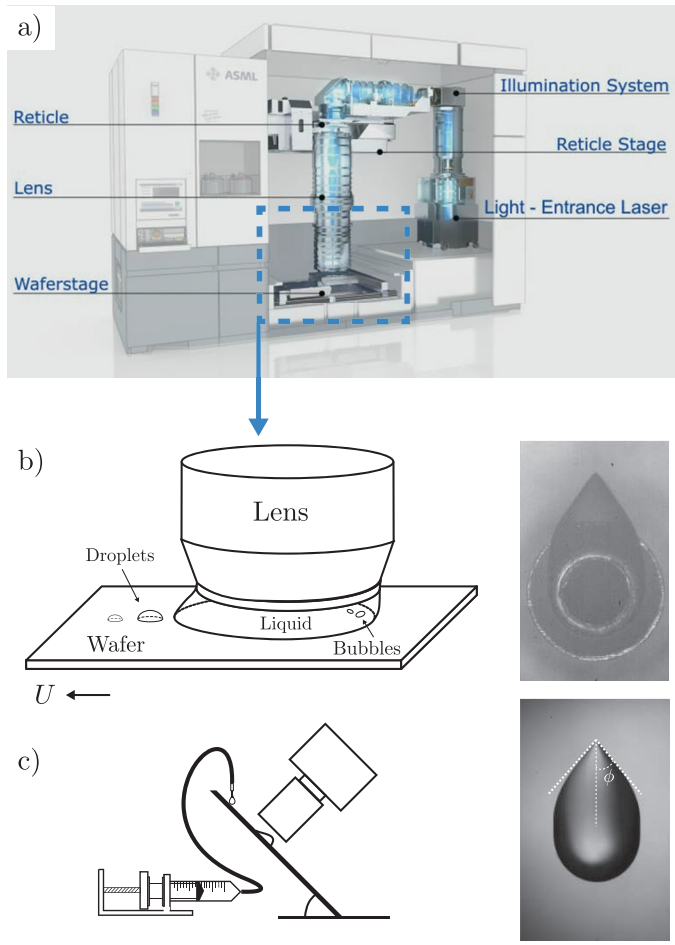

Figure 1.3: a) Image of an Immersion Lithography system [30]. b) Schematic of the immersion hood. The gap between the substrate (wafer) and a lens is filled with liquid. This schematic shows the result from instabilities which may occur at too high scan velocities, i.e. drop deposition on the wafer and bubble entrainment in the liquid lens. At high velocities the contact line motion highly resembles the tail of a (c) sliding drop on an inclined plate. The contact lines at the rear of the drop form a conical shape with opening angle ϕ.

motion has an influence on the throughput and manufacturing process. The research presented in this thesis is part of the FOM Industrial Partnership Program "Contact line control during wetting and dewetting" in collaboration with ASML and Océ. This thesis focuses on fundamental questions relevant for ASML, in the context of Immersion Lithography systems (Fig. 1.3a).

After the invention of the transistor half-way last century, electronics developed quickly. The chip performance doubled approximately every 18 months. A first prediction of such a trend is also known as Moore's law [31, 32]. As the design of electronics becomes more and more complex, the demand of smaller structures and faster machines in semi-conductor industry rises accordingly. Smaller structures require more advanced lithography techniques, such as photo-lithography. In this technique light is used to pattern a photo resist. The size of smallest possible structures depend on the resolution of the optical system which is given by the Rayleigh equation,

$$R = k\frac{\lambda}{NA}. \tag{1.3}$$

In this equation k is a system dependent pre-factor, λ is the optical wavelength of the used light and NA is the numerical aperture. The latter is a function of the index of refraction n of the surrounding media and the acceptance angle of the lens α: $NA = n\sin(\alpha)$. Hence an increase in the index of refraction leads to a considerable increase in the resolution, i.e. ability to print smaller structures. This leads to the currently used immersion lithography systems, in which the air ($n = 1$) in between the substrate (wafer) and the lens, is replaced by water ($n = 1.44$ for ArF DUV light with a wavelength of 193 nm). A simplified sketch of this situation is shown in Fig. 1.3a,b. Interestingly, the liquid needs to be confined between the lens and the wafer, thereby introducing a contact line in the system. To pattern a complete area of the substrate, the wafer is attached to wafer tables and moves at speeds up to ~ 1 m/s relative to the lens. Accordingly, this results in fast contact line motion with new challenges. At speeds below the critical velocity, the immersion liquid resembles a drop sliding down an incline. When the speed is increased the contact line can become unstable, leaving sessile droplets on the wafer at the receding side, and/or entraining bubbles at the advancing side. As a consequence undesired effects occur, for example, the drying of the sessile droplets result in stains on the wafer [33], and collisions of sessile droplets with the advancing part of the immersion liquid (returning motion) result in bubbles inside the immersion liquid. These bubbles and defects hinder or affect the lithography process significantly [34]. For commercial reasons, the throughput and yield should be as high as possible, but the necessary motion between the lens and the substrate is now partially limited by the critical velocity of the contact line. Therefore to avoid undesired effects, one faces a number

of fundamental questions such as: What determines the instability of contact lines? Can we predict the critical speed? How are bubbles entrapped? How are droplets deposited at the substrate?

1.4 Fast contact lines in drop spreading

High demands from the semi-conductor industry thus push the contact line motion to increasingly large velocities. However, fast contact line motion is not only found in industrial processes: very fast contact line dynamics can also be found in nature. For example immediately after first contact of drops with a surface. This simple phenomenon is an ideal system to fundamentally study fast contact line motion. Roughly speaking, the first contact of drops with a substrate can be categorised into situations where the impact velocity is high enough to play a role, and problems where the impact velocity is essentially zero. In both situations there exists a stage or circumstance in which the contact line could determine the dynamics [13, 27, 28, 35, 36]. Here we focus on the zero velocity contact or "drop spreading" which is generally known to be viscously dominated ('slow') in the final spreading stage. In this 'slow spreading regime' the drop approaches its final equilibrium shape and the dynamics is well described by Tanner's law [13]. This law can easily be derived from equation 1.1 with $\theta_e = 0$, and mass conservation of the drop:

$$\frac{r}{R} \sim \left(\frac{\gamma t}{\eta R}\right)^{1/10}. \tag{1.4}$$

Remarkably, it was found that the very first steps of spreading of water drops on a wetting surface are dominated by inertia. This was first recognized by Biance et al. [27] for completely wetting surfaces, and further investigated for partially wetting surfaces by Bird et al. [28, 29]. In these experiments, the radius r of the wetted area (with the contact line as perimeter) is determined from high speed recordings (see figure 1.4a). From a simple balance of inertial pressure and capillary pressure, the inertial time scale can be determined: $\tau_{inertial} \sim \sqrt{\rho R^3/\gamma}$, with ρ the density, R the drop radius and γ the surface tension. Rescaling experimental data with the inertial time scale for different drop sizes R and one specific wettability collapses the data for spreading water drops onto a single curve. This suggest that the short time dynamics of wetting are dominated by inertial forces instead of viscous forces. As observed in the experiments, high velocities are indeed reached: $r \sim 0.5$ mm in $t \sim 0.5$ ms. Besides this clear evidence of inertial drop spreading there are two other remarkable observations. First, the spreading dynamics clearly depends on the wetting properties of the substrate (i.e. equilibrium contact angle – see figure 1.4b). The observations

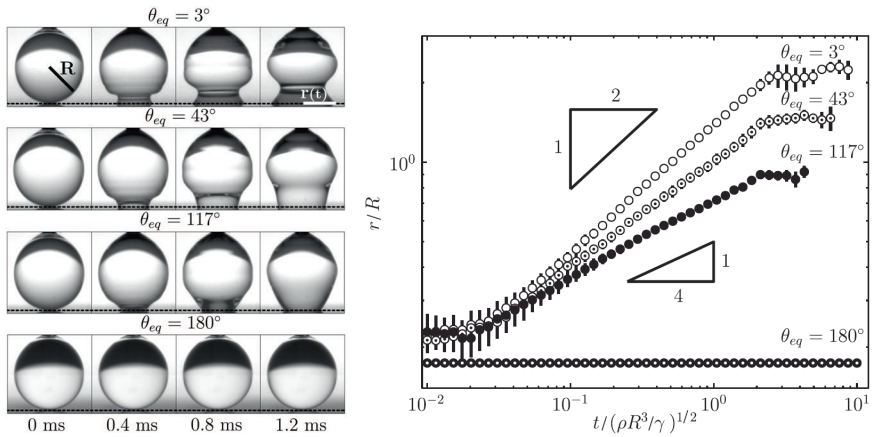

Figure 1.4: Experimental findings by Bird et al.[28]. a) The initial stages of spreading of water drops, just after it is brought into contact with a solid substrate. Different series correspond to different equilibrium contact angle θ_{eq} (drop radius $R = 0.82 \pm 0.01$ mm). Clearly, the wettability affects the spreading dynamics. b) Radius of wetted area r normalized with the equilibrium drop radius R as a function dimensionless time $t/\sqrt{\rho R^3/\gamma}$ for different substrate wettabilities.

by Bird et al., suggests a wettability dependent spreading, $r \sim t^{\alpha}$, with an exponent $\alpha(\theta)$ that depends on wettability. This is very surprising since force balances usually result in a power law with a constant exponent. The second noteworthy feature is that for all wettabilities the drop spreading seems to start at a fixed finite contact radius, rather than from a single point $r(t = 0) = 0$, as one might expect from geometry.

1.5 Singularities

Each of the contact line problems discussed above involve the appearance of singularities [37]. Mathematically, singularities are points at which a function takes an infinite value. For capillary flows this happens when there exist vanishing length or time scales which result in diverging pressures. In physical systems the molecular structure re-emerges at microscopic scales and the singularity is cut off. From an experimental point of view, the obvious challenge is to deal with the great disparity of time- and length-scales that describe the problem near singularity: one needs to push the spatial and temporal resolution to the limits of what is possible. A collection of the singularities observed in this thesis are shown in figure 1.5. Essentially the singularities can be divided into two categories: persistent singularities and dynami-

cal singularities [37]. The first type exists for a period or indefinitely in time and can move around in space. The moving contact line itself is an example of such a singular problem at any velocity (see figure 1.5a). Another persistent singularity is the corner shape observed at the rear end of the drop. When the critical velocity is approached, the inclined receding contact lines meet in a very sharp tip (see Fig. 1.3b). However it was shown by Peters et al. [38], that this corner singularity is actually regularised and has a small but finite curvature (see figure 1.5b).

The second kind of singularities, dynamical singularities, change in time and normally result into or result from topological changes. In the case of moving contact lines, such a dynamical singularity occurs when the critical contact line velocity is exceeded. This results in the formation of a rivulet from the tail that becomes unstable and subsequently breaks up into droplets. The pinch-off of small droplets from the tail involves a singularity (tail width w goes to zero; see figure 1.5c), and indeed involves a topological change: a single drop breaks up into two droplets. In the case of Immersion Lithography, sessile droplets on the substrate can collide with the advancing part of the immersion bath (meniscus-droplet impact). When the meniscus and the droplet come into contact, coalescence takes place, starting at a singular point of contact. It will turn out that this topological change can induce the entrapment of small air bubbles as is indicated in figure 1.5d. Finally, in case of drop spreading, the moment of contact is singular in a way comparable to coalescence, as shown in figure 1.5e.

1.6 Guide through the thesis

Figure 1.5, gives a clear overview of the investigated subjects in this thesis, each of which is related to fast contact line motion in Immersion Lithography. In Chapter 2 we first provide a detailed comparison between sliding drops and the moving contact line in a system that resembles an Immersion Lithography system (see Fig. 1.5a,b). Since motions in Immersion Lithography are not always steady, we then study the quasi-steady assumption for non-steady motion of contact lines in Chapter 3. Instead of the usual constant contact line velocity, the contact line is forced to move under an acceleration. Typical questions that will be addressed are: What sets the critical velocity of moving contact lines? To what extent are sliding drops comparable to an Immersion Lithography system? It is well known that there exists a critical velocity at which the receding contact line becomes unstable. What happens once a receding contact line becomes unstable? We experimentally study the stability of the reced-

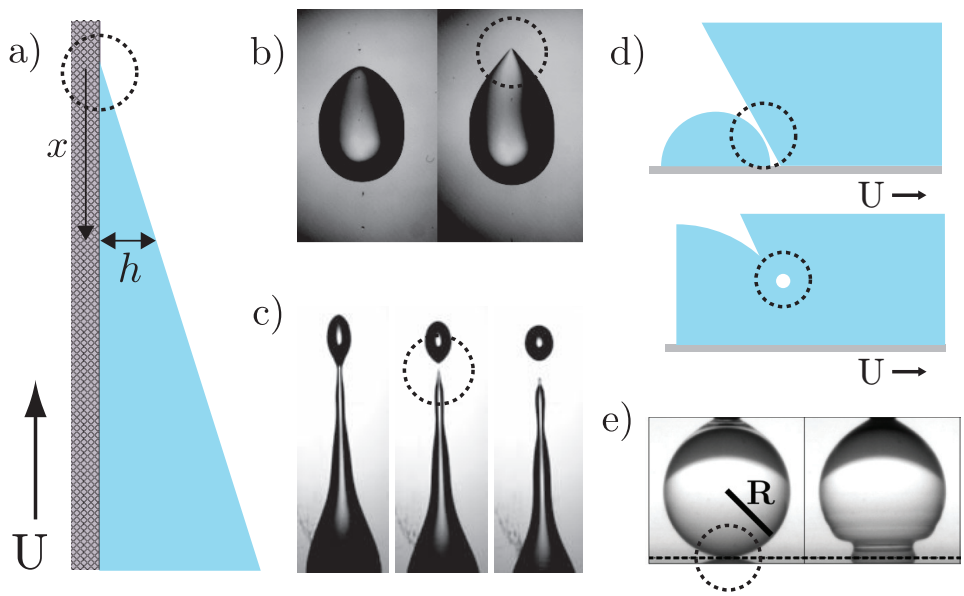

Figure 1.5: Overview of the types of singularities observed in this thesis, each of which is characterised by small length scales. The singularities are indicated by the dashed circles. a) Schematic of a receding contact line with interface profile $h(x)$ ($h(x) \to 0$ approaching the contact line). b) With increasing velocity the rear of a sliding drop forms a cornered tail with a small but finite tip curvature. c) Exceeding the critical velocity the tail of a sliding drops breaks into smaller droplets after pinch-off [21]. d) In the collision of sessile drops with an advancing meniscus, bubbles are observed after the coalescence process. e) From geometry one would expect drop spreading to start from a singular point [28].

ing contact line and investigate the break-up that occurs close to the critical speed in Chapter 4. Interestingly, the sessile drops that are left on the substrate can later collide with an advancing meniscus (see Fig. 1.5c,d). In applications such as dip-coating and immersion lithography, these droplets collide with an advancing meniscus, resulting in the entrapment of bubbles (see Fig. 1.5d). Since the bubble size and understanding of the underlying bubble formation mechanism is highly relevant for Immersion Lithography, we experimentally study droplet-meniscus collisions in Chapter 5. Is it possible to predict bubble entrainment from knowledge about contact line dynamics? What are the bubble-type and -size?

We also study drop spreading on partial wetting substrates, to understand more about the fundamentals of fast contact line motion. The spreading is a relative simple system that gives insight in contact line dynamics in fast spreading motion (see Fig. 1.5e). What are the dynamics shortly after the first contact? First we study the spreading of water drops on partially wetting surfaces in Chapter 6. In Chapter 7, we extend this study to more viscous drops and investigate to what extent the fast motion is dominated by inertia.

The final chapter, Chapter 8, concerns a subject without any contact line involved. We experimentally study levitated drops on an air cushion. This situation is very similar to the 'Leidenfrost' state in which drops levitate on a vapour film that emerges above a threshold temperature. It is well known that these drops can start oscillating, in so-called "star-oscillations". In our experiments, we study this threshold phenomenon and eliminate the effects due to heat and temperature to get a better understanding of the actual oscillation dynamics.

References

[1] C. Duez, C. Ybert, C. Clanet, and L. Bocquet, "Making a splash with water repellency", Nat. Phys. **3**, 180 (2007).

[2] J. Eggers, "Coupling the large and the small", Nat. Phys. **3**, 145 (2007).

[3] T. Young, Philos. Trans. R. Soc. London **95**, 65 (1804).

[4] P. S. d. Laplace, Méchanique Céleste, Supplément au Xiéme Libre (1805).

[5] Y. Pomeau and E. Villermaux, "Two hundred years of capillarity research", Physics Today **59**, 39–44 (2006).

[6] L. Léger and J.-F. Joanny, "Liquid spreading", Rep. Prog. Phys. **55**, 431–486 (1992).

[7] P. G. de Gennes, "Wetting: statics and dynamics", Rev. Mod. Phys. **57**, 827–863 (1985).

[8] D. Bonn, J. Eggers, J. Indekeu, J. Meunier, and E. Rolley, "Wetting and spreading", Rev. Mod. Phys. **81**, 739–805 (2009).

[9] B. Andreotti and J. H. Snoeijer, "Moving contact lines: Scales, regimes, and dynamical transitions", Annual Review of Fluid Mechanics **45**, null (2013).

[10] C. Huh and L. E. Scriven, "Hydrodynamic model of steady movement of a solid/liquid/fluid contact line", J. Coll. Int. Sci. **35**, 85–101 (1971).

[11] G. Berteloot, C. T. Pham, A. Daerr, F. Lequeux, and L. Limat, "Evaporation-induced flow near a contact line: Consequences on coating and contact angle", Europhys. Lett. **83** (2008).

[12] O. V. Voinov, "Hydrodynamics of wetting [english translation]", Fluid Dynamics **11**, 714–721 (1976).

[13] L. H. Tanner, "The spreading of silicone oil drops on horizontal surfaces", J. Phys. D: Appl. Phys. **12**, 1473–1478 (1979).

[14] R. G. Cox, "The dynamics of the spreading of liquids on a solid surface. part 1. viscous flow", J. Fluid Mech. **168**, 169–194 (1986).

[15] B. R. Duffy and S. K. Wilson, "A third-order differential equation arising in thin-film flows and relevant to tanner's law", Appl. Math. Lett. **10**, 63 (1997).

[16] G. Delon, M. Fermigier, J. H. Snoeijer, and B. Andreotti, "Relaxation of a dewetting contact line part 2: Experiments", J. Fluid Mech. **604**, 55 (2008).

[17] J. Ziegler, J. H. Snoeijer, and J. Eggers, "Film transitions of receding contact lines", Eur. Phys. J. Special Topics **166**, 177 (2009).

[18] J. Eggers, "Hydrodynamic theory of forced dewetting", Phys. Rev. Lett. **93**, 094502 (2004).

[19] T. D. Blake and K. J. Ruschak, "A maximum speed of wetting.", Nature **282**, 489–491 (1979).

[20] T. Podgorski, J. M. Flesselles, and L. Limat, "Corners, cusps, and pearls in running drops", Phys. Rev. Lett. **87**, 036102(1)–(4) (2001).

[21] N. Le Grand, A. Daerr, and L. Limat, "Shape and motion of drops sliding down an inclined plane", J. Fluid Mech. **541**, 293–315 (2005).

[22] L. Limat and H. A. Stone, "Three-dimensional lubrication model of a contact line corner singularity", Europhys. Lett. **65**, 365 (2004).

[23] M. Ben Amar, L. J. Cummings, and Y. Pomeau, "Transition of a moving contact line from smooth to angular", Phys. Fluids **15**, 2949–2960 (2003).

[24] J. Snoeijer, N. Le Grand, L. Limat, H. A. Stone, and J. Eggers, "Cornered drop and rivulets", Phys. Fluids **19**, 042104 (2007).

[25] K. Stoev, E. Ramé, and S. Garoff, "Effects of inertia on the hydrodynamics near moving contact lines", Phys. Fluids **11**, 3209 (1999).

[26] D. Quéré, "Inertial capillarity", EPL (Europhysics Letters) **39**, 533 (1997).

[27] A.-L. Biance, C. Clanet, and D. Quéré, "First steps of the spreading of a liquid droplet", Phys. Rev. E **69**, 016301 (2004).

[28] J. C. Bird, S. Mandre, and H. A. Stone, "Short-time dynamics of partial wetting", Phys. Rev. Lett. **100** (2008).

[29] L. Courbin, J. C. Bird, M. Reyssat, and H. A. Stone, "Dynamics of wetting: from inertial spreading to viscous imbibition", J. Phys.: Condens. Matter **21**, 464127 (2009).

[30] From ASML media library.

[31] R. Schaller, "Moore's law: past, present and future", Spectrum, IEEE **34**, 52 –59 (1997).

[32] G. Moore, "Cramming more components onto integrated circuits", Electronics **38**, 114–117 (1965).

[33] A. G. Marín, H. Gelderblom, D. Lohse, and J. H. Snoeijer, "Order-to-disorder transition in ring-shaped colloidal stains", Phys. Rev. Lett. **107**, 085502 (2011).

[34] M. Switkes, R. M., T. A. Shedd, H. B. Burnett, and M. S. Yeung, "Bubbles in immersion lithography", J. Vac. Sci. Technol. B **23**, 2409 – 2412 (2005).

[35] R. Rioboo, M. Marengo, and C. Tropea, "Time evolution of liquid drop impact onto solid, dry surfaces", Experiments in Fluids **33**, 112–124 (2002).

[36] A. Yarin, "Drop impact dynamics: Splashing, spreading, receding, bouncing.", Annual Review of Fluid Mechanics **38**, 159–192 (2006).

[37] J. Eggers, "Hydrodynamic singularities", in *A Perspective Look at Nonlinear Media in Physics, Chemistry, and Biology*, edited by J. Parisi, S. C. Mueller, and W. Zimmermann, 305–312 (Springer, Berlin) (1998).

[38] I. R. Peters, J. H. Snoeijer, A. Daerr, and L. Limat, "Coexistence of Two Singularities in Dewetting Flows: Regularizing the Corner Tip", Phys. Rev. Lett. **103** (2009).

2

Cornered contact lines: from sliding drops to immersion lithography *

Instabilities of receding contact lines often occur through the formation of a corner with a very sharp tip. These dewetting structures also appear in the technology of Immersion Lithography, where water is put between the lens and the silicon wafer to increase the optical resolution. In this paper we aim to compare corners appearing in Immersion Lithography to those at the tail of gravity driven-drops sliding down an incline. We use high speed recordings to measure the dynamic contact angle and the sharpness of the corner, for varying contact line velocity. It is found that these quantities behave very similarly for Immersion Lithography and drops on an incline. In addition, the results agree well with predictions by a lubrication model for cornered contact lines, hinting at a generic structure of dewetting corners.

2.1 Introduction

A fluid displacing another immiscible fluid across a solid surface is a very common phenomenon in both nature (e.g. such water drops sliding down a leaf [1]) and in-

*Published as: K.G. Winkels, I. R. Peters, F. Evangelista, M. Riepen, A. Daerr, L. Limat, and J.H. Snoeijer, Receding contact lines: from sliding drops to immersion lithography, Eur. Phys. J. Special Topics 192, 195205 (2011)

dustrial processes (e.g. printing and coating [2]). The fluid motion is controlled by the dynamics of the contact line, which is susceptible to instabilities when moving at large speeds [1, 3]. The standard approach to this problem is to assume the contact line remains straight during the motion, so that the flow is essentially two-dimensional. At low speeds this gives rise to the Cox-Voinov law [4, 5], describing the dynamic contact angle as a function of speed. The relevant dimensionless parameter is the capillary number, $\mathrm{Ca} = U\eta/\gamma$, representing the contact line velocity U rescaled by the typical dewetting velocity built upon viscosity η and surface tension γ respectively. The simplest scenario for instability of straight contact lines is that the contact angle becomes zero at a critical speed [6, 7]. At higher values of Ca the contact line gives way to the deposition of a liquid film [6, 8–11].

Interestingly, instability of receding contact lines often occurs through the formation of a corner with a very sharp tip, for which the flow is manifestly three-dimensional. This goes back to the work of Blake and Ruschak [12], who found that in the withdrawal of a plate from a liquid bath, the contact line adopts a 'v' shape at large speeds. The appearance of the corner was interpreted as a mechanism to reduce the effective contact line speed, since the inclination of the contact lines reduces their normal (perpendicular) velocity. Very similar corner shapes were observed for drops sliding down an incline, as shown in figure 2.1b [13, 14]. Drops are viewed from the top while sliding down under the influence of gravity. Instead of remaining circular, the receding 'tail' of the drop develops a corner-like structure that turns sharper with increasing capillary number. At even higher speeds the tail breaks up and small droplets are deposited on the surface. Under the assumption of a conical structure of the liquid, this tail can be described by a lubrication model [15]. This captures the essential geometrical features as well as the flow in the vicinity of the contact line [16, 17].

These three-dimensional dewetting phenomena turn out to play a crucial role in the technology of Immersion Lithography (figure 2.1c and 2.1d). This is a technique that is widely applied in semiconductor industry to achieve higher optical resolutions, and accordingly smaller dimensions [18, 19]. The conventional Lithography method, which consists of the projection of light patterns through a lens on substrates, is improved by replacing the air between the lens and the substrate by a liquid with a higher refractive index (figure 2.1c). This increases the numerical aperture of the system and consequently the imaging resolution. For ultra pure water, the commonly used liquid, the smallest printable features become of order $\sim$40 nm. While the liquid is advantageous for the optical performances, it introduces new complexities associated to the contact line. Since the lens cannot cover the complete substrate at once, it is moved over the wafer with speeds close to instability: the critical velocity

at which water loss occurs near the contact line determines the maximum speed of the lens. As such, it creates engineering difficulties and limitations for the production yield of Immersion Lithography.

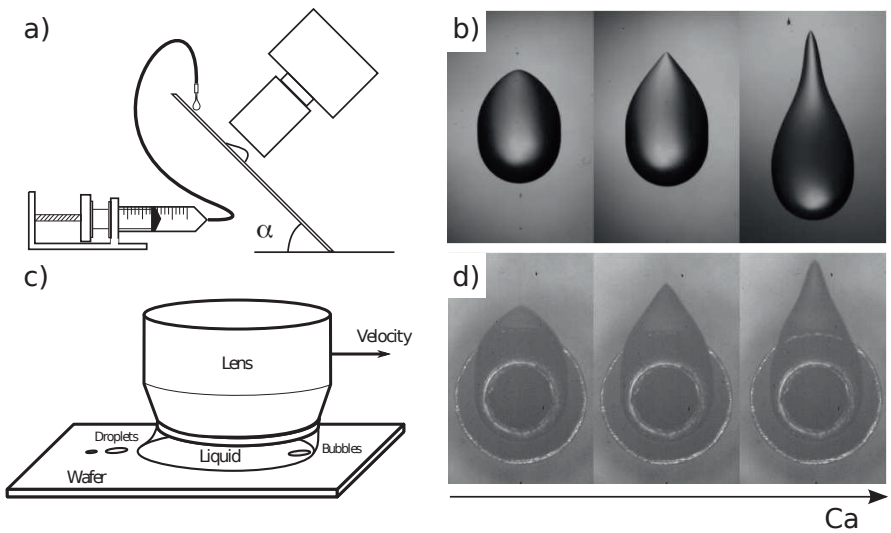

Figure 2.1: Analogy between drops sliding down an inclined plate and moving contact lines in Immersion Lithography. a) Setup used to study droplets sliding down an inclined plane; b) images from the experimental setup as shown in (a); c) Sketch of an Immersion Lithography system; d) images from a setup mimicking an Immersion Lithography system.

In this chapter we experimentally investigate the v-shaped contact lines observed in Immersion Lithography. We follow the evolution of the liquid corner as a function of speed by monitoring the angles from side-view and bottom-view imaging. It is clear from figure 2.1 that there is a striking resemblance with drops sliding down a plane and we make a quantitative comparison between the two systems. There are, however, some important differences between the two systems. First, the drops on an incline are driven by gravity and the speed is adjusted by the angle of inclination α, while in the Immersion Lithography experiment the substrate speed is imposed and controlled by a motor. Second, the Reynolds number for the silicon oil drops is negligible, while inertial effects could be expected for the low viscosity water drops in Immersion Lithography. These differences do not affect the generic features of the cornered contact lines in the set of experimental parameters/setting used, although

some quantitative differences are indeed observed.

The chapter is organized as follows. Section 2.2 defines the key quantities of the corner geometry and briefly reviews the main theoretical results. A detailed description of this experimental setup is given in Sec. 2.3. The central results are presented in Sec. 2.4, where we also make the detailed comparison with sliding drop data from [20], and the chapter closes with a Discussion.

2.2 Three-dimensional dewetting

The standard description of wetting dynamics assumes a straight contact line, resulting in a flow that is effectively two-dimensional. If one further assumes that inertia is not important, the dynamic contact angle seen from a side view, θ, follows from a balance of viscous forces and surface tension and thus depends on the capillary number Ca. Away from the critical speed, this is accurately described by the general Cox-Voinov relation [4, 5]

$$\theta^3 = \theta_0^3 \pm 9\mathrm{Ca}\ln\left(\frac{x}{\ell}\right), \tag{2.1}$$

where θ_0 is the static contact angle, while ℓ is a microscopic length at which the viscous singularity is regularized [21]. The sign is positive for advancing contact lines and negative for receding contact lines, the latter being relevant for this chapter. Note that the value of θ depends logarithmically on x, the distance to the contact line. Experimentally, the observed slope thus depends on the length scale at which the measurement is performed [22–24].

In the situation of straight contact lines the sole interface curvature lies in the plane parallel to the direction of motion of the contact line. This approach is too simple, however, as for the drops shown in figure 2.1 the interface becomes truly three-dimensional at higher Ca. The three-dimensional geometry can be solved by assuming that the interface develops a sharp conical shape [15–17]. The cone is characterised by two angles (figure 2.2): side view angle θ and top view (opening) angle ϕ. The lubrication equations indeed admit similarity solutions that are consistent with such a conical structure. This lubrication approach gives explicit predictions for the cone angles and these will be measured for the drops such as shown in figure 2.1.

A first prediction is that the cone angles θ and ϕ are related according to [15, 16]

$$\tan^3\theta = \frac{35}{16}\mathrm{Ca}\tan^2\phi. \tag{2.2}$$

This expresses the balance between viscous dissipation and capillary forces. In contrast to (2.1) the side-view angle no longer depends on the distance to the contact line,

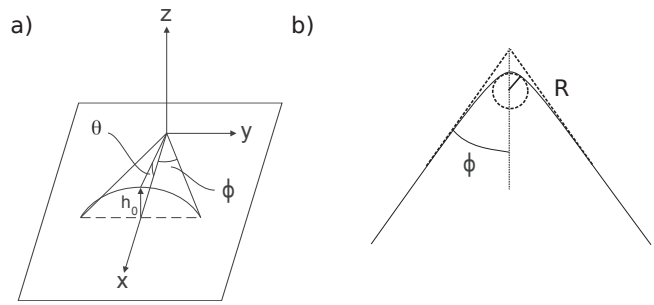

Figure 2.2: Schematic view of a cornered receding contact line. a) three-dimensional cone structure with characteristic angles ϕ and θ, b) the tip of the corner has a finite radius of curvature R.

but θ is simply constant along the cone. The reason is that for the cone the capillary forces result from the interface curvature defined in a plane *perpendicular* to the direction of motion (for straight contact lines this perpendicular curvature is zero). One should note, however, that this is not yet a closed expression for θ as a function of speed, since the opening angle ϕ also depends on Ca. The problem can be closed by introducing a matching condition near the inclined contact lines, and yields [17]

$$\frac{Ca}{\theta_0^3} = \frac{2\sin\phi}{18\sin^2\phi\ln\left(\frac{L}{\ell}\right)+\frac{35}{\cos^2\phi}} \approx \frac{2\phi}{18\phi^2\ln\left(\frac{L}{\ell}\right)+35}. \tag{2.3}$$

The latter step represents the limit of small ϕ. This relation predicts a maximum speed for the cone, occurring at a minimum value of the opening angle ϕ. Higher speeds result into instabilities and break-up.

While the cone model assumes a tip that is infinitely sharp, the tip of the receding contact line is in reality rounded at a small scale (figure 2.1). We therefore define the radius of curvature of the tip R as shown in figure 2.2b. At a large distance from the tip, $x \gg R$, one recovers the conical geometry characterized by a constant angle θ. On the other hand, the contact line will appear nearly straight when approaching the tip at a small distance $x \ll R$. We thus expect to recover the Cox-Voinov relation (2.1) in this regime. As was shown in [20], these two regions should match on a length scale of order R. Since in the corner regime $\theta^3 \ll \theta_0^3$, this matching yields

$$0 \approx \theta_0^3 - 9\mathrm{Ca}\ln\left(\frac{R}{\ell}\right), \tag{2.4}$$

where we took $x \approx R$ and $\theta \approx 0$ in (2.1). By inverting (2.4), we find a prediction for

the tip curvature R in terms of the speed:

$$R \approx \ell \exp\left(\frac{\theta_0^3}{9\mathrm{Ca}}\right). \tag{2.5}$$

In the remainder of the chapter we will experimentally measure the angles θ and ϕ as well as the tip curvature R, for varying contact line velocities. The relations mentioned above will provide the framework to quantitatively compare the data taken from an Immersion Lithography-like setup and from the drops sliding down an incline.

2.3 Experimental setup

The data compared in this chapter comes from two types of experiments: drops sliding down an inclined plate and moving contact lines in a configuration mimicking an Immersion Lithography system (figure 2.1). The data for the sliding drops on the inclined plane are taken from Peters et al. [20] (experiments similar to LeGrand et al. [14]), in which drops of silicon oil were used with a viscosity of $\mu = 18.6$ cP. The substrate was made partially wetting by a fluoro-polymers coating (FC725 by 3M). The various publications report minor differences in wetting properties, but typical values for the static contact angles are $\theta_0 \sim 45^\circ$, with a hysteresis of $\sim 10^\circ$. Drops were created in a controlled manner by using a syringe pump, resulting in droplet volumes in the range of 6-10 mm^3. The sliding speed of the drop was varied by the inclination angle of the plate.

The setup to mimic the Immersion Lithography situation is shown in figure 2.3 and will be referred to as the 'turntable setup/experiment', in the remainder of this chapter. While the sliding drops move through the reference frame of the camera, the liquid in the turntable setup is fixed in the reference frame of the cameras. The basic idea is to rotate a glass wafer on a turntable, while keeping a drop at a fixed position. To achieve this a droplet is held by the needle system shown in figure 2.3a. It consists of two concentric needles of different diameter (outer diameters of 1.84 mm and 1.27 mm, for the outer and inner needle respectively). Standard pure water is supplied through the inner needle at a constant flow rate of 12 ml/min. The outer needle simultaneously extracts water (liquid phase) and air at a fixed rate of 2.4 l/min, so that the water is constantly refreshed (an essential feature in Immersion Lithography systems to keep the water clean and at constant temperature as good as possible). The wall thickness of the outer needle is kept very thin and the height of the needle above the substrate as high as possible ($250\mu m$). While holding the droplet, a coated glass wafer of 300 mm diameter and 0.7 mm thickness is moved underneath. This

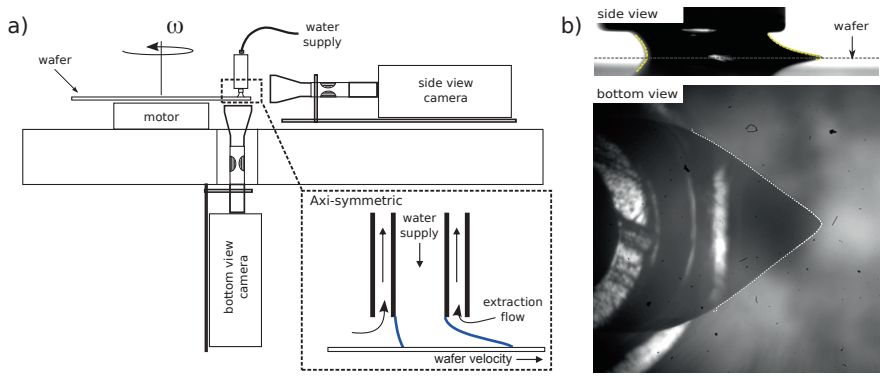

Figure 2.3: a) Sketch of the turntable setup b) Top and bottom view images from a typical measurement (U = 604 mm/s). The dashed line represents the detected boundary of the droplet obtained from digital imaging analysis.

is done by rotating the wafer by a custom made motor (IBS Precision Engineering) that is able to rotate the wafer at a maximum linear velocity of $u_{max} = 3$ m/s and maximum linear acceleration of $a_{max} = 100$ m/s^2 (measured at a radial distance of 140 mm from the center of the wafer). To obtain a partial wetting substrate, the glass wafers are coated having a static receding and advancing contact angle of 65° and 87°, respectively. All turntable experiments were carried out under controlled temperature, T = 22 $\pm$ 1 °C, and relative humidity, rH = 45 $\pm$ 5 %.

We simultaneously image the drop from the side and from below (figure 2.3). For side view imaging a high speed camera (Photron SA 1.1) is used in combination with a long distance microscope (Navitar 12X Telecentric Zoom System), whereas for the bottom view a more detailed view is realised (Photron SA 1.1 in combination with a Navitar 12X long distance microscope attached to a Mitutoyo Infinity Corrected objective). Resolutions of 6 μm/pixel (side) and 2.5 μm/pixel (bottom) are achieved. Typical recordings obtained from this setup are shown in figure 2.3b. Digital imaging analysis is used to detect the droplet boundary position. In both, bottom and side view recordings, this position is found by using a Canny filter [25]. This filter is applied in the region near the droplet contact line after image background subtraction and the contact line position is thus based on the gradient in pixel-intensity values (8-bit image). To avoid false detections, the edge detection is checked and verified by superposition on the original image (similar to the dashed lines shown in figure 2.3b). This boundary detection method is limited to pixel resolution and therefore results in discrete steps in the detected droplet edge. In order to find the tip position (wafer

position) on sub-pixel level, a parabolic function is fit to the first 10 pixels closest to the uttermost pixels of the raw edge detection. The minimum of the parabolic function is taken as the tip position. The final steps of data analysis will be specified while discussing the results in the following section.

Experimental data is obtained from multiple runs on different wafers in order to check the reproducibility. During each run we increase the velocity to 1 m/s, with an acceleration of 1 m/s^2, while the droplet is recorded simultaneously from the side and bottom, at a frame rate of 1000 fps. This corresponds to a linear velocity increase of 1 mm/s per frame. Hence, from a single recording it is possible to characterize the moving contact line behaviour as a function of the wafer speed. We have verified that the results are reproducible over a range of accelerations, so we can use the instantaneous speed (capillary number) as the relevant parameter. It should be noted that the Reynolds number based on the flying height is of the order $\mathcal{O}(100)$.

2.4 Results

2.4.1 Dynamic contact angle

The most basic characterisation of a moving contact line is the dynamic contact angle θ. In the literature we find a number of different definitions and is still subject to discussion [1, 22, 26]. Here we define θ as the angle based on the local interface slope defined by a linear fit, at a fixed distance from the contact line. The measurement uses the first detected boundary pixels within a fixed distance of 50 μm from the tip measured along the interface. In the spirit of the Cox-Voinov relation (2.1), this means that we measure the dynamic contact angle at a fixed position of $x = 25$ μm.

The results, up to break up, are presented in figure 2.4a. The circles represent data from turntable experiments, while the squares correspond to sliding drops. In both cases the dynamic contact angle decreases with Ca as expected for receding contact lines. For small speeds we find excellent agreements with the Cox-Voinov law, which is shown as dashed lines. The quality of the fits is further illustrated by plotting the same data as θ^3 versus Ca (figure 2.4b). This gives a straight line over a considerable range of velocities. According to (2.1), the slope of this line can be interpreted in terms of $\ln x/\ell$, where x is the scale of the measurement (≈ 25 μm) and ℓ a characteristic microscopic length. For the silicon oil drops this gives $\ln x/\ell = 8.9$, which indeed corresponds to a microscopic length, $\ell \approx 7 \cdot 10^{-9}$ m. The turntable data give a value $\ln x/\ell = 24$ ($\ell \approx 9.4 \cdot 10^{-16}$ m) which is surprisingly high (small). However, this value is consistent with experiments on water drops sliding down an incline [13], suggesting that this anomalous large value is, for presently unknown

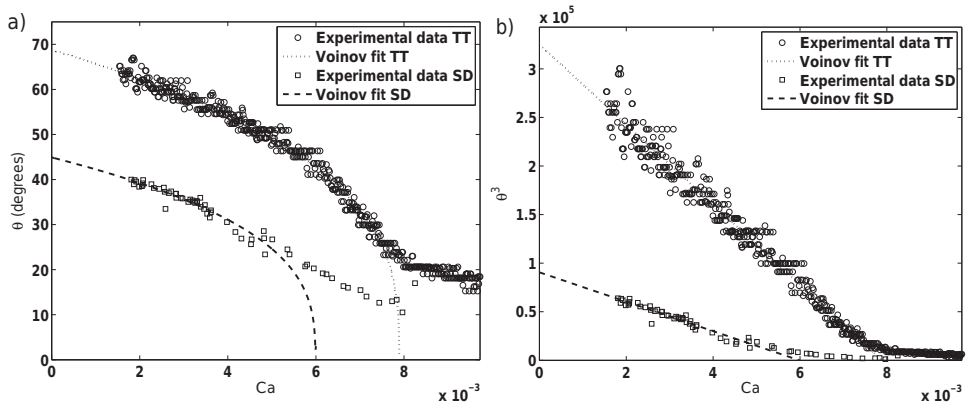

Figure 2.4: Dynamic contact angle θ as a function of the capillary number (normalized contact line velocity). The circles and squares represent the data obtained from the turntable setup (TT) and sliding droplet experiment (SD), respectively. The dashed lines represent the fit based on Cox-Voinov relation (2.1).

reasons, specific for water.

Interestingly, a significant deviation from Cox-Voinov is observed at higher speeds for both data sets. For turntable experiments this occurs around Ca $\sim 8 \cdot 10^{-3}$, while for sliding drops Ca $\sim 6 \cdot 10^{-3}$. Below we show in detail that for both experiments this coincides with the moment that the scale of measurement x becomes, $x \sim R$. We shall thus interpret this behaviour for θ as a change in geometry of the interface: from a two-dimensional straight contact line, as assumed for (2.1), to a three-dimensional conical shape. Note that the extrapolation of Voinov (two-dimensional approach) predicts vanishing contact angles. By changing the shape it thus seems that it can postpone the instabilities. However break up cannot be avoided, and occurs in the region of the maximum Ca plotted in the graph (for turntable data, $Ca \sim 0.01$ and sliding droplets $Ca \sim 0.008$).

2.4.2 Tip curvature

Let us now investigate the formation of the corner in more detail. The images on figure 2.5a show the change from a rounded contact line at low speeds to a sharp corner at higher speeds. To quantify this transition one can measure the curvature (sharpness) of the tip as a function of speed. We do so by fitting a circle to a number of detected boundary points near the tip. The fit is made in a least square sense, however the best fit will also depend on how many points are taken into account.

To solve this, the best fit is always based on all points within a vertical distance of 5 pixels from the tip. A number which is based on the assumption that one cannot measure radii smaller than 5 pixels ($\sim 14\ \mu m$),

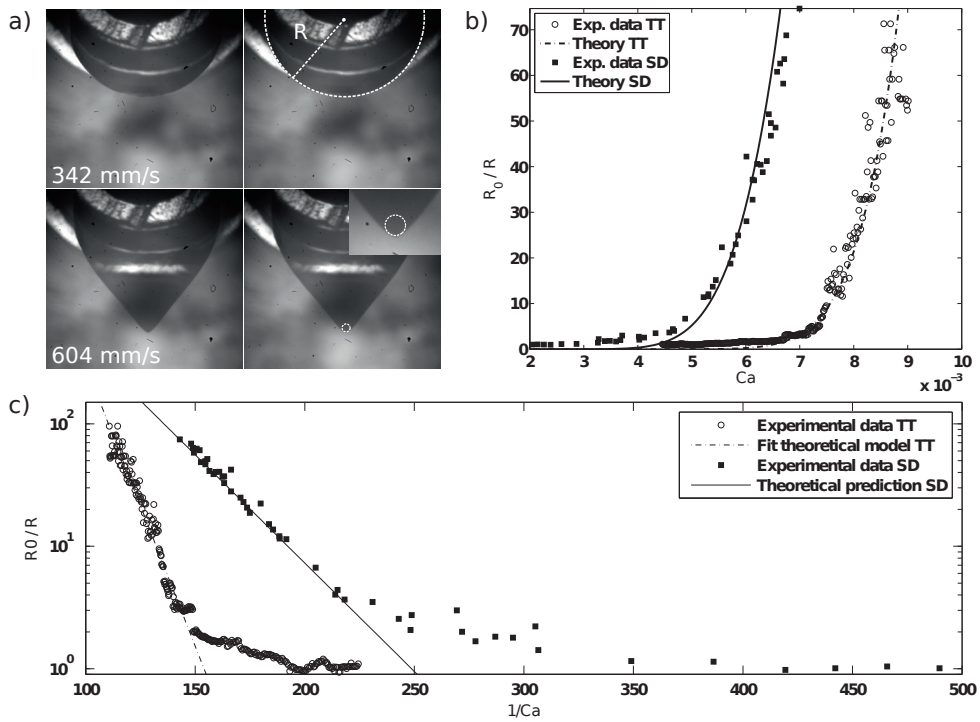

Figure 2.5: Measurement of the tip curvature. a) images of typical circle fits to the receding contact line, including the definition of the radius of curvature R. b) tip curvature R_0/R versus Ca. Data are normalized by the initial radius of curvature R_0. Circles and squares denote data from turntable experiments (TT) and drops sliding down an incline (SD), respectively. c) Same as in b) plotted on a logarithmic scale to reveal the exponential behaviour (2.6). Solid and dashed lines are the fits with $\ell \sim 0.1$ nm with $A = 0.11$ and $\ell \sim 9$ nm with $A = 0.05$ for the turntable data and sliding droplets, respectively.

The results are shown in figure 2.5b, where we plot the curvature R_0/R as a function of contact line speed Ca. Data are normalized by the initial radius, $R_0 = 0.75$ mm for turntable experiments, and $R_0 = 1.63$ mm for sliding drops. We find that the curvature remains nearly constant at low speeds, but observe a dramatic increase when the corner is formed. The curvature increases by almost 2 decades over a small

range in Ca. The smallest measured tip size before instabilities, is of the order of 10 μm and 20 μm, for turntable data and sliding droplets, respectively.

To test the theoretical prediction (2.5), we fitted the data with

$$R = \ell \exp\left(\frac{A}{\mathrm{Ca}}\right). \tag{2.6}$$

These are plotted as solid and dashed lines in figure 2.5b and 2.5c, and provide a good description of the experimental data. The exponential behaviour is best revealed on a semi-logarithmic plot (figure 2.5c), where the slope of the linear fit represents the exponential prefactor A and the offset the characteristic microscopic length scale. The former is found to be of the order nanometers/Ångström (as expected for the microscopic length scale) for both experimental data sets. The fitted values for turntable data are $\ell \sim 0.1$ nm and $A \approx 0.11$, while for sliding droplets, $\ell \sim 10$ nm and $A \approx 0.05$. Note that these values are very sensitive to the details of the fit. According to the model (2.5), one should find $A \approx \theta_0^3/9$. The data are indeed consistent with the static contact angle $\theta_0 = 45^\circ$ for the viscous sliding drops. In case of the turntable data, however, the values of A corresponds to $\theta_0 = 56^\circ$, which is not in accordance with the static receding contact angle ($\theta_0 = 65^\circ$). We come back to this issue, i.e. the difference between water and silicon oil, in the Discussion.

2.4.3 Corner opening angle

The final characteristic of the corner is the top view angle ϕ. Experimentally, however, there is a limited range of Ca where ϕ is a well defined quantity. This is clearly visible from the images in figure 2.1d). The shape of the contact line is rounded at low capillary numbers (left image). At intermediate velocities (center image), the contact line becomes distinctly "v"-shaped, resulting in two straight contact lines with a well defined angle ϕ. At higher velocities (right image) both straight contact lines become inflected, meaning that the opening angle ϕ will depend on the position of measurement. Finally, the tail gives way to a rivulet like structure ultimately becoming unstable.

In order to be consistent with the measurement of θ, we measure ϕ at an equal distance from the tip where also θ was measured in the side view. The angle is measured from the intersecting tangent lines to both sides of the v-shaped contact line. The tangent lines are obtained by a similar method as used in determination of the dynamic contact angle.

Figures 2.6a shows the measured values of ϕ of both experimental data sets. Clearly, the angle ϕ decreases with increasing capillary number. The shift in Ca is once more related also to the difference in surface wettability for the turntable

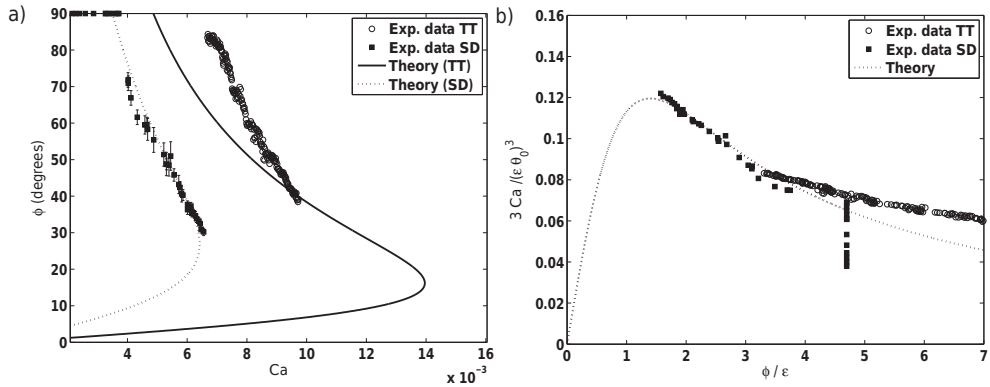

Figure 2.6: The measured opening angle ϕ as a function of the capillary number Ca. The circles and squares shown represent the measured value of ϕ for the turntable setup (TT) and the sliding droplet experiments (SD). While the lines are the predictions based on the simplified form of (2.3). a) measured angle ϕ versus Ca on a normal linear scale. b) Normalized Ca versus the normalized ϕ. Ca rescaled by θ_0 and ε ($\varepsilon = 1/\sqrt{\ln(x/\ell)}$) versus ϕ rescaled by ε.

experiments and sliding drop experiments. As suggested by [17], however, the data can be rescaled by using the lubrication prediction (2.3). This is shown in figure 2.6b, giving a reasonable collapse of the two sets of data. We remark, however, that the theory significantly overestimates the critical speed for drop deposition.

Our simultaneous measurement of ϕ and θ also allows for an experimental verification of the remarkable relation between both angles as given by (2.2). In figure 2.7, the experimental data of the turntable setup is plotted as circles together with the approximate analytical solution (2.2) and the exact numerical solution, represented as dashed and solid lines respectively. The trend is very similar and is almost comparable to the data from sliding droplet experiments done by Peters et al. [20]. However, it should be emphasized that these authors measure ϕ at a more distant position from the tip, which might be a cause for the appreciable shift of the data, compared to theory, that was less obvious in previous investigations from Le Grand et. al. [14, 16].

2.5 Discussion

In this chapter we compared v-shaped receding contact lines appearing in Immersion Lithography to the tails of drops sliding down an incline. We monitored the

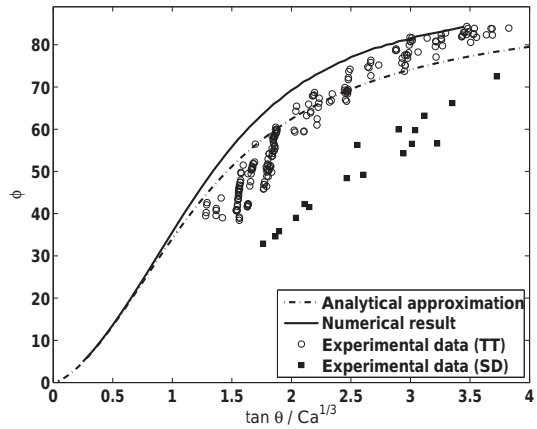

Figure 2.7: Opening angle ϕ versus $\tan(\theta)/\mathrm{Ca}^{1/3}$, to compare the experimental data with the approximate analytical result (2.2), shown as a dashed line. The solid line is the full numerical solution of the self-similar corner model [15]. Experimental data are shown as circles and squares from the turntable setup (TT) and sliding droplet setup (SD), respectively.

interface shapes for increasing contact line speed, using side view and bottom view imaging. We found that the receding contact lines in both systems behave very similarly, despite the difference in liquids (water versus silicon oil) and the difference in contact line driving. In particular, we find that the contact angle departs from the Cox-Voinov behaviour when the corner shape sets in, which can be attributed to a change from a two-dimensional to a fully three-dimensional interface. This transition is well described by a corner model based on the lubrication approximation, previously proposed for sliding drops.

There is, however, an interesting quantitative difference between water and silicon oil. For water, the logarithmic factor of the Cox-Voinov relation was found to be very large, $\ln(x/\ell) \approx 24$. Namely, this would imply a rather unphysical value for the microscopic length $\ell \approx 9.4 \cdot 10^{-16}$ m at which the viscous singularity is regularized. Similar values were found for sliding water drops [13], so we believe it to be due to the liquid rather than to the experimental configuration. A plausible explanation for this discrepancy lies in the relatively low viscosity of water – typical Reynolds numbers based on the drop size are of order $\mathcal{O}(100)$. By contrast, inertial effects are not important for the more viscous silicon oil drops, nor are they taken into account in the lubrication description. Despite this, our measurements of corner tip curvature do provide strong support for a 'viscous' logarithmic dissipation factor, also in the

case of water: the exponential increase of curvature arises from inversion of the logarithm, and is indeed confirmed experimentally. Secondly the complex droplet inner- and droplet outer-flow in the turntable experiment (with possible effects on evaporation and interface shape) is not completely understood. These intriguing issues deserve to be explored in future work.

References

[1] D. Bonn, J. Eggers, J. Indekeu, J. Meunier, and E. Rolley, "Wetting and spreading", Rev. Mod. Phys. **81**, 739 (2009).

[2] J. C. Berg, *Wettability* (Marcel Dekker, New York) (1993).

[3] T. Blake, R. Dobson, and K. Ruschak, "Wetting at high capillary numbers", Journal of Colloid and Interface Science **279**, 198–205 (2004).

[4] O. V. Voinov, "Hydrodynamics of wetting [english translation]", Fluid Dynamics **11**, 714–721 (1976).

[5] R. G. Cox, "The dynamics of the spreading of liquids on a solid surface. part 1. viscous flow", J. Fluid Mech. **168**, 169–194 (1986).

[6] B. V. Deryaguin and S. M. Levi, *Film Coating Theory* (Focal, London) (1964).

[7] J. Eggers, "Hydrodynamic theory of forced dewetting", Phys. Rev. Lett. **93**, 094502 (2004).

[8] L. D. Landau and B. V. Levich, "Dragging of a liquid by a moving plate", Acta physico-chimica USSR **17**, 42 (1942).

[9] R. Golestanian and E. Raphaël, "Relaxation of a moving contact line and the landau-levich effect", Europhys. Lett. **55**, 228–234 (2001).

[10] J. H. Snoeijer, G. Delon, M. Fermigier, and B. Andreotti, "Avoided critical behavior in dynamically forced wetting", Phys. Rev. Lett. **96**, 174504 (2006).

[11] J. H. Snoeijer, B. Andreotti, G. Delon, and M. Fermigier, "Relaxation of a dewetting contact line part 1: A full-scale hydrodynamic calculation", J. Fluid Mech. **579**, 63 (2007).

[12] T. D. Blake and K. J. Ruschak, "A maximum speed of wetting.", Nature **282**, 489–491 (1979).

[13] T. Podgorski, J. M. Flesselles, and L. Limat, "Corners, cusps, and pearls in running drops", Phys. Rev. Lett. **87**, 036102(1)–(4) (2001).

[14] N. Le Grand, A. Daerr, and L. Limat, "Shape and motion of drops sliding down an inclined plane", J. Fluid Mech. **541**, 293–315 (2005).

[15] L. Limat and H. A. Stone, "Three-dimensional lubrication model of a contact line corner singularity", Europhys. Lett. **65**, 365 (2004).

[16] J. H. Snoeijer, E. Rio, N. Le Grand, and L. Limat, "Self-similar flow and contact line geometry at the rear of cornered drops", Phys. Fluids **17**, 072101 (2005).

[17] J. Snoeijer, N. Le Grand, L. Limat, H. A. Stone, and J. Eggers, "Cornered drop and rivulets", Phys. Fluids **19**, 042104 (2007).

[18] J. H. Burnett, S. G. Kaplana, E. L. Shirleya, P. Tompkins, and J. E. Webb, "High-index materials for 193 nm immersion lithography", Proceedings of SPIE 5754, Optical Microlithography XVIII **5754** (2005).

[19] M. Riepen, F. Evangelista, and S. Donders, Proceedings of the 1st European Conference on Microfluidics (2008).

[20] I. R. Peters, J. H. Snoeijer, A. Daerr, and L. Limat, "Coexistence of Two Singularities in Dewetting Flows: Regularizing the Corner Tip", Phys. Rev. Lett. **103** (2009).

[21] C. Huh and L. E. Scriven, "Hydrodynamic model of steady movement of a solid/liquid/fluid contact line", J. Coll. Int. Sci. **35**, 85–101 (1971).

[22] E. L. Decker, B. Frank, Y. Suo, and S. Garoff, "Physics of contact angle measurement", Colloids and Surfaces **156**, 177–189 (1999).

[23] E. B. Dussan V., E. Ramé, and S. Garoff, "On identifying the appropriate boundary condition at a moving contact line: an experimental investigation", J. Fluid Mech. **230**, 97 (1991).

[24] J. A. Marsh, S. Garoff, and E. B. Dussan V., "Dynamic contact angles and hydrodynamics near a moving contact line", Phys. Rev. Lett. **70**, 2778–2781 (1993).

[25] J. Canny, IEEE Transactions on Pattern Analysis and Machine Intelligence **8**, 679 – 698 (1986).

[26] M. Maleki, E. Reyssat, D. Quéré, and R. Golestanian, "On the landau-levich transition", Langmuir **23**, 10116 (2007).

3

Unsteady contact line motion *

The dynamics of contact lines is usually characterized by the velocity at which the contact line moves over a substrate. However, many applications have to deal with contact lines that experience significant acceleration. Here we study such unsteady contact line motion using a geometry relevant for Immersion Lithography, in which a drop of water attached to a needle is forced to move over a substrate. We find that for small accelerations, the unsteady dynamics is accurately described by a quasi-steady model – the only relevant parameter is the instantaneous speed of the contact line with respect to the substrate. The quasi-steady regime extends to large velocities and accelerations, up to 0.5 m/s^2, which is surprising given the low viscosity of water. In addition we determine the bifurcation diagrams of the forced wetting transition. Surprisingly, the critical velocity depends on the drop volume while the dynamic contact angle does not. This illustrates that the outer flow geometry can significantly influence the critical velocity, beyond the usual Cox-Voinov law for contact line dynamics.

3.1 Introduction

The critical speed for contact line motion forms an important limitation in many applications that involve wetting of liquid on a substrate [1–4]. Beyond the criti-

*In preparation: K.G. Winkels, M. Riepen and J.H. Snoeijer, "Unsteady contact line motion".

cal speed, the contact lines are unstable with respect to droplet deposition [5, 6] or film pulling [7–9]. A simplified picture of this dynamical wetting transition is that the critical velocity arises when the dynamic contact angle becomes zero. This was shown experimentally [10, 11] by the withdrawal of a fiber from a liquid reservoir. In a more rigorous theoretical study by Eggers [12] on dip-coating, it was shown

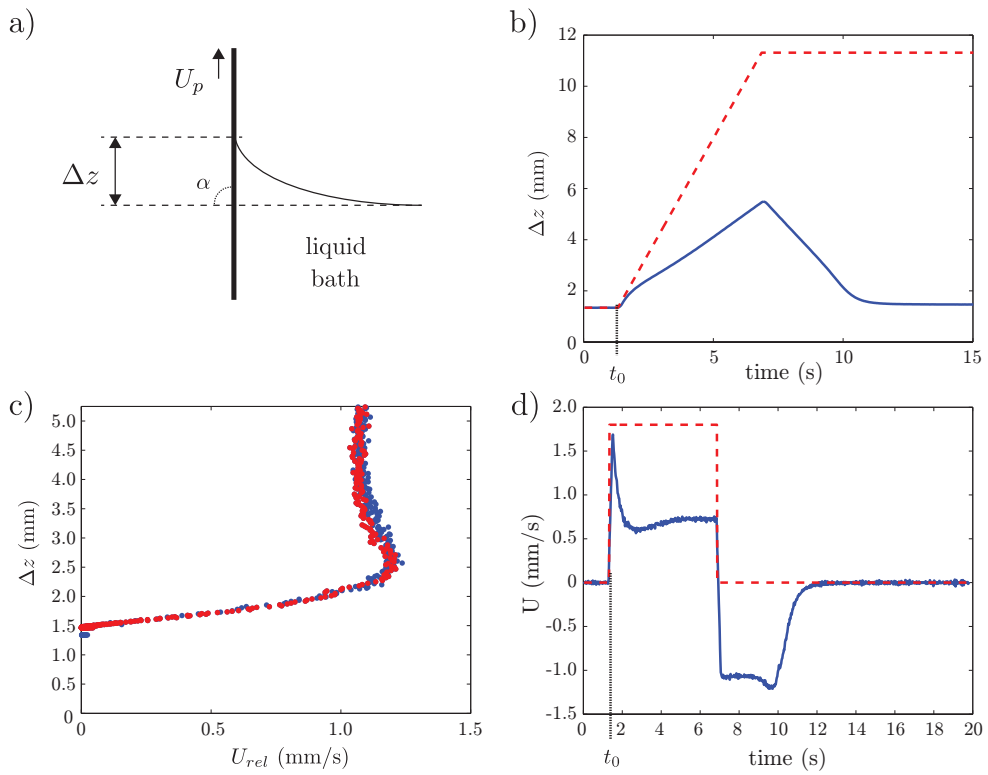

Figure 3.1: Illustrating experiment of quasi-steady dynamics. a) Schematic of a plate with-drawn from a liquid bath with velocity U_p. The contact line dynamics determines the meniscus height above bath surface Δz. b) The evolution of a fixed position on the plate (dashed line) and the meniscus height (solid line) are shown as a function of time. The plate motion is set to a velocity $U_p > U_{cr}$. c) Position of the contact line Δz as a function of the contact line velocity with respect to the plate, $U_{rel} = U_p - \Delta\dot{z}$. d) Velocity of the plate U_p (red dashed line) and the velocity of the contact line (blue solid line) in the camera reference frame.

that the critical velocity is actually determined by the interplay between small scale and large scale fluid motion. The dip-coating geometry consists of a plate that is

withdrawn from a liquid reservoir under an angle α, as shown in figure 3.1a. Very close to the contact line, the flow is determined by a balance between surface tension and viscosity. At larger scales, the interface has to match the large scale geometry, which for dip-coating is a large reservoir at equilibrium. The importance of the outer geometry was further emphasized by Ziegler et al. [13], who found that the critical velocity strongly depends on the inclination angle α [13], in particular for small α. Such a dependence is beyond the usual logarithmic dependence on microscopic and macroscopic parameters [14–16]. Interestingly, nearly all studies on moving contact lines consider motion at constant velocity. For many practical applications, however, accelerations can be substantial and one naturally wonders to what extent this affects the contact line motion. Such unsteady contact line motion was addressed by [17–20], who investigated relaxation towards an equilibrium position. By assuming a "quasi-steady dynamics", in which the contact line slowly evolves through a succession of nearly steady shapes, one can actually predict the rate of relaxation for very viscous liquids [19, 20].

To illustrate the principle of quasi-steady dynamics, we briefly discuss the results of a dip coating experiment for a highly viscous silicone oil [†]. The motion of the plate and that of the contact line is plotted as a function of time in figure 3.1b) and d). Panel b) shows the meniscus position Δz while panel d) gives the contact line velocity $\Delta\dot{z}$ in the frame of the reservoir (solid lines). At time t_0, the plate starts to move upwards from the liquid bath with an almost instantaneously reached constant velocity (dashed line). The plate velocity is above the critical speed, so that the meniscus can not attain a stationary position. Driven by the plate motion, the meniscus height increases with time. After a short transient, the contact line establishes a well-defined velocity: the contact line moves upwards with respect to the bath, but downwards with respect to the plate, since $\Delta\dot{z}$ is always smaller than the plate velocity U_p. Then, at $t = 7$ s, the plate velocity is set to zero, and the contact line relaxes back to its equilibrium position. From a physical perspective, the forcing of the liquid is imposed by the *relative* motion of the contact line with respect to the plate. It is therefore interesting to plot the meniscus height Δz versus $U_{rel} = U_p - \Delta\dot{z}$, the contact line speed with respect to the plate. The result is shown in figure 3.1c), both during the start-up of the plate (blue) and during the phase where the plate is stopped (red). Clearly, the contact line dynamics is identical during both phases, and can be characterized by a unique curve. One clearly observes a maximum velocity, which determines the critical speed at which steady menisci can be maintained.

The observations above suggest a quasi-steady motion of the receding contact

[†]These experiments were carried out during a short internship at the ESPCI in Paris, in collaboration with Bruno Andreotti and Antonin Marchand.

line, where the speed of the contact line with respect to the bath can be described by a function $f(\Delta z)$ [19, 20]. Hence, we can write

$$U_{rel} = U_p - \Delta\dot{z} = f(\Delta z) \Rightarrow \Delta\dot{z} = U_p - f(\Delta z), \tag{3.1}$$

which can be considered an evolution equation for $\Delta z(t)$. The function $f(\Delta z)$ is directly given by the bifurcation curve shown in figure 3.1c). For sliding velocities below the critical velocity ($U_{rel} < U_{cr}$), the contact line can stabilize at a position Δz_0. Since in that case $\Delta\dot{z}_{cl} = 0$, one simply finds

$$U_p = f(\Delta z_0). \tag{3.2}$$

The stability of these steady solutions can be assessed by a linear stability analysis, where we consider perturbations $\Delta z(t) = \Delta z_0 + A \cdot e^{\sigma t}$. This gives

$$\sigma A e^{\sigma t} = U_p - f(\Delta z_0) - \frac{df}{d\Delta z} A e^{\sigma t} \Rightarrow \sigma = -\frac{df}{d\Delta z}. \tag{3.3}$$

This shows that the stability only depends on the slope of the bifurcation function (stable for positive slope $df/d\Delta z > 0$ and unstable for a negative slope $df/d\Delta z < 0$) and that the relaxation time $1/\sigma$ diverges when U_p approaches U_{cr}. Note that the bifurcation curve $f(\Delta z)$ itself depends on the wetting characteristics of the substrate and the outer geometry of the problem [13].

In this Chapter, we investigate whether the quasi-steady approach can be applied to unsteady contact line motion in the context of immersion lithography. Besides differences in geometry, the working fluid for immersion lithography is typically water, which has a much smaller viscosity than the silicone oils typically used in dip-coating studies.

3.2 Experimental setup

To study receding contact lines, a turntable setup is used (see figure 3.2 a). While sliding drops normally move through the reference frame of the camera, the liquid drop in the turntable setup is fixed in the reference frame of the cameras. A glass wafer (300 mm diameter) is rotated at controlled angular velocity and acceleration, while keeping the droplet (volume $\sim 10\mu L$) at a fixed position ($R \sim 145$ mm) from the center of rotation (i.e. droplet experiences an almost linear motion). To obtain a partial wetting substrate, the glass wafer is coated, having a static receding and advancing contact angle of 65° and 86°, respectively. To hold the droplet a simple stainless steel rod is used with sharp perpendicular edges. To control the drop volume, a micro drop generator (Microdrop MD-E-3000) is used to form a sessile drop

at the substrate. This sessile drop is formed out of multiple small droplets formed with the micro drop generator (65 μm radius). Controlling the number of drops, sets the sessile drop volume. Then the sessile drop is moved to the rod position, where it automatically wets the stainless steel. From that moment it is fixed in the camera reference frame. We simultaneously image the drop from the side and from below (figure 3.2). For side view imaging a high speed camera (Photron SA 1.1) is used in combination with a long distance microscope (Navitar 12X Zoom System). The bottom view is also obtained with a high speed camera, PCO QE 1200s, in combination with a Nikon 10X microscope Infinity Corrected objective. Resolutions of $\sim$4.2 μm/pixel (side) and $\sim$3.4 μm/pixel (bottom) are achieved. Typical recordings obtained from this setup are shown in figure 3.2b,c. Digital imaging analysis is used to detect the droplet boundary position. In both, bottom and side view recordings, this position is found with a convolution method searching for the largest intensity slope on sub-pixel level [21]. To avoid false detections, the edge detection is checked and verified by superposition on the original image. Experimental data is obtained

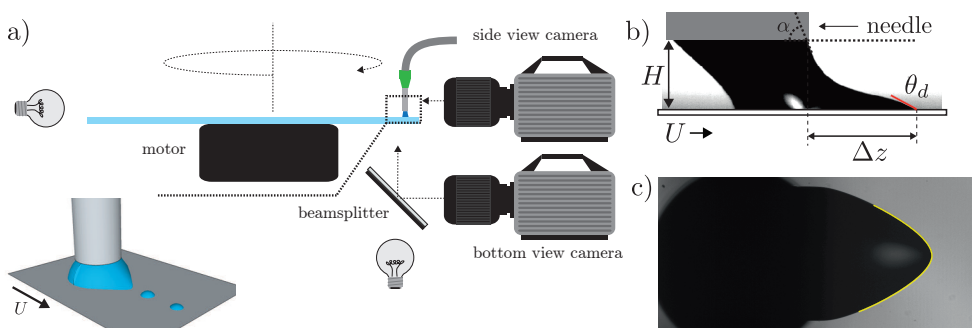

Figure 3.2: a) Turntable setup. Two cameras are synchronised to obtain a simultaneous side- and bottom-view. b,c) Bottom view and side view images from a typical measurement with an indication of the relevant experimental parameters. The contact line dynamics is characterised by the droplet tail length, Δz (with respect to the needle edge) and the dynamic receding contact angle, θ_d. The outer geometry is characterised by the angle α.

from multiple runs on different positions on the substrate in order to check the reproducibility. During each run we increase the velocity in steps or continuously up to 1 m/s, with varying acceleration from 0 - 0.5 m/s^2. The droplet is recorded simultaneously from the side and bottom, at a frame rate of 1000 fps. Depending on the accelerations and velocity protocol used, each image corresponds to a certain velocity. Hence, from a single recording it is possible to characterize the moving contact

line behaviour as a function of the wafer speed. The liquid used is water, which has a viscosity $1 \cdot 10^{-3}$ Pa s. Interestingly this means that typical Reynolds numbers based on velocity $Re \sim 1 - 100$ and based on acceleration $Re \sim 1 - 10$.

3.3 Experimental results

3.3.1 Quasi-steady dynamics

We first investigate whether the quasi-steady assumption also applies to the sliding drop geometry in the needle system, using a water drop. In this experiment, the velocity is increased in small steps (with acceleration: 0.5 m/s^2), with a duration of $\delta t =$ 0.05 s for each velocity (see figure 3.3). With this protocol, we ensured that $\delta t \gg 1/\sigma$ for the most of the selected velocities, such that the contact line has time to relax to an equilibrium position during the phases where the velocity is kept constant. Three separate measurements for one drop volume and one velocity protocol are shown in figure 3.3 – the collapse of data shows the reproducibility of the measurement.

We first measure the dynamics of the contact line position Δz, as defined in figure 3.2. The position is shown as a function of time in figure 3.3b). The green points correspond to the constant velocity periods, while the blue points represent the phases where the plate is accelerated. Similar to dip-coating, the tail length of the drop increases with velocity and remains at a constant position when the plate velocity remains constant. However, one clearly observes a critical velocity U_{cr}, where the tail length increases quickly in length and no longer equilibrates. We now investigate whether the step-wise motion of the contact line and the appearance of a critical speed can be captured by a single bifurcation curve. We therefore plotted the same data, as a function of the contact line velocity with respect to the plate $U_{rel} = U - \Delta\dot{z}$. The result is shown in figure 3.3d. In this plot, the periods of constant velocity appear as single points (green), while the dynamics during acceleration phases (blue) smoothly joins these steady states. This confirms that the acceleration dynamics is indeed quasi-steadily following the steady states. An additional feature is that one clearly identifies a maximum velocity, indicated by the vertical dashed line, beyond which no steady solutions can exist.

We also determined the dynamic contact angle, measured by a linear fit over the edge points within $\sim 30\ \mu m$ of the contact line. The results is shown in figure 3.3c). The angle decreases with speed as expected from the hydrodynamic description. The critical contact line velocity measured from the bifurcation diagram, does not appear at a zero contact angle.

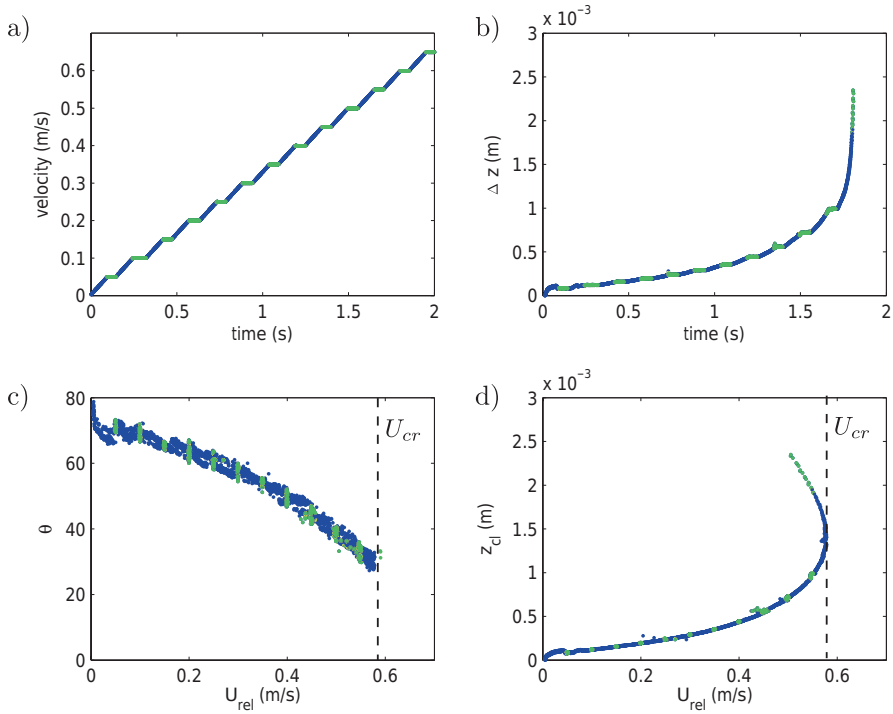

Figure 3.3: Verification quasi-steady dynamics. The green and blue data points correspond with constant velocity and constant acceleration respectively. a) Velocity protocol used, i.e step wise velocity increase. b) Tail length Δz as a function of time. At constant velocity the tail relaxes to a fixed length. c) Measured dynamic contact angle. d) Bifurcation curve with Δz as a function of the velocity of the contact line with respect to the plate U_{rel}. The critical velocity is indicated by the vertical dashed line at U_{cr}.

3.3.2 Critical velocity (volume dependence)

One important observation in our experiments is that upon varying the droplet volume, we found a significant change in the critical velocity (while other experimental parameters are held constant). To further investigate this, we used the measurement procedure that is shown in figure 3.4a). The velocity of the substrate is increased with constant acceleration to a value just above the critical velocity (for the initial volume) and kept constant for a time T. The drop tail elongates, i.e. Δz increases with time. As a result the rivulet structure that is formed out of the drop tail becomes

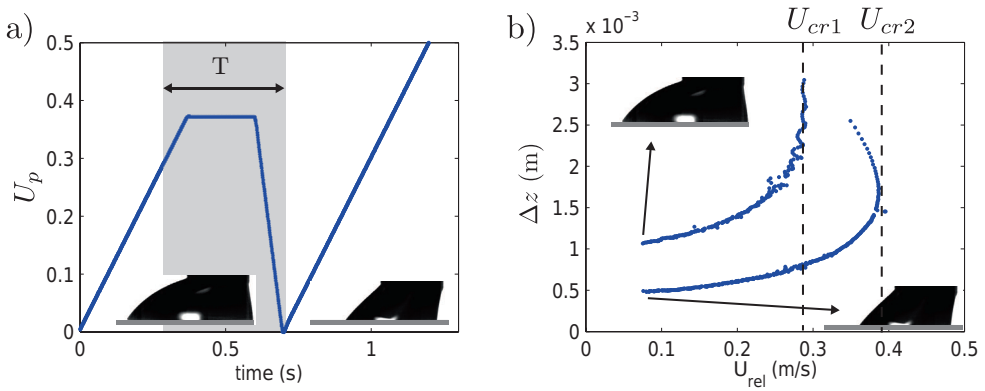

Figure 3.4: Influence of initial drop volume (inset images) on the critical velocity. a) Velocity protocol. b) Drop tail length Δz as a function of the contact line velocity with respect to the plate. All other parameters but volume is kept constant. For small drop volume (U_{cr2}) the critical velocity is higher than large drop volume (U_{cr1}).

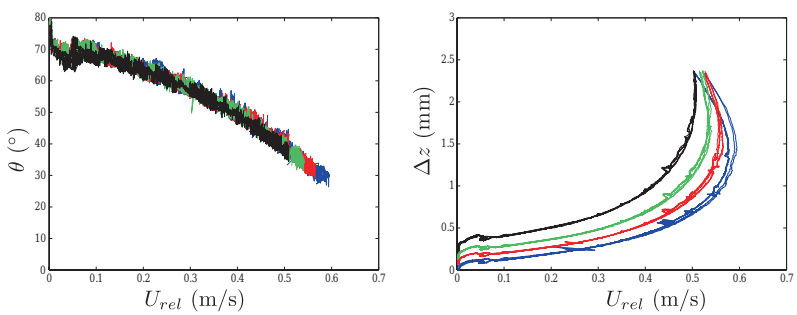

Figure 3.5: Contact line dynamics characterised by (a) the dynamic contact angle θ_d; and (b) tail length Δz. All plotted as a function of the contact line velocity with respect to the plate U_{rel}. The colors correspond with different drop volumes (expressed in number of microdrops): 5000 (blue), 6000 (red), 7000 (green), 8000 (black).

unstable and finally leads to break-up and deposition of smaller droplets on the substrate. Consequently, this instability reduces the volume of the drop. We then stop the motion of the substrate ($U = 0$), and subsequently apply a second acceleration run with the same drop of reduced volume. In figure 3.4 we show the two bifurcation curves, obtained once more by plotting Δz as a function of U_{rel}. Clearly, the drop of smaller volume has a different bifurcation curve and one can reach a new (higher) critical velocity U_{cr2}. This suggest that different critical velocities appear for differ-

ent volumes or outer geometry, for exactly the same microscopic characteristic such as wettability.

The volume dependence was further explored by performing experiments with controlled volumes, using the microdrop device. All other experimental control parameters are held constant and five runs are made for four different drop volumes (5000, 6000, 70000 and 8000 microdops). The experimentally obtained bifurcation diagrams are very reproducible, and independent of velocity protocol. Typical results are shown in figure 3.5b. All results clearly show that the critical velocity increases as the volume decreases. Contrarily to the volume dependence of the critical speed, the

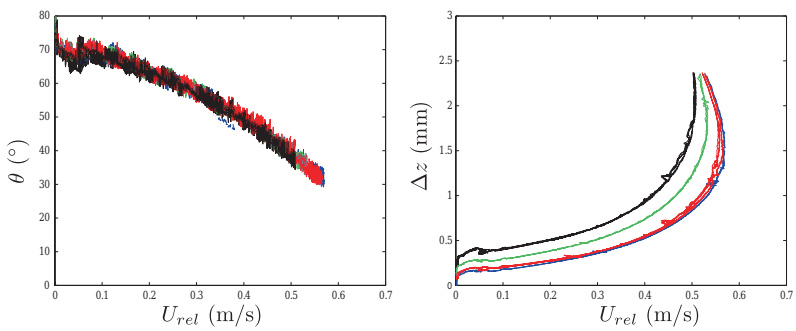

Figure 3.6: Contact line dynamics characterised by (a) the dynamics contact angle θ_d; and (b) tail length Δz. All plotted as a function of the velocity of the contact line with respect U_{rel}. In this experiment the needle height is changed for two different droplet volumes (denoted in number of microdrops). In both cases the critical velocity increases with gapwidth ($NH1 \sim 500\mu m$: 6000 (red), 8000 (black); $NH2 \sim 610\mu m$: 6000 (blue), 8000 (green)).

dynamic contact angle is completely unaffected by the drop volume. As can be seen from figure 3.5a), the dynamic contact angle measurements for the different volumes collapse.

An alternative method to investigate the effect of outer geometry is to vary the gap height H in between the drop holder and the substrate. For two different drop volumes, the bifurcation curves are made for two different gap heights. The results are shown in figure 3.6. Also for constant volume and different gap height, there exist differences in the critical velocity. Clearly the critical dewetting velocity is not only a function of the volume but there is a more detailed dependence on the outer geometry. Again, the dynamic contact angle is not sensitive to macroscopic changes. This shows that for our experiments, the dynamic contact angle carries no information on the critical velocity.

3.4 Discussion

In this Chapter we experimentally studied unsteady motion of sliding drops, for a system that is reminiscent to the geometry of immersion lithography. Despite the small viscosity of water, we found that the unsteady motion evolves according to "quasi-steady" profiles: for all our experiments, the relative velocity of the contact line with respect to the plate is determined purely by the position of the meniscus. For the accelerations used in the experiments, no unsteady effects were observed. This suggests that the concept of quasi-steady contact line dynamics, which was previously observed for dip-coating, can be applied to a broad class of contact line geometries.

Surprisingly, we observed an unexpectedly large dependence of the critical speed on the volume and/or geometry of the drop held below the needle. This could result from inertial effects, however, the Reynolds number based e.g. on the needle height is not affected by a volume change. Instead, we provide a tentative explanation in terms of the geometry of the meniscus, which is affected by the drop volume. For this, we

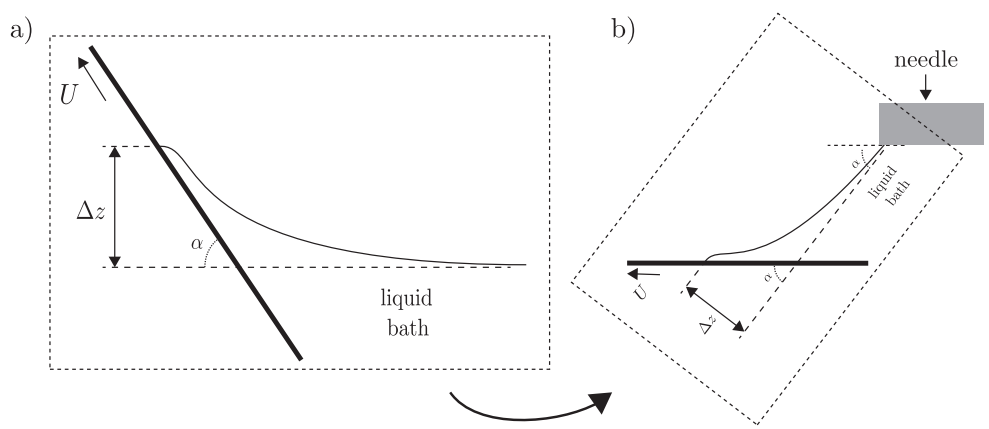

Figure 3.7: Analogy dipcoating and the system reminiscent with immersion lithography. a) Schematic typical dip coating experiment. b) Schematic of a sliding drop held by a rod or needle.

once more attempt an analogy to dip-coating, a geometry for the wetting transition is much better understood. This analogy is sketched in figure 3.7, where we relate the inclination angle of the plate in dip-coating (panel a) to the angle at which the meniscus arrives at the needle in the immersion lithography setup (panel b). While we do not wish to claim a perfect correspondence between the two systems, e.g. the liquid reservoir is infinite in dip-coating, it is known that the large scale meniscus

geometry is crucial in determining the critical speed [12, 13].

For the present experiments, a larger drop volume or smaller height H naturally leads to a smaller α. In one measurement run, typically α decreases with velocity and it turns out, that at a point before instability it reaches a minimum value α_{min}. Here we determine α_{min} as a function of the critical velocity determined from the bifurcation diagrams (see figure 3.8). The critical velocity increases with increasing

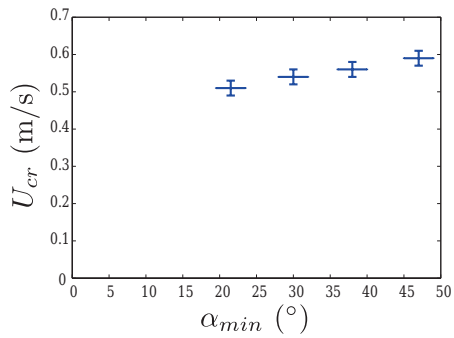

Figure 3.8: The critical velocity U_{cr} as a function of α_{min} (the characterisation of the outer scale boundary condition).

value of angle α_{min}. Indeed, this is in accordance with Ref. [13], where it was shown numerically the bifurcation diagram changes considerably for the plate withdrawing angle α: the critical velocity increases with α. In the dip-coating case, one even observed a dramatic decrease in U_{cr} as the angle α is further decreased to values much smaller than the wetting angle. This qualitative agreement emphasizes the strong connection between local microscopic contact line dynamics that needs to match an outer scale flow. Essentially, both boundary conditions are important in determining the critical velocity of dewetting. Note, that the present arguments have focussed on a two-dimensional flow situation, while our experimental system is truly three-dimensional with a possibility to form corners as well (as observed in chapter 2). In the results presented in this chapter, sharp corners were formed only for very small drops. It remains an open question under what conditions corners can form when approaching the critical dewetting speed.

References

[1] H. Burnett, T. Shedd, G. Nellis, M. El-Morsi, R. Engelstad, S. Garoff, and K. Varanasi, “Control of the receding meniscus in immersion lithography”, vol-

ume 23, 2611–2616 (AVS) (2005).

[2] H. Wijshoff, "The dynamics of the piezo inkjet printhead operation", Physics Reports **491**, 77–177 (2010).

[3] M. Riepen, F. Evangelista, and S. Donders, Proceedings of the 1st European Conference on Microfluidics (2008).

[4] K. G. Winkels, I. R. Peters, F. Evangelista, M. Riepen, A. Daerr, L. Limat, and J. Snoeijer, "Receding contact lines: From sliding drops to immersion lithography", Eur. Phys. J. Special Topics **192**, 195 (2011).

[5] N. Le Grand, A. Daerr, and L. Limat, "Shape and motion of drops sliding down an inclined plane", J. Fluid Mech. **541**, 293–315 (2005).

[6] J. Snoeijer, N. Le Grand, L. Limat, H. A. Stone, and J. Eggers, "Cornered drop and rivulets", Phys. Fluids **19**, 042104 (2007).

[7] L. D. Landau and B. V. Levich, "Dragging of a liquid by a moving plate", Acta physico-chimica USSR **17**, 42 (1942).

[8] T. D. Blake and K. J. Ruschak, "A maximum speed of wetting.", Nature **282**, 489–491 (1979).

[9] A. Koulago, V. Shkadov, D. Quéré, and A. Deryck, "Film entrained by a fiber quickly drawn out of a liquid bath", Phys. Fluids **7**, 1221–1224 (1995).

[10] R. V. Sedev and J. G. Petrov, "Influence of geometry on steady dewetting kinetics", Colloids and Surfaces **62**, 141–151 (1992).

[11] J. G. Petrov, R. V. Sedev, and P. G. Petrov, "Effect of geometry on steady wetting kinetics and critical velocity of film entrainment", Advances in Colloid and Interface Science **38**, 229 – 269 (1992).

[12] J. Eggers, "Hydrodynamic theory of forced dewetting", Phys. Rev. Lett. **93**, 094502 (2004).

[13] J. Ziegler, J. H. Snoeijer, and J. Eggers, "Film transitions of receding contact lines", Eur. Phys. J. Special Topics **166**, 177 (2009).

[14] O. V. Voinov, "Hydrodynamics of wetting [english translation]", Fluid Dynamics **11**, 714–721 (1976).

[15] R. G. Cox, "The dynamics of the spreading of liquids on a solid surface. part 1. viscous flow", J. Fluid Mech. **168**, 169–194 (1986).

[16] P.-G. de Gennes, "Wetting: statics and dynamics", Rev. Mod. Phys. **57**, 827–863 (1985).

[17] T. Ondaruhu and M. Veyssi, "Relaxation modes of the contact line of a liquid spreading on a surface", Nature **352**, 418420 (1991).

[18] R. Golestanian and E. Raphaël, "Relaxation of a moving contact line and the landau-levich effect", Europhys. Lett. **55**, 228–234 (2001).

[19] J. H. Snoeijer, B. Andreotti, G. Delon, and M. Fermigier, "Relaxation of a dewetting contact line part 1: A full-scale hydrodynamic calculation", J. Fluid Mech. **579**, 63 (2007).

[20] G. Delon, M. Fermigier, J. H. Snoeijer, and B. Andreotti, "Relaxation of a dewetting contact line part 2: Experiments", J. Fluid Mech. **604**, 55 (2008).

[21] A. Marchand, "Mouillage statique et dynamique : Influences géométriques aux échelles moléculaires", Ph.D. thesis, Université Paris VII (2011).

4

Drop emission by receding contact lines *

The shape of a sliding drop on a partially wetting substrate strongly depends on its sliding velocity. With increasing sliding speed, the receding tail of the drop elongates and changes from a rounded shape into a cornered shape. Such a receding contact line remains stable up to a critical speed. However, exceeding this critical speed results in the ejection of a thin rivulet from the cornered tail, which finally breaks up into smaller droplets. We experimentally investigate this break-up process with high-speed imaging and show that there are indeed two separate physical phenomena involved. First, there is a topological transition from a mass conserving dewetting corner to a geometry where a rivulet is ejected with a net outflux of liquid. Second, this rivulet breaks into small sessile droplets. Our experiments show that the width of the rivulet depends on the sliding velocity: the rivulet width tends to zero when approaching the critical contact line speed. We show that the size of the emitted droplets is determined by this rivulet width, implying that the droplet size vanishes as well at the critical speed. We investigate to what extent the drop formation can be described by a Rayleigh-Plateau instability, and point out some differences due to the presence of a contact line.

*To be submitted as: K.G. Winkels, A. Eddi and J. H. Snoeijer, *Drop emission by receding contact lines*.

4.1 Introduction

Drop formation is a widely studied subject [1, 2] with many different applications. The detailed fluid mechanics of drop formation has been investigated extensively for many different systems, such as break up of liquid jets and sheets [1, 3–5], or drops detaching from a dripping faucet. The resulting drop sizes, or distribution drop sizes [6], have been characterized experimentally in great detail and can in many cases be predicted from the underlying fluid mechanics. Applications such as spray formation or inkjet printing crucially rely on this knowledge to produce droplets at controlled rate and size [7]. Typically, the drop size is determined by the size of the nozzle from which a liquid jet is created, and follows from the most unstable wavelength of the Raleigh-Plateau instability [2, 8].

While drops usually result from the break-up of free jets, similar drop formation has been observed for (receding) contact lines [9–14]. In that case the break-up of the free surface is strongly affected by the presence of the solid boundary. As an illustration one can consider a liquid drop sliding down a partially wetting inclined plane. Upon increasing the sliding velocity, the rounded drop becomes increasingly pointy; the rear of the drop develops a corner-like shape and is characterized by a very large curvature at the tip [15]. This change in shape from "rounded" towards a "corner" effectively reduces the (normal) velocity of the contact line, and allows the drop to reach higher sliding velocities [10, 11, 16]. However, the sliding velocity of the main drop cannot be increased without instabilities. There is a critical velocity U_{cr} above which the receding corner becomes unstable, resulting in the deposition of static droplets on the substrate, also referred to as the "pearling" transition [9, 10, 17]. While the argument based on the normal velocity explains why corners appear, it can not explain the emission of droplets.

The drop formation problem for receding contact lines was addressed by Snoeijer et al. [17] who developed a model to describe the shape of the main drop in the pearling regime. The main result of this model is shown in figure 4.1, where the contour of a sliding drop is drawn for five different sliding velocities. Below the critical speed, the drop tail is well described by a conical shape [18–20] (arrow 1 and 2 in figure 4.1). In the reference frame co-moving with the drop, this solution satisfies the zero-flux condition, such that no liquid is deposited on the substrate. However, this solution ceases to exist above the critical speed (dashed drop contour figure 4.1). A new class of solutions emerge beyond the critical speed, which exhibit a finite liquid flux of liquid (arrow 3 and 4 in figure 4.1). Hence, instead of further reducing the corner angle, the new solutions result in the ejection of a thin rivulet from the cornered tail. It was shown in Ref. [17] that the rivulet width, w, depends

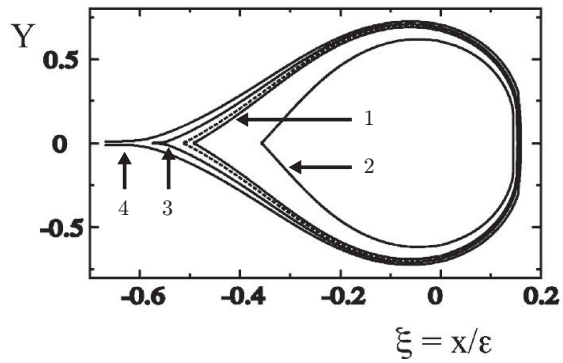

Figure 4.1: Theoretical solution of the top view contour of a sliding drop. Adapted from [17]. Arrow 1 and 2 indicate stable solutions for sliding velocities below the critical speed. Exceeding the critical speed (transition solution is indicated by the dashed line), results into rivulet solutions (arrow 3 and 4).

on the sliding velocity U as

$$w = \ell \exp \frac{-a}{\sqrt{U/U_{cr} - 1}}. \tag{4.1}$$

Here, the pre-factor ℓ is a typical outer length scale of the geometry such as the drop size, while the numerical constant $a = 1.0515$. Interestingly, this equation predicts that the width of the ejected rivulet becomes vanishingly small at the critical velocity, i.e. when the sliding velocity U is only slightly above the critical speed U_{cr}. This also implies that in principle one could produce rivulets and droplets of arbitrarily small size, by letting $U \to U_{cr}$.

These predictions, however, have not yet been tested experimentally in great detail, and the break-up phenomena of sliding drops have not been fully characterized. Interestingly, the instability of the rivulet that is emitted from the sliding drop is strongly reminiscent of the Rayleigh-Plateau break-up of a free jet that is not in contact with a substrate. Indeed, there exists a vast body of work on the stability of static cylindrical caps that are at rest on a solid substrate [21–24]. The driving mechanism for the instability is identical to that of Rayleigh-Plateau: a sinusoidal perturbation of the contact line reduces the capillary free energy for wavenumbers below a critical value k_c. While for cylindrical jets of radius R the critical wavenumber $k_c = 1/R$, a correction appears for finite contact angles [21, 24]. Details of the dispersion relation, such as the timescale for the instability and the maximally unstable wavenumber, will depend on the very viscous motion of the contact line. However, one still finds

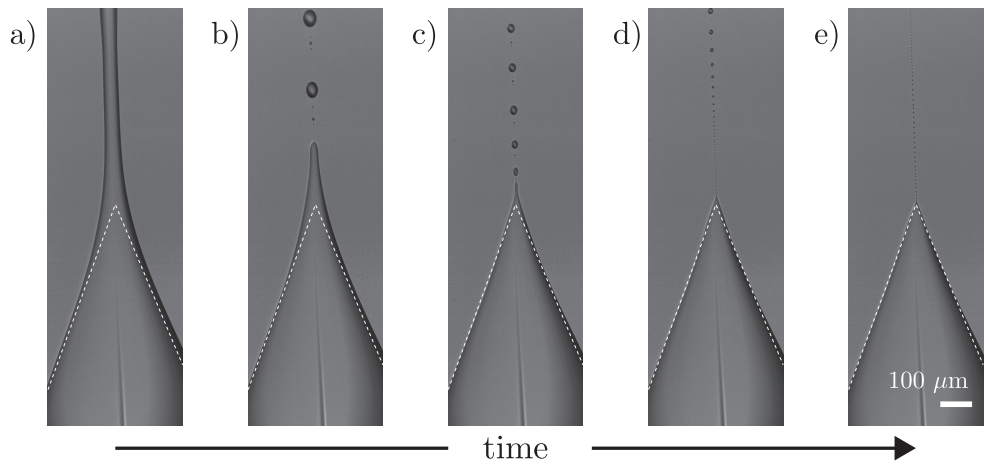

Figure 4.2: Bottom view of the rear of a sliding drop. The drop moves at a constant velocity $U < U_{critical}$, with a conical rear (white dashed lines). Due to a strong perturbation of the receding contact line, (a) a long rivulet is formed. (b-e) The tail relaxes back to its stable conical shape, while ejecting increasingly small sessile droplets.

$k_c \propto 1/R$, suggesting that the drop size should scale with the width of the rivulet. These features have indeed been addressed experimentally for the breakup of steady rivulets [25–28]. However, Gonzáles et al. [26] showed that the break-up of a finite rivulet is initiated at the ends of the liquid filament, and propagates towards the center. Such a break-up consists of successive stages of bulge growth and pinch-off at the ends of the strip. Details of break-up can in principle thus be more intricate than the stability analysis for an infinitely extended rivulet.

In this Chapter we experimentally investigate the dynamics of droplet emission by receding contact lines. By holding the drop below a needle, while the substrate moves below the drop, we are able to study receding contact lines in the frame of reference of sliding drops. The still images in figure 4.2, show that indeed the size of the emitted droplet size can change dramatically. In this figure, a time sequence of bottom view images is shown of a drop sliding in the downward direction at a constant velocity below the critical speed. Before the first image, the receding contact line was perturbed by a wetting defect (not visible in the image), and a long tail has formed at the rear of the drop (Fig. 4.2a). Once the receding contact line detaches from the defect, the tail relaxes back to its stable corner shape (indicated with the white dashed lines). Indeed, the observed shapes are very similar to theoretical predictions as shown in figure 4.1, in which a cornered drop tail is attached to a rivulet. The rivulet is unstable and breaks into increasingly small droplets moving with the

substrate. The goal of this study is to quantify the size of the drops, rivulets and the frequency of drop emission as a function of sliding velocity. In particular, we focus on the dynamics close to the critical velocity U_{cr}. The main questions we will address are whether or not the droplet size indeed vanishes at the critical velocity U_{cr}, and whether the dynamics can be understood from the analogy to the Rayleigh-Plateau instability.

The Chapter is organized as follows. The experimental setup is explained in section 4.2. In this section we define the measured quantities and provide details of the measurement protocol. Section 4.3 starts with a qualitative discussion of our experimental observations, and then quantifies the detailed dynamics of drop formation at different sliding velocities. Indeed, we find that the size of the emitted drops tends to zero at the critical speed, in accordance with (4.1). By comparing our results to the Rayleigh-Plateau instability, we point out some subtle effects that can be attributed to the presence of a contact line. The chapter ends with concluding remarks in section 4.4.

4.2 Experimental setup

To study the break-up process of the receding contact line of sliding droplets, a turntable is used as shown in figure 4.3. A glass wafer (300 mm diameter) is coated with 3M NovecTM Electronic Coating EGC-1700, which makes it partial wetting for the silicon oil used ($\theta_{adv} = 49^\circ$ and $\theta_{rec} = 41^\circ$). The wafer is clamped to an air bearing rotary stage (Aerotech ABRT 200), with which the wafer is rotated at controlled velocity (0 - 3.5 $^\circ/s$) and acceleration (0 - 0.5 $^\circ/s^2$). A silicon oil drop (Basildon Chemicals Silicone Fluid, density 953 kg/m^3, surface tension 20.8 mN/m, viscosity 20 cSt) is held by a EFD dispense tip (outer diameter 1.27 mm) fixed at ~ 240 μm above the substrate. The tip is connected to a Picoplus (Harvard Apparatus, USA) syringe pump to accurately control the drop volume. Since the drop size is of the order of ~ 1 mm and the position at the wafer is ~ 145 mm, the drop experiences an approximate linear motion. We simultaneously image the drop from the side and from below. For side view imaging a PCO1200s camera is used in combination with a long distance microscope (Navitar 12X Zoom System). The bottom view is obtained with a Photron SA1 in combination with a Navitar Zoom 6000. The corresponding resolutions are 2.7 μm/pixel (side) and 2.5 μm/pixel (bottom). The maximum frame rate used is 1000 fps. Typical side- and bottomview recordings obtained from this setup are shown in figure 4.4. In the side view (figure 4.4a), the substrate is indicated by a white dashed line. Both the drop and the needle are visible in the left of the image, and the drop ejects small satellite droplets at the tail. Below the white line, also

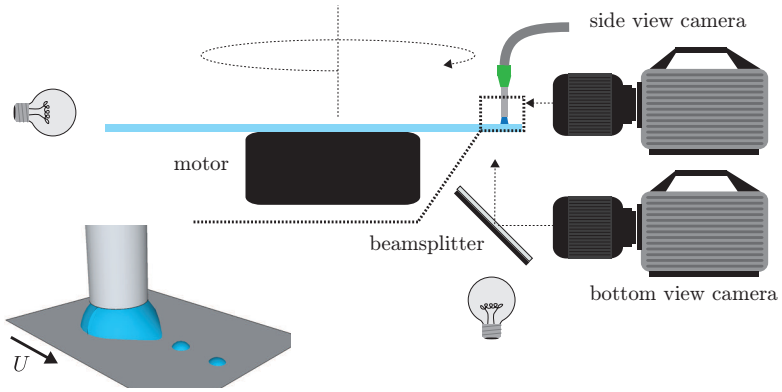

Figure 4.3: Sketch of the experimental setup to simultaneously visualize the side- and bottom-view of the break-up process of the drop tail. A coated glass wafer is rotated at controlled velocity while a needle is fixed in the camera reference frame. The bottom left inset shows how the needle holds a droplet in place, while the substrate moves below the drop. The camera is therefore in the co-moving frame of the droplet.

the mirror reflections in the substrate are visible. Both images are bright and the drop and droplets appear black. The orientation of the illumination and shape of the liquid sometimes result in diffraction and reflections, and bright parts inside and at the edge of the drop(lets) appear. The droplet motion is relative to the substrate which moves from left to right with velocity U in all images shown in this chapter. The velocities used vary from $\sim$0-8.5 mm/s, which corresponds to Reynolds numbers $Re < 1$.

If the main drop is forced to move above the critical speed, a tail is formed with width w, that breaks up into a trail of small sessile drops. Throughout the chapter we will call these sessile drops 'droplets' and refer to the main sliding drop as 'drop'. As can be observed clearly in the bottom view images (figure 4.4b), the droplet trail consists of two distinct droplet sizes. First we find large ellipsoidal droplets, with major diameter a and minor diameter b. To characterize the size of these droplets, we define the effective radius $R = \sqrt{ab}/2$. Typically the ellipticity is small, i.e. $\frac{a}{b} > 0.8$. Second, we observe the formation of small satellite droplets in between the large droplets, emerging from the pinch-off process. The break-up is quite regular, with droplet separation distance λ. Using custom made Matlab scripts, the position of the liquid edge is detected as the location where the intensity profile presents its maximum slope [29]. Then the droplet sizes are determined from fitting an ellipse to the detected droplet edge, giving the radius R and the position coordinates in the image. The separation distance λ is measured from the velocity of the substrate multiplied by the intermediate formation time. Only drop radii larger than the mean

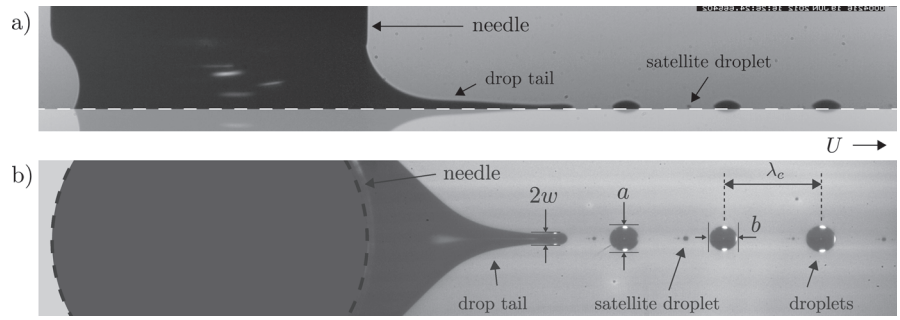

Figure 4.4: Definition of the parameters measured in this chapter. a) Typical snapshot of the side view during break-up. b) Simultaneous snapshot of the bottomview (scale: needle diameter is 1.27mm).

drop size in the image is taken into account. This condition is used to exclude any measurement with a satellite droplet, since satellite droplets result from a different physical process which is not subject of this study [30].

4.3 Results

4.3.1 Phenomenology

In the example described in figure 4.2, the contact line was perturbed strongly by a defect before the image of Fig. 4.2a. Once detached from the defect, this resulted in a relaxation of the contact line. In the experiments below we will not use perturbation by defects, but impose a well controlled velocity U at which the drop slides over the substrate. To study the dynamics of drop formation, we zoomed in on the receding part of the droplet and recorded its dynamics as a function of velocity. A few examples of recordings are shown in figure 4.5. From the top image to bottom image the plate velocity increases. The plate is moving from left to right and the drop and droplets turn black in the image. As is shown in image (a) of figure 4.5 the drop tail is stable and cone-like for $U < U_{cr}$. In this state no droplets are emitted from the tail. Increasing the velocity slightly above the critical velocity results in the formation of a thin rivulet structure that subsequently breaks into smaller droplets moving with the substrate. Although the entire break-up process is dynamic, the shape of the drop tail is rather steady and leads to a reproducible emission of droplets of well-defined size (figure 4.5b). Further increasing the velocity leads to larger rivulet widths w, increasing droplet size R and increasing distance between droplets λ (figure 4.5c-i).

We used different experimental protocols to quantify how these sizes depend on

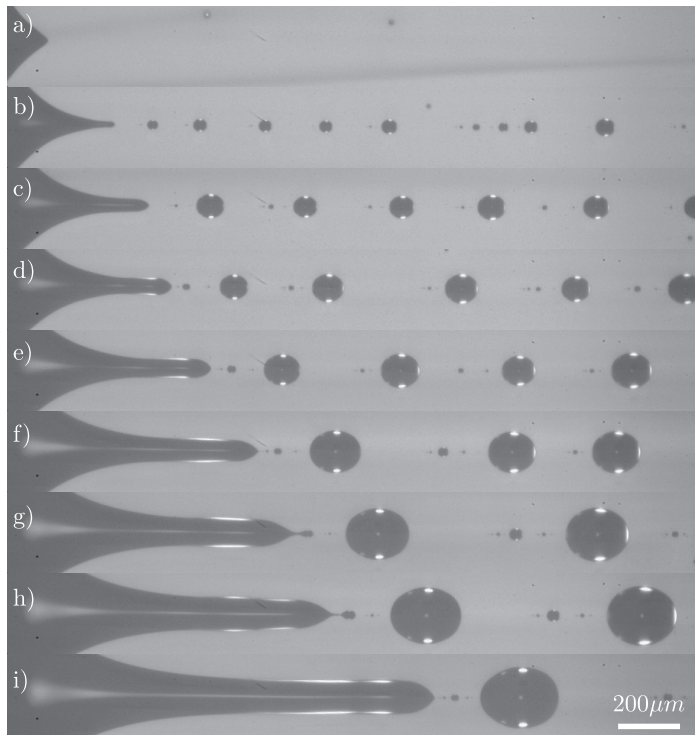

Figure 4.5: Typical tail (break up) for different velocities. a) Stable cornered tail ($U = 5.9$ mm/s). b-i) Unstable tail for increasing velocity ($U = 6.4; 6.6; 6.8; 7.1; 7.3; 7.5; 7.8; 8.1$ mm/s).

sliding velocity. First, a stepwise increase in velocity is applied. Starting below the critical velocity, the velocity is gradually increased with discrete steps up to about $1.4U_{cr}$. The duration of each step is taken much larger than the natural relaxation time of the contact line, such that we avoid transients due to the stepwise increase of the velocity. For each constant speed, we measure the width w, droplet radii R and droplet separation distance λ from the images. By varying the duration at which the velocities are kept constant, we have ensured that the small loss of volume of the main drop, due to the drop emission, does not significantly affect any of our results. In addition, we verified that there is no measurable hysteresis around the pearling transition. This was done by experiments where the velocity was decreased stepwise. Measurements are carried out at different parts of the wafer, excluding any possible bias due to local heterogeneity.

4.3.2 Rivulet width

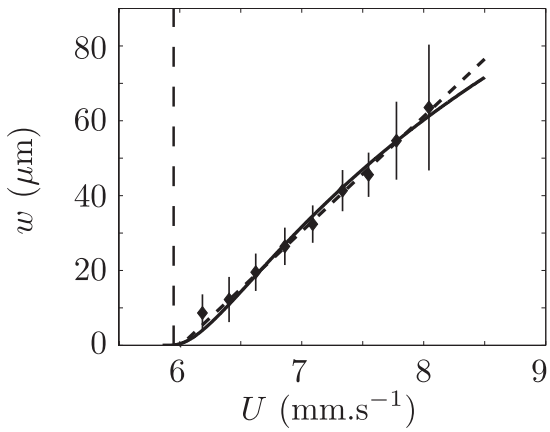

Figure 4.6: Drop tail width w measured as a function of velocity U. All datapoints represent averages over at least 5 independent experimental runs. The solid line corresponds with eq. 4.1 and the dashed line corresponds with eq. 4.2.

The results for the rivulet width are shown in figure 4.6. Up to the critical velocity (indicated by the vertical dashed line in figure 4.6) no rivulet is emitted from the drop. Above the critical velocity, the width is measured at the position where the rivulet is almost horizontal (slope boundary < 0.1), leading to a reproducible measurement. The figure clearly shows that the width increases in size with velocity. Close to the critical speed, the emitted rivulets are indeed very small and approach the limit of our experimental detection. Each data point at one velocity represents the mean over several measurements with different velocity protocols. For stepwise velocity increase, stepwise velocity decrease and constant velocities, measurements collapse onto a single curve.The error bars represent the maximum standard deviation either observed in a measurement per fixed velocity or from the set of mean data points.

The data are well-described by a simple linear fit of the type

$$w = \frac{U - U_c}{U_c}\ell, \tag{4.2}$$

where ℓ is a characteristic length scale and U_c the critical velocity. The fit is plotted in the figure as the black dotted line, with fitted parameters $U_c = 6$ mm/s and $\ell = 182$ μm. Similarly, the theoretical prediction (4.1) by Snoeijer et al. [17] can be fitted equally well, giving $U_c \approx 5.9$ mm/s and $\ell \approx 340$ μm (solid line in figure 4.6). The fitted values for ℓ are indeed of comparable magnitude to the natural length scale of

the experimental geometry: the size of the main drop $R \sim 590\ \mu m$, or the height of the the needle above the substrate $H \sim 242\ \mu m$. This indeed suggests that the rivulet size is governed by the distance to the critical point and the outer length scale of the main drop, as predicted in [17]. The remarkable mathematical structure of equation 4.1 close to U_{cr} is beyond experimental resolution.

4.3.3 Size and periodicity of emitted droplets

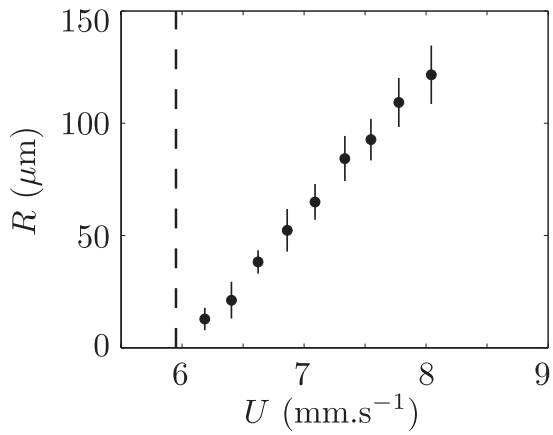

Figure 4.7: Droplet size R as a function of velocity U. All datapoints represent averages over at least 5 independent experimental runs.

We now turn to the size of the emitted drops, which is quantified in figure 4.7. Similarly to w, the droplet size can be tiny close to the critical point, $\sim 10\mu$m, approaching the limit of experimental detection. The data display the same trend as the rivulet width, increasing almost linearly with sliding velocity. As will be analyzed in detail below, this suggests that the drop size is selected by the width of the ejected rivulet.

At a given velocity, the droplets are ejected at a very repetitive rate. This results in a third length that can be measured, namely the wavelength λ which is the distance in between the main droplets. Due to a limited field of view, the values for λ are measured from the time in between two successive break-ups, multiplied with the velocity of the substrate. For small wavelengths, the validity of this method was confirmed by a direct comparison with the distance between two separated drops. The resulting λ versus speed is presented in figure 4.8. Once more the data suggest a vanishing length scale at the onset of drop formation, and a nearly linear dependence on drop speed.

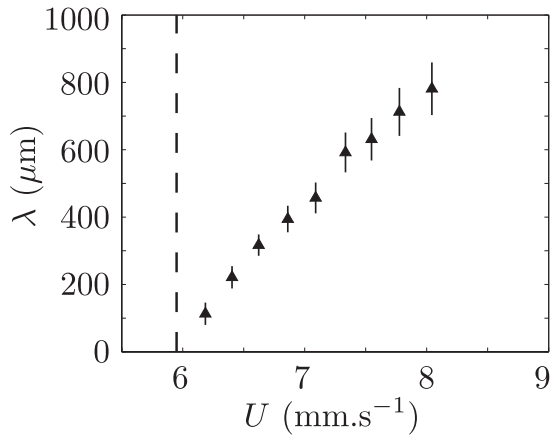

Figure 4.8: Distance between major droplets λ as function of velocity U. All datapoints represent averages over at least 5 independent experimental runs.

4.3.4 Rivulet stability and mechanism for drop formation

The results above suggest that the rivulet width w determines the characteristic scale for the droplet size R and separation λ. This is strongly reminiscent of the Rayleigh-Plateau instability of cylindrical jets, for which the cylinder radius R_0 determines the wavelength and droplet sizes. This stability analysis has been generalized from free jets to the case of rivulets on a solid substrate, with a contact angle θ_0 [21, 24] Here we explore whether this rivulet-instability can quantitatively account for our experimental observations.

For infinitely extended axisymmetric jets of radius R_0, long-wave surface modulations increase the capillary energy and thus lead to instability [31–33]. Elementary geometry shows that the critical wavelength $\lambda_c = 2\pi R_0$, above which free jets become unstable. In terms of the wavenumber the stability boundary becomes $k_c = 2\pi/\lambda_c = 1/R_0$. This geometric calculation has been extended to infinite cylindrical caps, as shown in figure 4.9a [21, 24]. The critical wavenumber is now a function of the contact angle, and follows from [24],

$$k_c^2 R_0^2 = 2\left[1 + \sin^2\theta_0 - \theta_0 \cot\theta_0\right]^{-1}, \tag{4.3}$$

where R_0 is defined in figure 4.9a. Expressing this in terms of the rivulet width, $w = 2R_0 \sin\theta$, gives the result shown in figure 4.9b, indeed showing the dependence on the contact angle θ_0. As expected, we recover the stability boundary for a complete cylinder at $\theta_0 = \pi/2$, for which $k_c w = 2k_c R_0 = 2$. For an equilibrium contact angle

$\theta_0 = 45^\circ$, as is the approximately case in our experiments, the critical wavenumber is slightly larger, namely $k_c w = 2.37$.

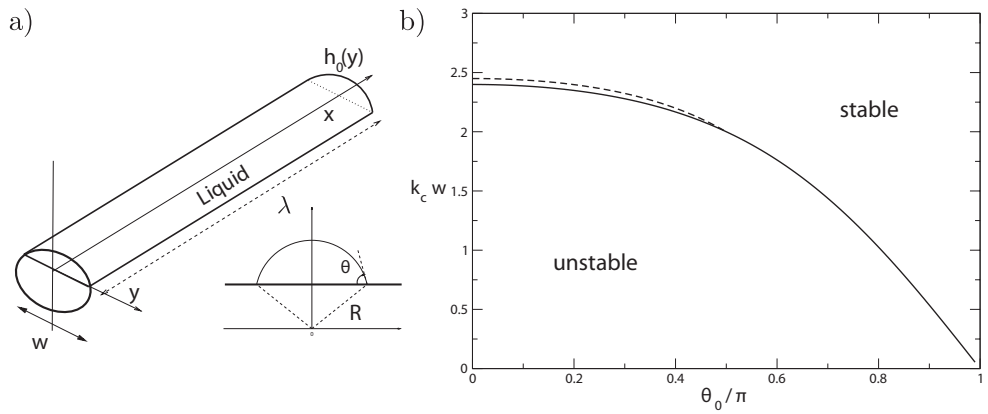

Figure 4.9: a) Simple view of a rivulet, modelled as a cylindrical cap on a substrate. b) Stability criterion of a cylindrical cap (from [Diez]). The solid line represents the theory by Davis [21].] and the dashed line the prediction by Diez et al. [24] (eq. 4.3).

Of course, the stability boundary does not yet give a prediction for the wavelength that will be observed experimentally. The dynamics of the instability is usually dominated by the fastest growing wavenumber k_{max}, which can be determined from the dispersion relation. This requires a detailed description of the flow inside the rivulet as well as the contact line dynamics. This stability analysis has been performed by [24] who numerically determined the dispersion relation for various contact angles and microscopic parameters for the contact line motion. In all cases, the maximum growth rate was typically attained for wavenumbers in between $0.5k_c$ and k_c. For simplicity, we use the rough estimate $k_{max} \approx 0.7k_c$, which for $\theta = 45^\circ$ gives a prediction $k_{max}w = 2\pi w/\lambda \approx 1.7$.

In order to compare the wavelengths observed in our experiments to the Rayleigh-Plateau instability of a rivulet, we determined the dimensionless wavenumber of drop emission, $2\pi w/\lambda$, at different velocities. The result is shown in 4.10a. Indeed, we observe that the wavenumbers are well below the stability boundary $2\pi w/\lambda_c = 2.37$. However, the wavenumbers are clearly much smaller than the prediction from the dispersion relation, which we estimated above as $2\pi w/\lambda \approx 1.7$. Hence, the separation distance between the emitted droplets is much larger than most unstable wavelength of an infinitely extended rivulet. This suggests that the drop emission is not governed directly by the Rayleigh-Plateau instability, valid for infinitely extended rivulets, but has a more subtle breakup dynamics.

Still, our data show that the rivulet width is the determining factor for the size of the emitted drops. To illustrate this, we collapsed all measurements by allowing a (constant) multiplicative factor between the three length scales. Figure 4.10b shows that the relations $w = 0.07\lambda$ and $w = 0.5R$ provide an accurate description of the data, showing a collapse for all velocities.

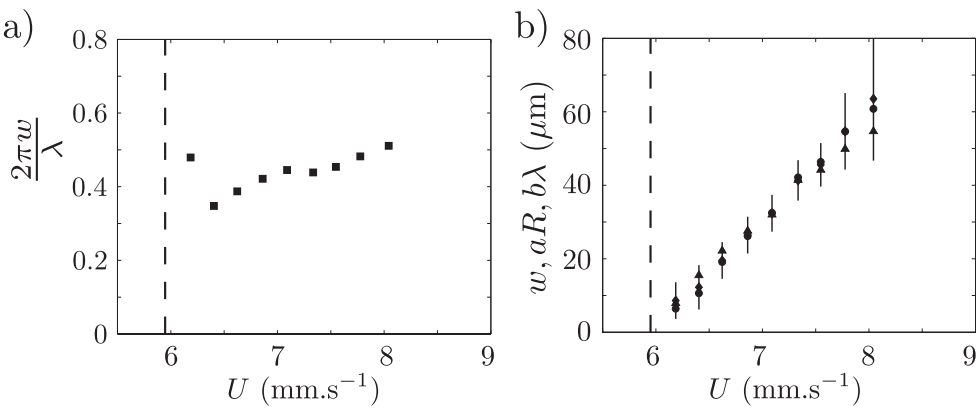

Figure 4.10: (a) Dimensionless wavenumber of drop emission, $2\pi w/\lambda$. The wavenumber lies well within the stability boundary of Rayleigh-Plateau instability for rivulets (~ 2.37), but is much smaller than the expected fastest growing mode (≈ 1.7). (b) All experimental data for w, R, and λ can be collapsed using a constant multiplicative factor $w = b\lambda$ ($\triangle$), with $b \approx 0.07$; $w = aR$ ($\circ$), with $a \approx 0.51$; w ($\diamond$).

4.4 Discussion

In this Chapter we studied droplet emission by cornered contact lines close to the critical velocity of instability. Our experimental results show that the tail width of the main drop, as well as the radius and wavelength of the emitted drops depend continuously on the substrate velocity U. All length scales tend to zero at the onset of droplet formation, e.g. upon reducing the contact line velocity to U_{cr}. This is in close agreement with earlier predictions [17]. The simple picture that emerges is that above the critical speed, the conical receding contact line transforms into a cone-shape that is connected to a rivulet. The geometry of the interface is completely dictated by the drop motion and receding contact line dynamics. Once a rivulet has formed, it breaks up into smaller droplets. The size and rate at which these drops are emitted are determined by the rivulet width w.

An open question, however, is to establish the precise dynamical mechanism (as

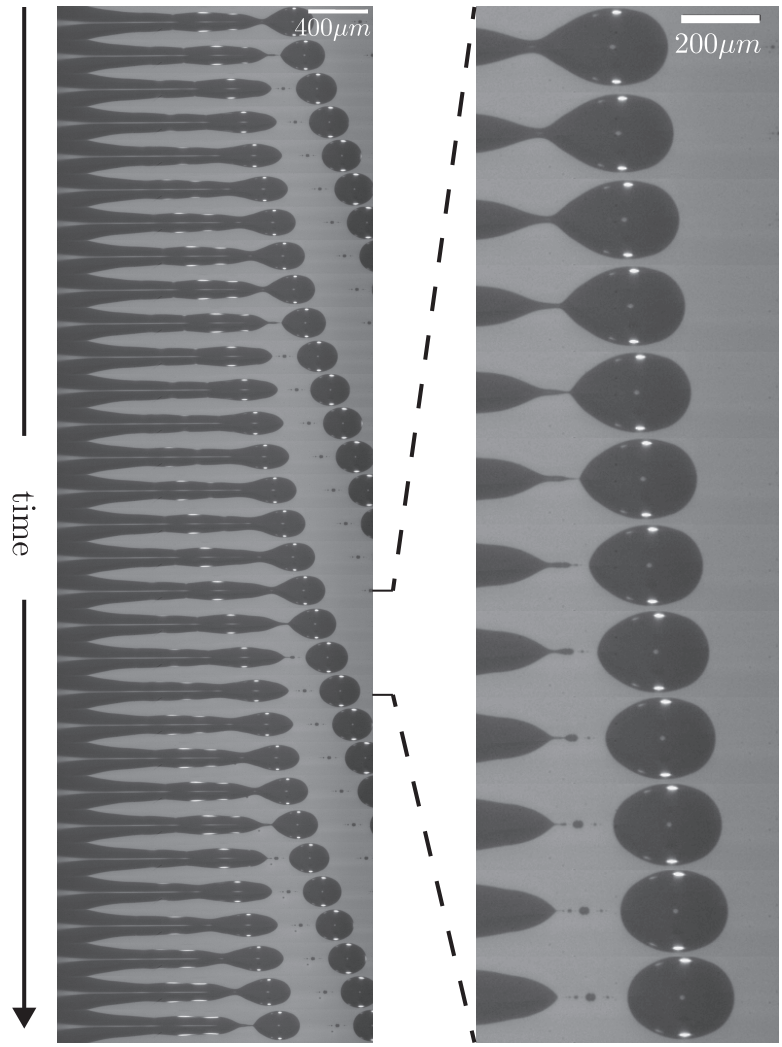

Figure 4.11: Time sequence of the droplet pinch-off. Used liquid: 20 cP, silicon oil. Plate velocity, $U_{plate} = 8.1$ mm/s. Time step between consecutive frames: 10 ms and 2 ms in the left and right image column respectively.

shown in figure 4.11) that selects the size of the drops. We found that the observed separation distance between drops is much larger than predicted for the instability of rivulets, which is the analogue for the Rayleigh-Plateau breakup of cylindrical jets. By mass conservation, this also means that the drop sizes are larger than expected from the Rayleigh-Plateau analogy. A similar conclusion was drawn by Diez

et al.[24], who found for finite-sized rivulets that the break-up starts at the edge of the rivulet. In figure 4.12 we explicitly highlight some differences between the rivulets

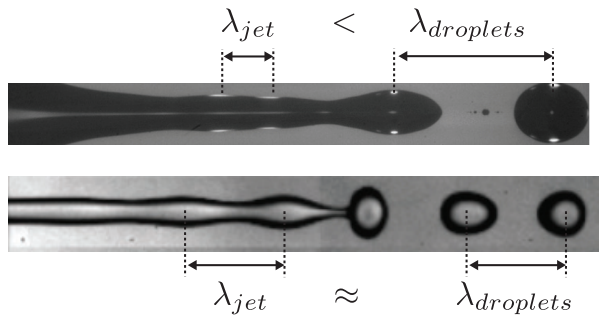

Figure 4.12: Comparison between an inviscid free jet break up and the rivulet break up discussed in this chapter (bottom image adapted from van Hoeve et al.[3]).

emitted by a cornered contact line (top panel), with respect to a pure Rayleigh-Plateau break-up as observed for cylindrical jets (bottom panel). In the latter case, one observes a gradual growth of a sinusoidal perturbation of well-defined wavelength. By the time the amplitude of the perturbation becomes comparable to the jet radius, this leads to the pinching of a droplet. The spacing between two successive droplets is almost identical to the wavelength observed on the jet. The situation is rather different for the rivulet shown in the upper panel. Due to the transition region from "cone" to "rivulet" on the left, we do not have a well-defined cylindrical shape as for the free jet. Although we can more or less identify a periodic ondulation on the rivulet, it is much harder to distinguish a gradual growth of the instability that could lead to pinchoff. Interestingly, we see that the wavelength on the rivulet (λ_{riv}) seems much smaller than the spacing between two deposited drops (λ). This is consistent with our conclusion from figure 4.10, which showed that the wavenumber based on the drop separation is much smaller than expected from Rayleigh-Plateau. These obervations suggest that the break-up is not determined by the Rayleigh-Plateau instability, but that the contact line dynamics at the tip of the rivulet plays an important role in the final pinching of the droplets. This also explains the ellipsoidal shape of the emitted droplets, which are slightly extended in the direction of the rivulet. Due to contact angle hysteresis, the receding tip leads to a smaller contact angle than the advancing contact line motion that occurs during pinchoff in the direction perpendicular to the rivulet.

References

[1] J. Eggers and E. Villermaux, "Physics of liquid jets", Rep. Progr. Phys. **71**, 036601 (2008).

[2] J. Eggers, "Nonlinear dynamics and breakup of free-surface flows", Rev. Mod. Phys. **69**, 865–929 (1997).

[3] W. van Hoeve, S. Gekle, J. H. Snoeijer, M. Versluis, M. P. Brenner, and D. Lohse, "Breakup of diminutive rayleigh jets", Physics of Fluids **22**, 122003 (2010).

[4] A. H. Lefebvre, *Atomization and sprays* (Hemisphere.) (1989).

[5] A. J. Yule and J. J. Dunkley, *Atomization of melts* (Clarendon Press, Oxford) (1994).

[6] E. Villermaux, "Fragmentation", Annual Review of Fluid Mechanics **39**, 419–446 (2007).

[7] H. Wijshoff, "The dynamics of the piezo inkjet printhead operation", Physics Reports **491**, 77–177 (2010).

[8] H. González and F. J. García, "The measurement of growth rates in capillary jets", Journal of Fluid Mechanics **619**, 179–212 (2009).

[9] T. Podgorski, J. M. Flesselles, and L. Limat, "Corners, cusps, and pearls in running drops", Phys. Rev. Lett. **87**, 036102(1)–(4) (2001).

[10] N. Le Grand, A. Daerr, and L. Limat, "Shape and motion of drops sliding down an inclined plane", J. Fluid Mech. **541**, 293–315 (2005).

[11] T. D. Blake and K. J. Ruschak, "A maximum speed of wetting.", Nature **282**, 489–491 (1979).

[12] H. Benkreira and M. I. Khan, "Air entrainment in dip coating under reduced air pressures", Chem. Eng. Sci. **63**, 448–459 (2008).

[13] H. Benkreira and J. B. Ikin, "Dynamic wetting and gas viscosity effects", Chem. Eng. Sci. **65**, 1790–1796 (2010).

[14] R. Ledesma-Aguilar, R. Nistal, A. Hern*á*ndez-Machado, and I. Pagonabarraga, "Controlled drop emission by wetting properties in driven liquid filaments", Nature Materials **10**, 367–371 (2011).

[15] I. R. Peters, J. H. Snoeijer, A. Daerr, and L. Limat, "Coexistence of Two Singularities in Dewetting Flows: Regularizing the Corner Tip", Phys. Rev. Lett. **103** (2009).

[16] M. Ben Amar, L. J. Cummings, and Y. Pomeau, "Transition of a moving contact line from smooth to angular", Phys. Fluids **15**, 2949–2960 (2003).

[17] J. Snoeijer, N. Le Grand, L. Limat, H. A. Stone, and J. Eggers, "Cornered drop and rivulets", Phys. Fluids **19**, 042104 (2007).

[18] H. A. Stone, L. Limat, S. K. Wilson, J. M. Flesselles, and T. Podgorski, "Corner singularity of a contact line moving on a solid substrate", C. R. Physique **3**, 103–110 (2002).

[19] L. Limat and H. A. Stone, "Three-dimensional lubrication model of a contact line corner singularity", Europhys. Lett. **65**, 365 (2004).

[20] J. H. Snoeijer, E. Rio, N. Le Grand, and L. Limat, "Self-similar flow and contact line geometry at the rear of cornered drops", Phys. Fluids **17**, 072101 (2005).

[21] S. H. Davis, "Moving contact lines and rivulet instabilities. part 1. the static rivulet", Journal of Fluid Mechanics **98**, 225–242 (1980).

[22] D. Langbein, "The shape and stability of liquid menisci at solid edges", Journal of Fluid Mechanics **213**, 251–265 (1990).

[23] R. V. Roy and L. W. Schwartz, "On the stability of liquid ridges", Journal of Fluid Mechanics **391**, 293–318 (1999).

[24] J. A. Diez, A. G. González, and L. Kondic, "On the breakup of fluid rivulets", Physics of Fluids **21**, 082105 (2009).

[25] J. Park, K. Y. Suh, S. Seo, and H. H. Lee, "Anisotropic rupture of polymer strips driven by rayleigh instability", The Journal of Chemical Physics **124**, 214710 (2006).

[26] A. G. González, J. Diez, R. Gratton, and J. Gomba, "Rupture of a fluid strip under partial wetting conditions", EPL (Europhysics Letters) **77**, 44001 (2007).

[27] J. A. Diez, A. G. González, and L. Kondic, "Stability of a finite-length rivulet under partial wetting conditions", Journal of Physics: Conference Series **166**, 012009 (2009).

[28] J. D. Fowlkes, L. Kondic, J. Diez, Y. Wu, and P. D. Rack, "Self-assembly versus directed assembly of nanoparticles via pulsed laser induced dewetting of patterned metal films", Nano Letters **11**, 2478–2485 (2011).

[29] A. Marchand, "Mouillage statique et dynamique : Influences géométriques aux échelles moléculaires", Ph.D. thesis, Université Paris VII (2011).

[30] W. T. Pimbley and H. C. Lee, "Satellite droplet formation in a liquid jet", IBM Journal of Research and Development **21**, 21 – 30 (1977).

[31] L. Rayleigh, "On the instability of jets", Proc. Roy. Soc. London **10**, 4 (1879).

[32] J. A. F. Plateau, *Statique expérimentale et theorique des liquides soumis aux seules forces moléculaires*, volume 2 (Gauthier Villars: Paris) (1873).

[33] P.-G. de Gennes, F. Brochart-Wyart, and D. Quéré, *Capillarity and Wetting Phenomena: Drops, Bubbles, Pearls, Waves* (Springer) (2003).

5

Bubble formation during the collision of a sessile drop with a meniscus [*] [†]

The impact of a sessile droplet with a moving meniscus, as encountered for example in dip-coating, generically leads to the entrapment of small air bubbles. Here we experimentally study this process of bubble formation by looking through the liquid using high-speed imaging. Our central finding is that the size of the entrapped bubble crucially depends on the location where coalescence between the drop and the moving meniscus is initiated: (i) at a finite height above the substrate, or (ii) exactly at the contact line. In the first case, we typically find bubble sizes of the order of a few microns, independent of the size and speed of the impacting drop. By contrast, the bubbles that are formed when coalescence starts at the contact line become increasingly large, as the size or the velocity of the impacting drop is increased. We show how these observations can be explained from a balance between the lubrication pressure in the air layer and the capillary pressure of the drop.

[*]Submitted as: D.L. Keij, K.G. Winkels, H. Castelijns, M. Riepen and J.H. Snoeijer, *Bubble formation during the collision of a sessile drop with a meniscus*.

[†]The scaling arguments put forward in this thesis are also part of: W. Bouwhuis, R. C.A. van der Veen, T. Tran, D.L. Keij, K.G. Winkels, I.R. Peters, D. van der Meer, C. Sun, J. H. Snoeijer, and D. Lohse, "Maximal air bubble entrainment at liquid drop impact", *Phys. Rev. Lett.*, **109**, 264501 (2012).

5.1 Introduction

Air bubbles can be entrapped in a wide variety of flows with a free surface [1–16]. Such entrapped bubbles can have large effects on for example bulk gas concentrations and sound emission [17, 18]. In addition, bubbles can be a nuisance for industrial processes, where they cause defects, obstructions or noise [19]. Various different mechanisms for air entrapment have been proposed in the literature. For example, it is well known that the impact of a drop on a free surface (e.g. rain) can induce an inertial cavity collapse that results in an oscillating bubble [2, 8]. At lower impact speeds, air films can be trapped between a liquid drop and a liquid or a solid wall, by lubricating effects of the medium. Such a lubricating film can delay or completely avoid coalescence. In the extreme case such an air film can even cause a droplet to float on the liquid surface [20–22]. However, depending on whether this film simply drains or becomes unstable, air entrainment might occur [6, 9, 10, 23]. However, it has been predicted that bubbles can also be entrapped during a coalescence with zero impact velocity, for which no lubricating film develops. In this case the bubbles form by reconnecting capillary waves that result in toroidal bubble rings as described theoretically [24].

In this chapter we focus on entrapment of air bubbles that form when a sessile drop impacts with a moving meniscus. This is relevant for applications as dip-coating and immersion lithography (Fig. 5.1). Dip-coating is a very common setup both for applications and fundamental studies, where a solid plate is plunged into or withdrawn from a liquid reservoir. A very similar geometry is present in immersion lithography, a technology used in semi-conductor industry: replacing the air in between a lens and the silicon wafer by a liquid leads to an increase in the numerical aperture of the system, allowing for projecting smaller structures. A simplified version of the flow geometry for immersion lithography is sketched in figure 5.1 c-d). The “meniscus” consists of a liquid bridge held between the hydrophilic glass plate and a wafer which is usually made partially wetting by a coating. The water will preferably remain in the gap, due to the contact with the hydrophilic glass plate, even when the substrate is in motion. A first mechanism for bubble entrapment is that at high velocities, the contact line can become unstable resulting in entrainment of a thin air film [25] or bubbles [26, 27]. A second mechanism that leads to bubbles in these applications is due to residual drops, which are left on the substrate. These drops move along with the substrate and collide with the reservoir (dip-coating) or liquid bridge (immersion lithography). Air bubbles are generically entrapped during a collision of such a sessile drop with the meniscus.

We present an experimental study on the formation of bubbles resulting from the impact of a sessile drop with a meniscus close to a moving contact line. The sessile

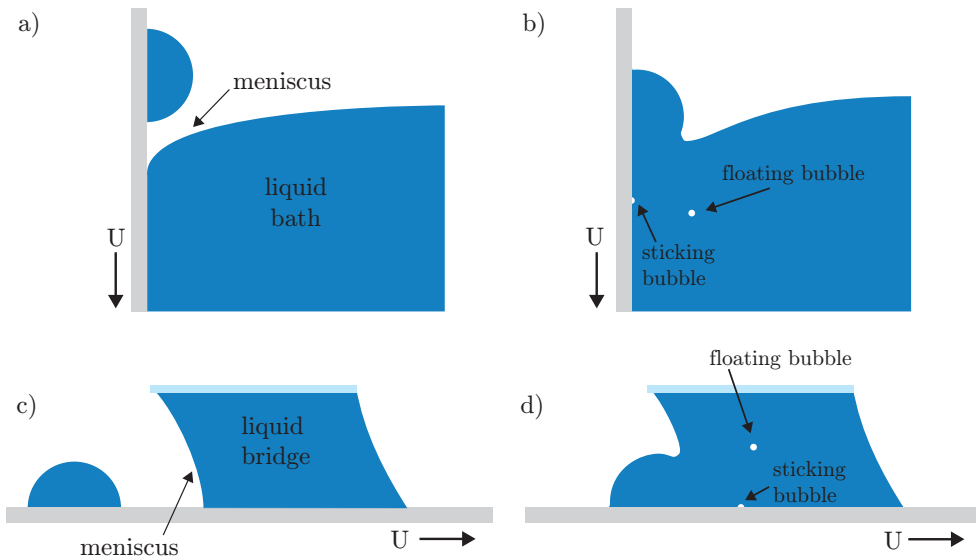

Figure 5.1: Two examples of bubble entrapment during the collision of a sessile drop with a meniscus: dip-coating (a,b) and immersion lithography (c,d). (a) A sessile drop moves with the substrate into a liquid reservoir. (b) Air bubbles can be trapped during the coalescence of the drop with the reservoir. These bubbles are sometimes floating in the bulk liquid (floating bubbles) and sometimes attached to the substrate (sticking bubbles). (c) A sessile drop moves with the substrate into a liquid bridge. The liquid bridge consists of a gap filled with liquid, stationary at the top (pinned contact line) and sliding over the substrate at the bottom (moving contact line). The front part of the liquid bridge forms the meniscus in the 'drop-meniscus-collision'. (d) Similar as in dip-coating, two types of bubbles can be formed.

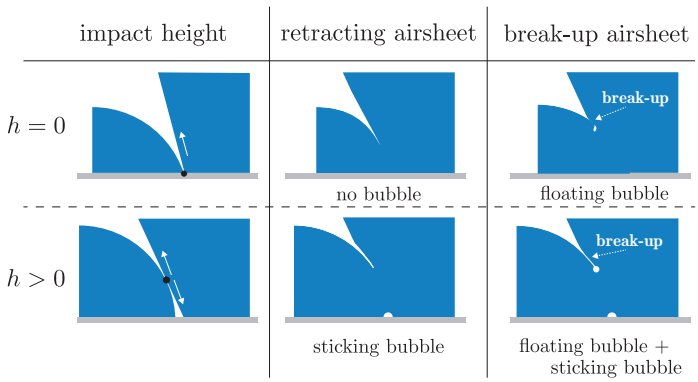

Figure 5.2: Scenarios for bubble entrapment. Two different bubble types can form depending on the impact height h (indicated by the black dot). If the first contact is located at the contact line ($h = 0$), the upward motion of the coalescing bridge drives the air between the drop and the meniscus away from the substrate. Depending on the dynamics of this retraction, this results into breakup (floating bubble) or no bubble. Similar dynamics is observed when first contact is above the contact line $h > 0$. However, for the downward motion of the liquid bridge we always observe the entrapment of an air bubble at the substrate (sticking bubble).

drop always coalesces with the meniscus. As summarized in Fig. 5.2, however, we identified two scenarios for bubble entrapment. First, when the contact takes place at or very close to the moving contact line (i.e. at $h = 0$, with h the impact height with respect to the moving substrate) we observe "floating bubbles". These bubbles are spherical and float in the bulk of the liquid bridge. Second, when the first contact between the sessile drop and the meniscus takes place above the moving contact line ($h > 0$) also a "sticking bubble" can be formed. This bubble is attached to the substrate and moves with the wafer. It should be noted that apart from these two cases, the coalescence can also result into no bubble formation, or a combination of floating bubbles and sticking bubbles. As summarized in Fig. 5.2, this depends on whether or not the airsheet breaks up during the coalescence.

The chapter is organized as follows. We first introduce the experimental setup (Sec. 5.2). Then we will discuss the formation mechanism of the two possible types of bubbles appearing during the drop-meniscus collision (Sec 5.3), and quantify the size of the entrapped bubbles, as a function of the impact velocity and the size of the sessile drop (Sec. 5.4). The latter section also includes explanations for the size of the two types of bubbles. The chapter ends with a discussion (section 5.5).

5.2 Experimental setup

The experimental setup consists of a coated glass wafer ($D = 300$ mm) clamped to a turntable that is rotated with controlled angular velocity $\omega = 5 - 225\ ^\circ/s$. The rotational motion of the wafer approximates a linear motion in the camera reference frame, due to the small droplet size compared to the radial position on the wafer ($r \sim 135$ mm). A detailed description of a similar setup is given in Winkels et al. [28]. The geometry in which the collision between a sessile drop and a meniscus is realized is sketched in Fig. 5.3. A small glass plate (7×12 mm) is fixed in the camera reference frame at a height $0.8 - 2.8$ mm above the substrate and close (< 15 mm) to the edge of the wafer. The gap between the wafer and the glass plate is filled with water (Millipore, Milli-Q, Advantage A10) resulting in a liquid bridge with a pinned contact line at the hydrophilic glass plate and a mobile contact line at the coated wafer ($\theta_e \sim 70^\circ - 83^\circ$). With this construction, the liquid is held fixed in the camera reference frame also when the wafer is rotated. The liquid bridge then slides over the wafer, such that at the front and at the rear of the bridge there is a moving contact line. Within the experimental range of velocities, we observe no air entrainment unless there is a collision with an incoming sessile drop.

The two main control parameters in the experiment are the size and velocity of the impacting drop. Before each measurement a sessile droplet is created on the wafer with multiple drops from a micro-drop generator (Microdrop Technologies, MD-E-3000 in combination with a MD-K-130 dispenser head, single drop diameter ~ 65 μm). We achieve drop sizes in the range $R \sim 0.2 - 1$ mm. The sizes are determined from side view recordings. The wafer velocity, and hence the impact velocity of the sessile drop, is varied over the range $U \sim 0.01 - 0.54$ m/s.

The process of impact and the subsequent bubble formation is recorded simultaneously with two high speed cameras. For the top view a Shimadzu HPV1 or Photron SA1.1 (framerates $10 - 250$ kfps) is used, connected to a long distance microscope (Navitar 12X Zoom with 1.5X front lens) obtaining a maximum resolving power of 2 μm/pixel. The side view is captured simultaneously with a PCO1200s camera (used at 1 kfps) attached to a lens (Jenoptik, JENmetar 1x/12 LD). To image the formation of the bubbles, the meniscus is viewed from above through the top glass plate, as shown in Fig. 5.3a. In combination with backlit illumination the meniscus turns black, while the wetted area inside the liquid bridge turns bright. Typical image recordings are shown in Fig. 5.3b. The contact line of the sessile drop is marked with the yellow line: prior to impact, the drop is 'hidden' behind the meniscus in the top view recordings. During the coalescence, the region where the drop and meniscus have merged will actually turn bright and can thus be monitored very accurately.

Finally, we note that the liquid bridge can exhibit a rather complex geometry.

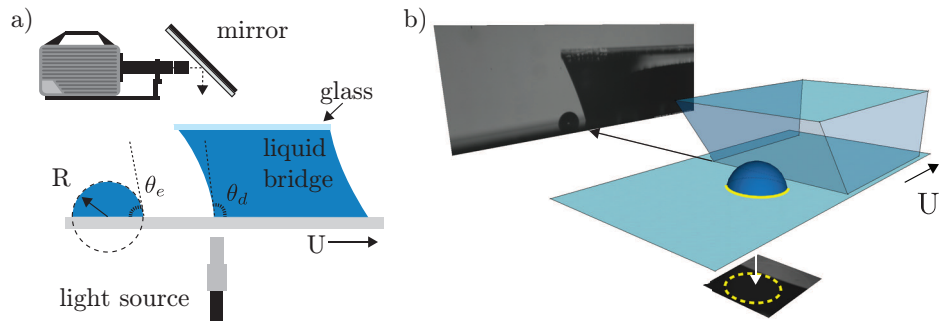

Figure 5.3: (a) Schematic of the experimental setup. The top-view recordings are obtained with backlit illumination. The drop radius R, equilibrium contact angle θ_e and dynamic contact angle θ_d are also defined. (b) Three-dimensional impression of the impact of a sessile droplet (yellow line denotes the contact line) with the liquid bridge. The black-and-white images show typical recordings of the side- and top-view obtained with the experimental setup.

The meniscus can be convex or concave depending on the gap height, volume of liquid and the dynamic contact angle. Throughout our experiments we have tuned these parameters in order to keep the impacting meniscus as "flat" as possible in the side view. By avoiding strongly concave or convex menisci, we have been able to obtain conditions where the bubble formation is highly reproducible. The geometry of impact is relatively simple in this case: the sessile drop is a spherical cap with angle θ_e, while the meniscus is approximated by a "plane" with dynamic contact angle θ_d. The height of impact then follows from elementary geometry and can be realized at $h = 0$ or at $h > 0$.

5.3 Experimental observations

5.3.1 Floating bubbles: $h = 0$

We first consider the case where the coalescence is initiated at the contact line, with impact height $h = 0$ within experimental accuracy. The subsequent coalescence is directed upwards, away from the substrate. The outcome of the experiment is that either a floating bubble is formed inside the liquid, or no bubble is formed. Figure 5.4 shows a typical image sequence in the case a floating bubble is entrapped. Below the experimental stills we provide sketches of the side view, to clarify the various stages of the bubble formation.

A sessile droplet with size R, moves from left to right with velocity U (Fig.5.4I). The yellow solid line indicates the contact line of the sessile drop which is hidden behind the black meniscus prior to impact. The white dashed line denotes the moving contact line of the meniscus. Interestingly, a small deformation of the contact line can be observed at time $t = -24\ \mu s$ before impact (white arrow, Fig. 5.4, $t = -24\ \mu s$). This deformation is due to the lubrication pressure building up in the air between the drop and the meniscus. Subsequently, the coalescence process starts at, or at least very close to, the contact line (Fig. 5.4II). During the upward motion of the coalescing bridge a pocket of air is enclosed, resulting into a floating bubble (Fig. 5.4III). The coalescence continues while the spherical bubble floats inside the liquid bridge ($t = 312\ \mu s$, Fig.5.4). The floating bubble is stable and remains inside the liquid bridge also after drop collision (Fig. 5.4IV).

5.3.2 Sticking bubbles: $h > 0$

Another type of bubbles that can be entrapped is a sticking bubble, attached to the substrate after its formation. These sticking bubbles form a spherical cap with a finite contact angle, and arise when the initial contact between the drop and the substrate occurs at a finite height above the substrate, $h > 0$. The process of sticking bubble formation is clearly revealed in the top view recordings as shown in Figure 5.5. Once more, we complement the still images with side view sketches to clarify the process of bubble formation (I-IV). It should be noted that in comparison with Fig. 5.4, besides the impact height $h > 0$ also the drop size R is different. However as will be shown later this does not affect the phenomenon.

At very short time before impact ($t = -2\ \mu$s, Fig. 5.5I), the drop-meniscus separation distance is very small and the sessile drop is indicated by the yellow circle. Once again, the meniscus is completely black and the drop moves in from the left with velocity U, hidden behind the meniscus in this top view. The moving contact line of the meniscus is slightly curved and indicated by the white dashed line. After several microseconds, $t = 22\ \mu s$, one clearly observes that contact has occurred at a finite height above the substrate. The bridge connecting the drop and the meniscus appears as a bright ellipsoidal area (Fig. 5.5II). Coalescence is initiated in all directions, and the downward part of the bridge approaches the substrate (Fig. 5.5, $t = 22 - 94\ \mu s$). During this rapid motion, the air is confined in a cylindrical cap that is squeezed between the wafer and the downward coalescing front. At the final stage of bubble formation, this cylindrical shape pinches off symmetrically along the wafer (up- and downwards in the image), leaving a small "satellite" bubble at the substrate. This sticking bubble (Fig. 5.5III, $t = 190\ \mu s$, red dashed circle), moves with the substrate. The coalescence also proceeds in the upward direction, away from the contact

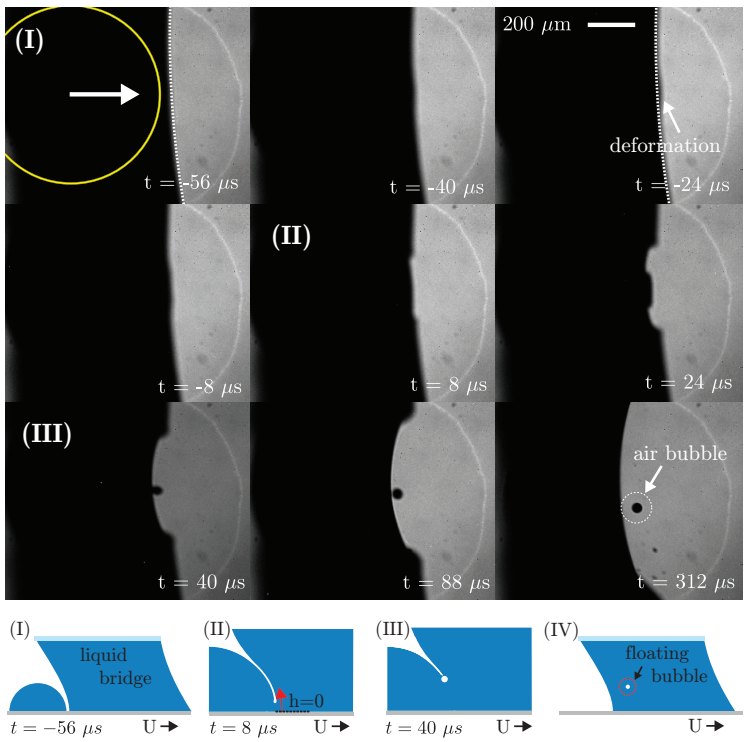

Figure 5.4: Top: High-speed recordings of the formation of a floating bubble. The yellow solid line denotes the contact line of the sessile droplet before impact (hidden behind the black meniscus). In the final top view image ($t = 312\mu$s), the air bubble is located in the white dashed circle. Parameter settings: $U = 300 \pm 3$ mm/s, $R = 0.35 \pm 0.02$ mm, $R_{bub} = 22 \pm 3$ μm. Bottom: Sketch of the side view during the bubble formation at different moments in time. I) The sessile drop approaches the meniscus at velocity U. II) Before coalescence an air sheet is formed between the meniscus and the drop, which retracts upwards away from the substrate if coalescence is initiated at the contact line ($h = 0$). III) The retracting air sheet is enclosed during the coalescence. IV) A spherical bubble is formed, that floats in the bulk liquid (floating bubble).

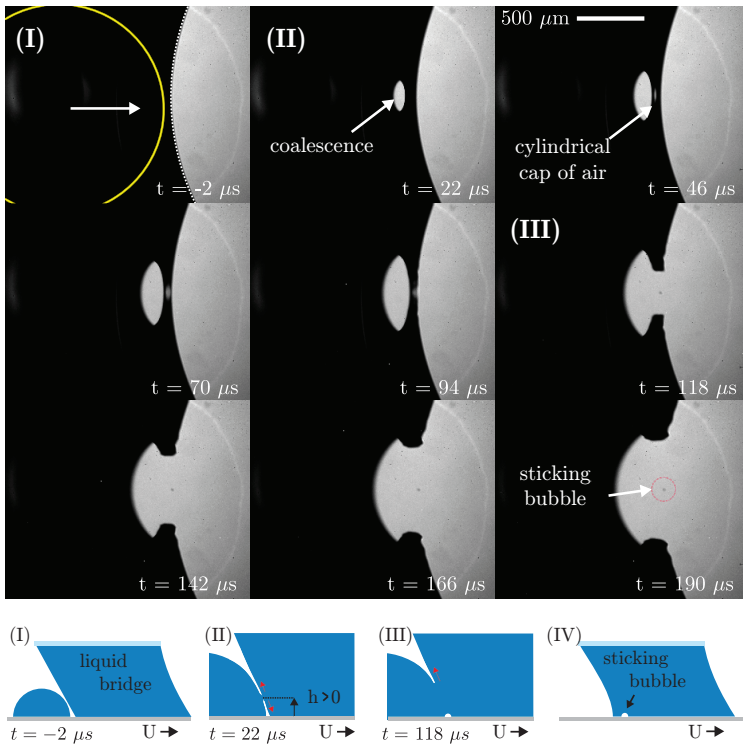

Figure 5.5: Top: High-speed recordings of the formation of a sticking bubble. The yellow solid line in the first image denotes the static contact line of the sessile droplet (hidden behind the meniscus), while the dashed line shows the moving contact line of the meniscus. In the final image ($t = 190\mu$), the air bubble is indicated by the red dashed circle. Parameter settings: $U = 375 \pm 3$ mm/s, $R = 1.00 \pm 0.03$ mm, $R_{bubble} = 12 \pm 6$ μm. Bottom: Sketch of the side view during the bubble formation. I) The sessile drop approaches the meniscus. II) First contact occurs at finite height $h > 0$. As a result, a coalescing bridge moves upwards and downwards. III) The downward retracting air sheet creates an air channel at the substrate (perpendicular to the field of view), which finally breaks up into a sticking bubble. IV) The sessile drop merged with the liquid bridge, leaving a sticking bubble inside the bulk liquid.

line. In some experiments we have seen that this can also result into a floating bubble, in analogy to those described in Sec. 5.3.1.

5.4 Bubble sizes

5.4.1 Measurements

We now investigate the size of the entrapped bubbles, characterized by the radius R_{bub}, for different impact conditions. In particular, we vary the size of the sessile drop, R, and the impact velocity, U. Our measurements are summarized in Fig. 5.6. The coloured triangles (◁,◁,◁) show data obtained for floating bubbles, for $U = 0.01$ - 0.4 m/s and $R = 0.26$-1.00 mm in radius. The blue squares (□) are results for sticking bubbles, for the impact velocities $U = 0.02 - 0.54$ m/s and $R = 0.21 - 0.62$ mm. Each data point corresponds to a single collision, and the error bars represent the accuracy of resolution. One clearly observes that the two different types of bubbles display

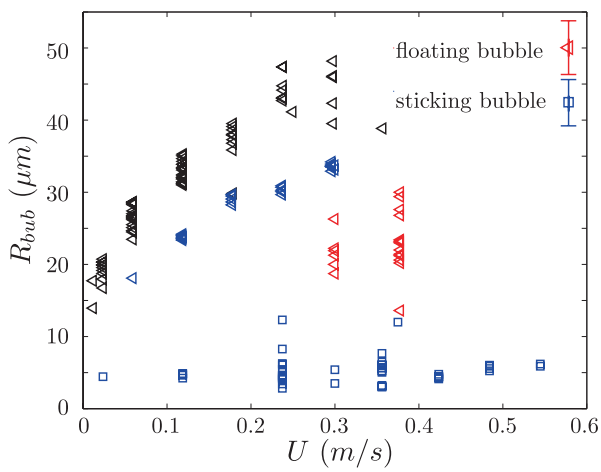

Figure 5.6: Size of entrapped bubbles R_{bub}, measured as a function of impact velocity U. The data summarize all collision events, for varying drop sizes. The triangles (◁) represent the data for floating bubbles. For these bubbles the colors indicate the approximate impact drop radius: in red ◁ $R < 400$ μm, in blue ◁ $400 < R < 600$ μm and in black ◁ $R > 600$ μm. The squares (□) denote the sticking bubbles for $0.21 < R < 0.62$. The typical measurement error is indicated in the legend.

very different sizes, originating from the different mechanisms of their formation. For floating bubbles, the general trend is that R_{bub} increases with impact velocity. However, for a given velocity there is a rather large spread of the data. We show

below that this can be attributed to the different sizes of impacting drops. This is also why R_{bub} is lower for the largest impact velocities, which were obtained for relatively small drops. The results for sticking bubbles are very different: within our experimental resolution, the bubble size is independent of both the impact velocity and of the radius of impacting drop. The size of sticking bubbles is approximately $R_{bub} \sim 5\ \mu$m, which is much smaller than the floating bubbles.

5.4.2 Floating bubbles: $h = 0$

As observed in Sec. 5.3.1, the meniscus is weakly distorted already before the coalescence starts (arrow Fig. 5.4, $t = -24\ \mu s$). This suggests that a pressure builds up inside the air layer in between the drop and meniscus, which is sufficiently strong to deform the liquid interfaces prior to impact. In fact, this effect is well-known for drop impact on a solid or on a liquid reservoir [12, 16, 20–22, 29, 30]. As the air is squeezed out of the narrow gap, the viscous air flow leads to a lubrication pressure inside the layer.

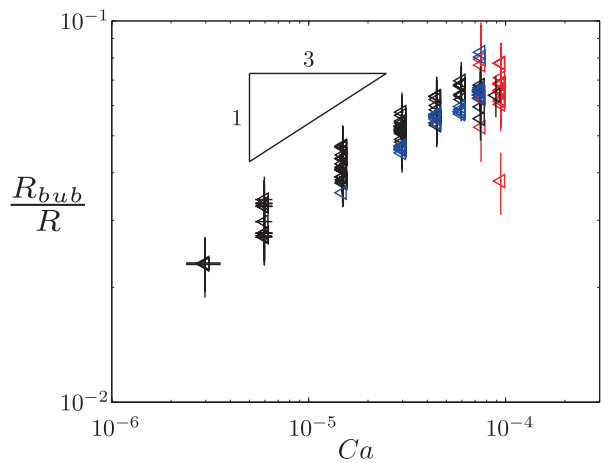

Figure 5.7: Floating bubbles sizes. Bubble radius R_{bub} normalized by R, plotted versus the capillary number $\mathrm{Ca} = U\eta_g/\gamma$. The colors indicate the approximate impact drop radius: in red $R < 400\ \mu m$, in blue $400 < R < 600\ \mu m$ and in black $R > 600\ \mu m$.

The volume of the entrapped air sheet ultimately determines the size of the air bubble. We therefore propose that the lubrication pressure is responsible for the velocity dependence of R_{bub}. As the pressure originates from the dynamical viscosity of the gas, η_g, it is natural to re-plot the experimental data in terms of the capillary

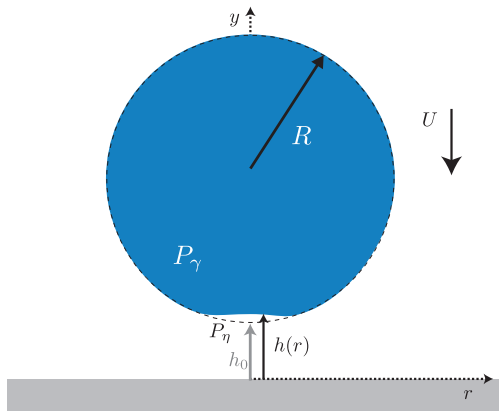

Figure 5.8: Sketch of a drop impacting a substrate.

number $\mathrm{Ca} = U\eta_g/\gamma$, where γ is the surface tension (even though we did not explicitly vary the gas viscosity η_g and surface tension γ). Figure 5.7 shows the data in dimensionless form, where we scaled the bubble radius by the radius of the impacting drop. In comparison to Fig. 5.6, we indeed observe that the rescaled bubble sizes are nicely aligned, and display a monotonic increase with Ca. The scatter is comparable to the experimental error in determining the bubble radius. The data are reasonably described by a power-law over more than a decade in Ca.

We now rationalize this dependence on Ca by drawing the analogy with drop impact on a solid substrate [12, 13, 31]. The geometry of this impact is sketched in Fig. 5.8, and is actually much simpler than the geometry of Fig. 5.1. While the drop approaches the substrate with velocity U, the thickness of the air layer reduces and air is squeezed out. As long as the lubrication pressure, P_η, is significantly smaller than the capillary pressure inside the drop, $P_\gamma = 2\gamma/R$, the drop remains spherical. In this regime the drop is undeformed and the shape of the air layer is described by $h(r) \simeq h_0 + r^2/(2R)$. Then, the lubrication pressure can be computed exactly [32].

$$P_\eta = \frac{3\eta_g U R}{{h_0}^2 \left(1 + \frac{r^2}{2Rh_0}\right)^2}, \tag{5.1}$$

where h_0 is the gap thickness at $r = 0$. From this equation, it is clear that the typical lateral length scale of the lubricating pressure is, $L \sim (Rh_0)^{1/2}$.

In the Appendix (section 5.6), we provide a perturbation expansion to compute the deformation induced by the lubrication pressure. Here we will provide a scaling argument. To estimate at what distance h_0 the drop will start to deform, we balance

$P_\eta \sim P_\gamma$. Note that this is different from [12, 13], in which P_η is balanced with the inertial pressure inside the liquid. The visco-capillary balance yields a characteristic height for the dimple below the drop H (Fig. 5.8):

$$\frac{3\eta_g UR}{H^2} \sim \frac{2\gamma}{R} \Longrightarrow H \sim R\,(\mathrm{Ca})^{1/2}. \tag{5.2}$$

This determines the distance at which the drop first deforms, and provides the natural length scale for the dimple size in the direction normal to the wall. In a very short time (~ 0.1 ms) the deformation finally leads to very fast coalescence during which the lubricating air sheet is trapped and forms a bubble. The volume of the air pocket, and hence of the bubble, is expected to scale as

$$R_{bub}^3 \sim HL^2 \sim H^2 R \Longrightarrow \frac{R_{bub}}{R} \sim \mathrm{Ca}^{1/3}. \tag{5.3}$$

As observed both in the data (Fig. 5.7) and the scaling, the bubble size increases with velocity.

For completeness, we also report the scaling in the inertial regime that is relevant at higher impact velocities. For higher impact velocities, inertia comes into play and can become significantly larger than capillary forces. Then the characteristic deformation height is determined from a balance of the lubrication pressure and the inertial pressure, $P_l \sim P_\gamma$. Where P_l is estimated from the unsteady Bernoulli equation (deceleration of the liquid). Scaling suggests that the liquid flow potential $\phi \sim UL$ changes over a time $t \sim \frac{H}{U}$, such that $P_l \sim \frac{\rho_l LU^2}{H}$. The characteristic height for deformation then becomes:

$$\frac{\eta_g UR}{H^2} \sim \frac{\rho_l LU^2}{H} \Longrightarrow H \sim R\mathrm{St}^{-2/3}, \tag{5.4}$$

where $\mathrm{St} = \frac{\rho_l RU}{\eta_g}$. As a result the bubble volume is expected to scale as

$$R_{bub}^3 \sim HL^2 \Longrightarrow \frac{R_{bub}^3}{R^3} \sim \mathrm{St}^{-4/3}, \tag{5.5}$$

i.e. decreasing bubble volume with velocity. Therefore it is expected that a maximum will occur in the crossover between both regimes when

$$\mathrm{St} \sim \mathrm{Ca}^{-3/4} \Longrightarrow U_{cross} \sim \frac{\eta_g^{1/7}\gamma^{3/7}}{\rho_l^{4/7} R^{4/7}}. \tag{5.6}$$

We were indeed able to verify these scaling arguments, including the appearance of a maximum bubble volume, for the drop impact of a liquid drop on a solid substrate as

sketched in Fig. 5.8. The resulting dimple heights and drop volumes were determined from numerical simulations and experiments based on interferometry, the details of which are reported in Bouwhuis et al [31]. The resulting dimple heights and bubble volumes are reported in Fig. 5.9. Indeed, both the dimple and volume display a maximum, and the data are consistent with the scaling laws of equation (5.2,5.3) and (5.4,5.5). Let us emphasize that for the collisions of drops with a meniscus, as

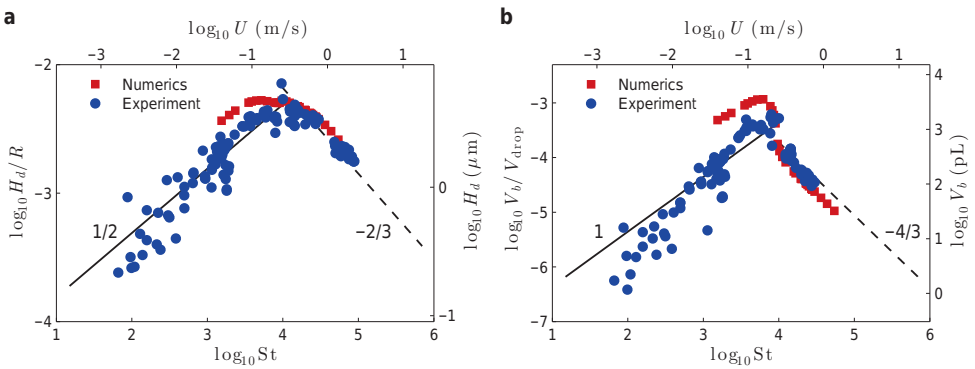

Figure 5.9: Maximum entrapment of air bubbles for drop impact on a solid surface [31]. (a) Dimple height H and (b) entrained bubble volume V_{bub} as functions of the impact velocity U (upper axes) and Stokes number St (lower axes). The shape of the air layer can be characterized by the dimple height H and the lateral extension L. Blue circles correspond to high-speed color interferometry measurements, red squares correspond to numerical simulations. The straight lines correspond to the derived scaling laws in the capillary regime (solid) and inertial regime (dashed) with the respective scaling exponents.

reported in Fig.5.7, we only explored the capillary regime. Despite the obvious difference in impact geometry, this scaling argument, $R_{bub} \sim R\mathrm{Ca}^{1/3}$ is also consistent with the experimental data for the floating bubbles that form during the impact of a sessile drop with a meniscus. This suggests that the bubble volume is indeed governed by the lubrication effect of the squeezed gas layer. Clearly, a much more detailed modelling of the impact geometry, and the subsequent drainage of air, is required to confirm this scenario.

5.4.3 Sticking bubbles: $h > 0$

How can we understand that the size of sticking bubbles is independent of U? The key is that the coalescence of the meniscus and drop in Fig. 5.5, leading to the air

confinement at the substrate, is much faster than the impact velocity U. This is quantified in Fig. 5.10, where we plot the growth of the coalescing bridge in time. The bridge radius w approximately grows as $w \sim t^{1/2}$ (best fit: 0.55), which is comparable to the standard inertia-dominated coalescence of two free droplets [24, 33]. The fact that the exponent is slightly larger than 1/2 is consistent with recent measurements on water drops, signalling a crossover to a viscosity-dominated coalescence [34]. A power-law with exponent smaller than unity implies a very rapid dynamics at the initial stages. From the perspective of bubble entrapment, this means that speed with which the cylindrical cap of air is squeezed (Fig. 5.5), is much faster than the actual impact velocity of the sessile drop. This explains why U is irrelevant for the size of the sticking bubbles.

It still remains a question why the size of sticking bubbles is also independent of the drop radius R. A closer look at the sticking bubble formation, reveals a striking analogy with the pinch-off process of a buoyant air bubble from a nozzle in water, such as visualized by Burton et al [35] (see figure 5.11b). In their case, the detachment of the large bubble occurs by the breakup of a slender cylindrical neck. During this breakup, small satellite bubbles of approximately 10 microns diameter are formed at the middle of the neck. According to [36], the size of these satellites can be attributed to the inertia in the gas phase, which becomes relevant during the final stages of pinch-off. Indeed, we observe a very similar breakup of the cylindrical cap in Fig. 5.11a. The main difference with respect to Burton et al. [35] is that in our case the cylinder of air is attached to the surface. However, the time scale for breakup and the size of the satellite bubble are almost the same in both experiments. Clearly, the size of the impacting drop is completely irrelevant during this final stage of the bubble formation.

In conclusion, the sticking bubbles display a universal size due to a combination of two classical singularities: coalescence and breakup. First, the growth of the coalescing bridge is extremely fast, making the impact velocity of the sessile drop irrelevant. It confines the air between the coalescing bridge and the substrate into a cylindrical air pocket. This cylinder of air undergoes a pinch-off, similar to [35–38]. What remains is a small bubble that is completely independent of impact conditions.

5.5 Discussion

We have identified two types of bubbles that form during the impact of a sessile drop with a meniscus. As summarized in Fig. 5.2, the formation crucially depends on the height of the initial contact. When the first contact occurs at $h = 0$ the resulting bubbles are “floating” inside the liquid. These bubbles appear due to the entrapment of a

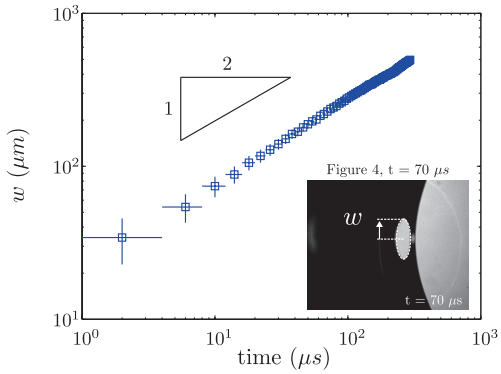

Figure 5.10: Coalescence bridge growth w as a function of time t, for impact occurring at finite height h. Inset: typical recording image (see Fig. 5.5, $t = 70\ \mu s$) with definition of w.

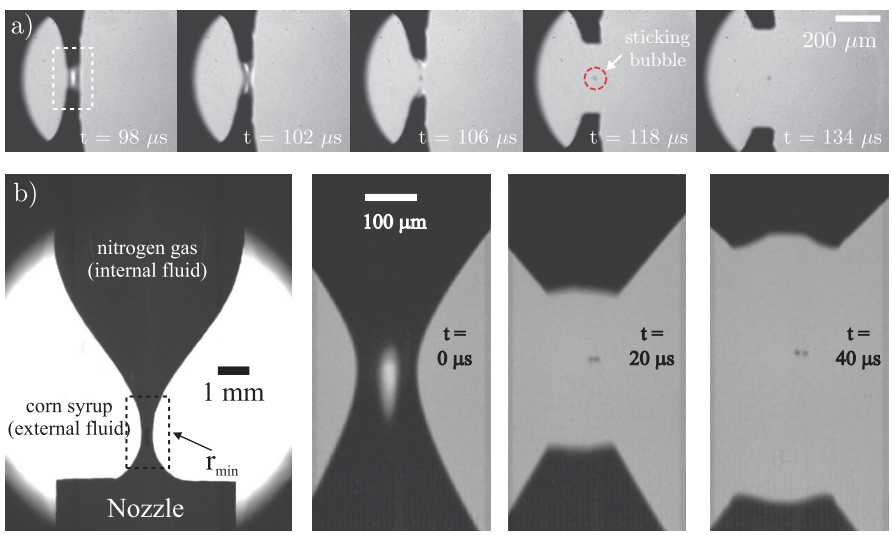

Figure 5.11: Analogy of break-up of a cylindrical cap (a) (zoom in top view Fig. 5.5) with the break-up of a cylindrical neck in bubble pinch-off (b) (reprint Burton et al. PRL 94, 184502, 2005). The break-up of a cylindrical cap, results in a sticking bubble.

lubricating air film, in analogy for bubble entrapment below drops falling on a solid surface. The bubble sizes increase in size with increasing impact velocity, consistent with a scaling argument $R_{bub}/R \sim \mathrm{Ca}^{1/3}$. By contrast at finite impact height, $h > 0$,

the entrapped bubbles are "sticking" to the substrate. Their size is a few microns and their formation is completely independent of the size and velocity of the impacting drops. The reason for this is that the formation process is dominated by the very fast coalescence, followed by the very fast pinchoff of an air cylinder.

Our findings will be of interest for applications such as coating and immersion lithography. Collisions between drops and the meniscus can occur in these geometries, but bubbles are usually not desired. We have shown that bubble sizes are strongly reduced when the initial contact occurs at a finite height above the substrate, which can be achieved by tuning the wettability of the substrate. However, we emphasize here that the geometry of impact can be much more complicated than the conditions studied in this chapter. In our experiments we avoided strongly convex or concave menisci, such that the small sessile drops always impact a nearly flat meniscus. Meniscus curvature indeed has a strong influence, in particular on the drainage dynamics of the air film. As mentioned in Fig. 5.2, the upward coalescence does not always lead to the entrapment of a bubble. We have not been able to quantify the parameters that determine whether or not a floating bubble will form. This remains an important open question.

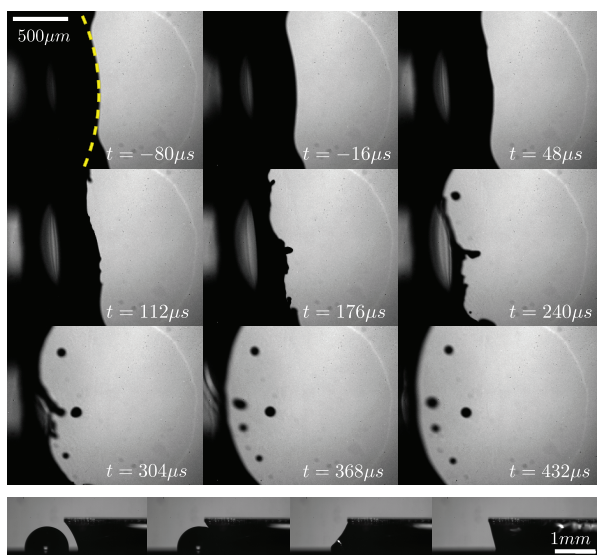

Figure 5.12: Complex break-up pattern of an air sheet (relatively large impacting droplet, $R = 1.1$ mm; height liquid bridge: 1.44 mm).

The importance of geometry is illustrated in Fig. 5.12, reporting the impact of a relatively large drop, with a drop size comparable to the height of the liquid bridge. In

that case, the shape of the air sheet and the subsequent drainage dynamics is strongly affected (R becomes comparable with the radius of curvature of the meniscus). One can clearly observe the destabilization of the air sheet, and how this results into multiple small bubbles. This is very different from the impact of small drops, for which we always observed break-up of a single filament. We speculate that the relevant parameter is the drop size in relation to the relevant dimensions of the meniscus, such as its curvature or its height, but this remains to be investigated. Also, in the theoretical approach we have focused on the cases where the impact is normal to the contact line of the meniscus. An inclined impact, could of course have an effect on the symmetry and build up of the lubricating air film, and the subsequent coalescence process. It would be interesting to investigate these effects in more detail, both experimentally and numerically.

5.6 Appendix: Matched asymptotic expansion for the dimple profile in droplet impact.

In this appendix we study a variation of the impact of a drop on a meniscus or on a solid wall. Namely we consider a rigid sphere impacting on a liquid reservoir. While the scaling laws for this geometry are identical to that of a drop impacting on a rigid solid, a full calculation of the profile requires a matched asymptotic expansion in which a well-defined outer geometry is taken into account. As will be shown, the outer cut-off is naturally introduced when introducing gravity. **Note:** in de appendix surface tension will be denoted by γ, since the final result contains the Euler-Mascheroni constant $\zeta \approx 0.57721...$

5.6.1 Formulation

The geometry of the problem is sketched in Fig. 5.13. We assume that the deformable liquid meniscus deflects a small amount $\delta(r)$, without affecting the lubricating gas pressure (i.e. pressure relation can be approximated by the pressure coming from a solid sphere approaching a solid wall). From figure 5.13, it is clear that in case of a deformable interface the air layer thickness becomes $h(r,t)+\delta(r,t)$. Hence, in order to use the lubricating pressure as derived in the sections before we have to assume:

1. $\delta(r,t) \ll h(r,t)$
2. $\frac{\partial \delta}{\partial t} \ll \frac{\partial h}{\partial t}$

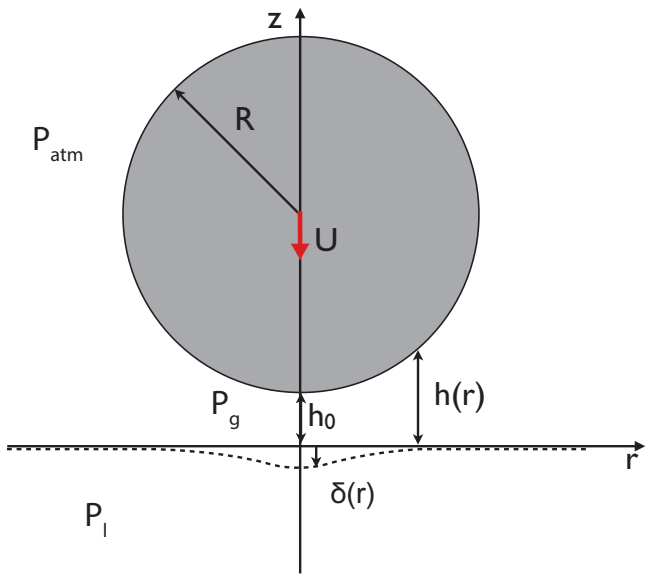

Figure 5.13: Sketch including all variables and symbols used in the derivation. The droplet (radius R) approaches the surface with a velocity U, hence the distance from the undisturbed water level is $h_0(t)$. While moving downwards it is assumed that the meniscus deforms with $\delta(r)$.

Under these assumptions (where $|\frac{dh_0}{dt}| = U$, the velocity of the droplet), we can write the pressure as [32].

$$P_{gas} = \frac{3\eta_g |\frac{dh_0}{dt}| R}{{h_0}^2 \left(1 + \frac{r^2}{2Rh_0}\right)^2} + P_{atm}, \tag{5.7}$$

With this, we can make a pressure balance at the interface of the bulk liquid/meniscus (equilibrium assumption liquid) at $z = -\delta$:

$$P_{liquid,interface} = P_{hydro} = P_{atm} + \rho_l g \delta, \tag{5.8}$$

If there exists a deformation δ, the interface will be curved with curvature κ. Due to Laplace pressure:

$$P_{liquid,interface} = P_{gas} - \gamma\kappa, \tag{5.9}$$

where $\kappa = \frac{\partial_{rr} z}{(1+(\partial_r z)^2)^{3/2}} + \frac{\partial_r z}{r(1+(\partial_r z)^2)^{1/2}}$. Then the pressure balance becomes:

$$P_{atm} + \rho g \delta = P_{gas} - \gamma\kappa. \tag{5.10}$$

Under the assumption of small $\partial_r z$, the curvature κ reduces to: $\partial_{rr} z + \frac{\partial_r z}{r}$. This curvature at the surface, $z = -\delta(r)$, combined with equation 5.10 gives

$$\frac{3\eta_g U R}{\left(h_0 + \frac{r^2}{2R}\right)^2} = -\gamma\left(\partial_{rr}\delta(r) + \frac{\partial_r \delta(r)}{r}\right) + \rho g \delta(r). \tag{5.11}$$

Note that $Ca = \frac{\eta_g U}{\gamma}$ and $\ell_c = \sqrt{\frac{\gamma}{\rho g}}$. Therefore the equation above can be simplified to:

$$\frac{3CaR}{h_0^2\left(1 + \frac{r^2}{2L^2}\right)^2} = -\left(\partial_{rr}\delta(r) + \frac{\partial_r \delta(r)}{r}\right) + \frac{1}{\ell_c^2}\delta(r), \tag{5.12}$$

where $L = \sqrt{h_0 R}$. This ordinary differential equation (ODE) must be supplemented with the boundary conditions (axi-symmetry and $\delta(r) \to 0$, for $r \to \infty$):

1. $\frac{\partial \delta(r)}{\partial r} \mid_{r\to 0} = 0$
2. $\delta(r) \mid_{r\to\infty} = 0$

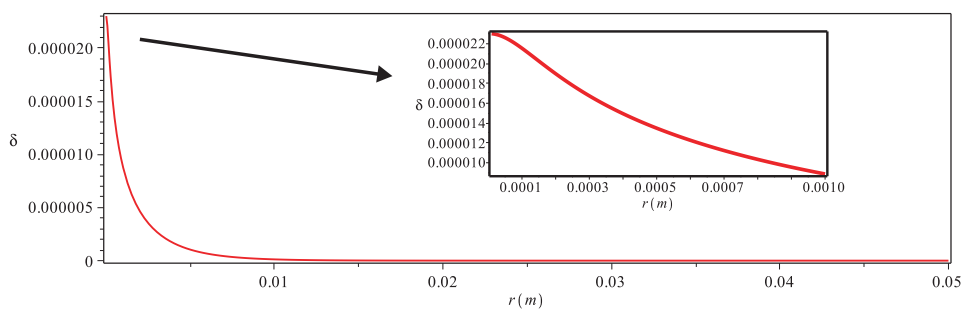

Figure 5.14: Numerical result to equation 5.12. Parameter values: $Ca = 2.5 \cdot 10^{-5}$, $\ell_c = 2.7 \cdot 10^{-3}$ m, $R = 1 \cdot 10^{-3}$ m and $h_0 = 1 \cdot 10^{-5}$ m. The inset is a zoom on the small scale dimple close to $r = 0$.

Equation 5.12 is solved numerically using Maple and shown in figure 5.14. This numerical solution clearly shows that the profile has two characteristic length scales. First, the bath is deflected up to a few millimeters from the impact location, which is the scale of the capillary length. As shown in the inset, however, the dimple profile has a characteristic width that is determined by the width of the lubrication pressure, and which is much smaller (about 0.1 millimeter). Based on this separation of length scales, we can therefore derive an analytical result with the method of matched

asymptotic expansions. In this method the solutions to the equation are searched on different length scales. In this problem two radial length scales are already defined: 1) outer length scale ℓ_c and 2) inner length scale L, pre factors in the outermost right term and outermost left term of equation 5.12 respectively.

5.6.2 Inner solution: inner length L.

We now introduce an expansion parameter $\varepsilon = \frac{L}{\ell_c}$, which can be assumed small for the initial dimple formation. To find the equation describing the interface deformation in the inner region , equation 5.12 is written in dimensionless form, using the following scaling

1. $r = r' \cdot \varepsilon \ell_c$,
2. $\delta(r) = \delta' \cdot \delta_I$,
3. $\frac{\partial \delta}{\partial r} = \frac{\delta_I}{L} \cdot \frac{\partial \delta'}{\partial r'}$,
4. $\frac{\partial^2 \delta}{\partial r^2} = \frac{\delta_I}{L^2} \cdot \frac{\partial^2 \delta'}{\partial r'^2}$,

where the primes denote the dimensionless form of the variables. Here δ_I is the characteristic deformation in the inner region. The dimensionless form of equation 5.12 reduces to:

$$\frac{3CaRL^2}{\delta_I h_0^2 \left(1 + \frac{r'^2}{2}\right)^2} = -\left(\partial_{r'r'}\delta' + \frac{\partial'_r \delta'}{r'}\right) + \frac{L^2}{\ell_c^2}\delta'. \tag{5.13}$$

Defining $\delta_I = \frac{3CaRL^2}{h_0^2}$, the above equation finally simplifies to

$$\frac{1}{\left(1 + \frac{r'^2}{2}\right)^2} = -\left(\partial_{r'r'}\delta' + \frac{\partial'_r \delta'}{r'}\right) + \varepsilon^2 \delta'. \tag{5.14}$$

Using $\varepsilon \ll 1$, the inner equation becomes

$$\frac{1}{\left(1 + \frac{r'^2}{2}\right)^2} = -\partial_{r'r'}\delta' - \frac{\partial'_r \delta'}{r'}. \tag{5.15}$$

This has the solution:

$$\delta'(r') = (C_{1I} + 1)\ln\left(r'\right) - \frac{1}{2}\ln\left(2 + r'^2\right) + C_{2I}, \tag{5.16}$$

which should satisfy the first boundary condition (i.e. $\frac{\partial \delta'}{\partial r'} |_{r\to 0} = 0$). Therefore $C_{1I} = -1$, reducing the above equation to:

$$\delta'(r') = -\frac{1}{2}\ln\left(2 + r'^2\right) + C_{2I}. \tag{5.17}$$

The second parameter C_{2I} will be determined by matching to the outer solution. Note that the logarithmic divergence as $r \to \infty$ makes it necessary to introduce an outer cut-off. Otherwise, the result would be an infinite deformation at large r.

5.6.3 Outer solution: outer ℓ_c

A similar approach as for the inner region, can now be applied to find the governing equation and its solution in the outer region. The scalings used are as follows:

1. $r = \widehat{r} \cdot \ell_c$,
2. $\delta(r) = \widehat{\delta} \cdot \delta_O$,
3. $\frac{\partial \delta}{\partial r} = \frac{\delta_O}{\ell_c} \cdot \frac{\partial \widehat{\delta}}{\partial \widehat{r}}$,
4. $\frac{\partial^2 \delta}{\partial r^2} = \frac{\delta_O}{\ell_c^2} \cdot \frac{\partial^2 \widehat{\delta}}{\partial \widehat{r}^2}$,

where the hatted variables denote the dimensionless form of the variables. The dimensionless form of equation 5.12 reduces to:

$$\frac{3CaR\ell_c^2}{\delta_O h_0^2 \left(1 + \frac{\widehat{r}^2 \ell_c^2}{2L^2}\right)^2} = -\partial_{\widehat{r}\widehat{r}}\widehat{\delta} - \frac{\partial_{\widehat{r}}\widehat{\delta}}{\widehat{r}} + \widehat{\delta}. \tag{5.18}$$

Defining again a characteristic deformation $\delta_O = \frac{3CaR\ell_c^2}{h_0^2}$, the equation simplifies to

$$\frac{1}{\left(1 + \frac{\widehat{r}^2}{2\varepsilon^2}\right)^2} = -\partial_{\widehat{r}\widehat{r}}\widehat{\delta} - \frac{\partial_{\widehat{r}}\widehat{\delta}}{\widehat{r}} + \widehat{\delta}. \tag{5.19}$$

If we assume that $\varepsilon \ll \widehat{r}$ such that $\frac{\widehat{r}^2}{2\varepsilon^2} >> 1$ the outer region equation simplifies to:

$$0 = -\partial_{\widehat{r}\widehat{r}}\widehat{\delta} - \frac{\partial_{\widehat{r}}\widehat{\delta}}{\widehat{r}} + \widehat{\delta}(\widehat{r}). \tag{5.20}$$

Equation 5.20 has the solution:

$$\widehat{\delta}(\widehat{r}) = C_{1O} I_0(\widehat{r}) + C_{2O} K_0(\widehat{r}), \tag{5.21}$$

where I_0 and K_0 are the modified Bessel functions of the first and second kinds, respectively. The solution should satisfy the second boundary condition (i.e. $\widehat{\delta}(\widehat{r})\mid_{r\to\infty}= 0$). Since the first term of equation 5.21 diverges for $r\to\infty$ ($I_0\to 0$), C_{1O} should be zero. Therefore,

$$\widehat{\delta}(\widehat{r}) = C_{2O}K_0(\widehat{r}). \tag{5.22}$$

5.6.4 Intermediate length scale: matching.

As matched asymptotic expansion already suggests, the solutions of the inner- and outer-region should match in the asymptotic limits. Intuitively this suggests that the inner solution at 'infinity' (in terms of the inner length scale variable) should match with the outer solution at 'zero' (in terms of the outer length scale variable), i.e. $\delta'(r')\mid_{r'\to\infty}= \widehat{\delta}(\widehat{r})\mid_{\widehat{r}\to 0}$. Here we apply the formal procedure, by introducing the intermediate length $\sqrt{\varepsilon}\ell_c$, giving variables:

1. $r = \widetilde{r}\sqrt{\varepsilon}\ell_c$,
2. $\widetilde{r} = \frac{r}{\sqrt{\varepsilon}\ell_c} = \frac{r'\varepsilon\ell_c}{\sqrt{\varepsilon}\ell_c} \to r' = \frac{\widetilde{r}}{\sqrt{\varepsilon}}$,
3. $\widetilde{r} = \frac{r}{\sqrt{\varepsilon}\ell_c} = \frac{\widehat{r}\varepsilon\ell_c}{\sqrt{\varepsilon}\ell_c} \to \widehat{r} = \widetilde{r}\sqrt{\varepsilon}$.

Then the solutions (eq. 5.17 and 5.22) become, respectively:

$$\delta(\widetilde{r}) = -\frac{\delta_I}{2}\ln\left(2+\left(\frac{\widetilde{r}}{\sqrt{\varepsilon}}\right)^2\right) + \delta_I C_{2I} \tag{5.23}$$

$$\delta(\widetilde{r}) = \delta_O C_{2O} K_0\left(\widetilde{r}\sqrt{\varepsilon}\right). \tag{5.24}$$

In the limit of small ε (hence, $\frac{\widetilde{r}}{\sqrt{\varepsilon}} \gg 1$ and $\widetilde{r}\sqrt{\varepsilon} \ll 1$ expansions can be made. For the inner solution this gives

$$\delta(\widetilde{r}) = -\delta_I \ln\left(\frac{\widetilde{r}}{\sqrt{\varepsilon}}\right) + \delta_I C_{2I} - \frac{\delta_I}{\left(\frac{\widetilde{r}}{\sqrt{\varepsilon}}\right)^2} + \mathscr{O}(4), \tag{5.25}$$

while for the outer solution this gives (with ζ the Euler-Mascheroni constant)

$$\delta(\widetilde{r}) = \delta_O C_{2O}\left(\ln(2) - \ln\left(\widetilde{r}\sqrt{\varepsilon}\right) - \zeta\right) + \mathscr{O}(..). \tag{5.26}$$

Comparing both expansions

$$\delta(\widetilde{r}) = -\delta_I \ln(\widetilde{r}) + \delta_I\left(\ln\left(\sqrt{\varepsilon}\right) + C_{2I}\right) + \mathscr{O}(..) \tag{5.27}$$

$$\delta(\widetilde{r}) = -\delta_O C_{2O}\ln(\widetilde{r}) + \delta_O C_{2O}\left(\ln(2) - \ln\left(\sqrt{\varepsilon}\right) - \zeta\right) + \mathscr{O}(..) \tag{5.28}$$

From this one can see from the $\widetilde{r}$-dependent terms

$$\delta_I = \delta_O C_{2O} \rightarrow C_{2O} = \frac{\delta_I}{\delta_O}, \tag{5.29}$$

$$C_{2O} = \frac{\delta_I}{\delta_O} = \frac{\frac{3CaRL^2}{h_0^2}}{\frac{3CaR\ell_c^2}{h_0^2}} = \frac{L^2}{\ell_c^2} = \varepsilon^2. \tag{5.30}$$

Using this in the remaining first order terms:

$$\delta_I \left(\ln\left(\sqrt{\varepsilon}\right) + C_{2I}\right) = \delta_O C_{2O} \left(\ln(2) - \ln\left(\sqrt{\varepsilon}\right) - \zeta\right) \tag{5.31}$$

$$\delta_I \left(\ln\left(\sqrt{\varepsilon}\right) + C_{2I}\right) = \delta_I \left(\ln(2) - \ln\left(\sqrt{\varepsilon}\right) - \zeta\right) \tag{5.32}$$

$$C_{2I} = \ln(2) + \ln\left(\frac{1}{\varepsilon}\right) - \zeta \tag{5.33}$$

The final solutions are in dimensional variables.
Inner:

$$\delta(r) = -\frac{3CaRL^2}{h_0^2}\left[\frac{1}{2}\ln\left(2 + \frac{r^2}{L^2}\right) - \left(\ln(2) - \zeta + \ln\left(\frac{\ell_c}{\sqrt{Rh_0}}\right)\right)\right] \tag{5.34}$$

Outer:

$$\delta(r) = \frac{3CaRL^2}{h_0^2} K_0\left(\frac{r}{\ell_c}\right) \tag{5.35}$$

For parameter values: $Ca = 2.5 \cdot 10^{-5}$, $\ell_c = 2.7 \cdot 10^{-3}$ m, $R = 1 \cdot 10^{-3}$ m and $h_0 = 1 \cdot 10^{-5}$ m, the analytical and numerical result is compared in figure 5.15. Indeed, the inner solution (blue solid line, eq. 5.34) and outer solution (green solid line, eq. 5.35) are in accordance with the numerical solution (red dashed line) in the inner and outer regime respectively. The inset shows a zoom on the smaller scale dimple structure where also the cross-over between the inner and outer regime becomes visible. Note that this result is based on the assumption $\frac{\delta(r=0)}{h_0} \ll 1$, which gives $\mathrm{Ca} \ll \left(\frac{h_0}{R}\right)^2$.

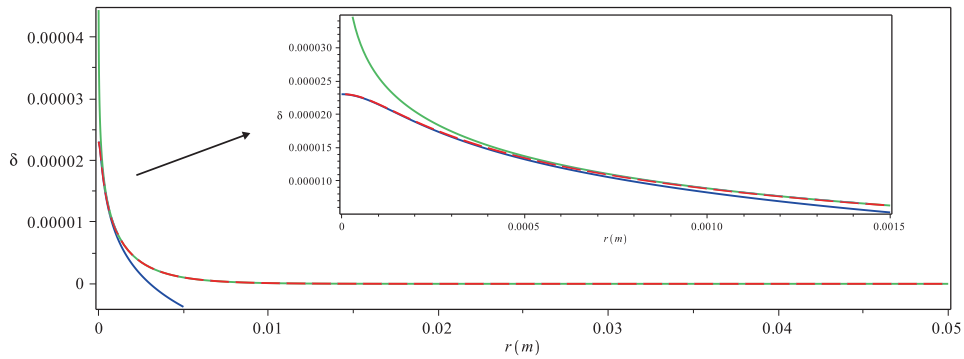

Figure 5.15: Red dashed line represents the numerical result to equation 5.12. Parameter values: $Ca = 2.5 \cdot 10^{-5}$, $\ell_c = 2.7 \cdot 10^{-3}$ m, $R = 1 \cdot 10^{-3}$ m and $h_0 = 1 \cdot 10^{-5}$ m. The analytical solution is shown as well: the outer solution in green (eq. 5.35) and the inner solution in blue (eq. 5.34). The inset is a zoom on the small scale dimple.

References

[1] A.L. Yarin. Drop impact dynamics: Splashing, spreading, receding, bouncing.. *Annual Review of Fluid Mechanics*, 38:159–192, 2006.

[2] H. N. Oguz and A. Prosperetti. Bubble entrainment by the impact of drops on liquid surfaces. *Journal of Fluid Mechanics*, 219:143–179, 1990.

[3] P. Tsai, R. C. A. van der Veen, M. van de Raa, and D. Lohse. How micropatterns and air pressure affect splashing on surfaces. *Langmuir*, 26(20):16090–16095, 2010.

[4] P. Tsai, S. Pacheco, C.Pirat, L. Lefferts, and D. Lohse. Drop impact upon micro- and nanostructured superhydrophobic surfaces. *Langmuir*, 25(20):12293–12298, Oct 2009.

[5] D.E. Cole and J.L. Liow. Liow (2004) - Bubble Entrapment During Water Drop Impacts. *15th Australasian Fluid Mechanics Conference*, pages 1–4, Dec 2004.

[6] J.L. Liow and D.E. Cole. Bubble entrapment mechanisms during the impact of a water drop. *16th Australasian Fluid Mechanics Conference*, pages 866–869, 2007.

[7] G.E. Charles and S.G Mason. The coalescence of liquid drops with flat liquid/liquid interfaces. *Journal of Colloid Science*, 15(3):236 – 267, 1960.

[8] Q. Deng, A. V. Anilkumar, and T. G. Wang. The role of viscosity and surface tension in bubble entrapment during drop impact onto a deep liquid pool. *Journal of Fluid Mechanics*, 578:119–138, 2007.

[9] S.T. Thoroddsen, T.G. Etoh, and K. Takehara. Air entrapment under an impacting drop. *Journal of Fluid Mechanics*, (478):125–134, 2003.

[10] L. Esmailizadeh and R Mesler. Bubble entrainment with drops. *Journal of Colloid And Interface Science*, 110(2):561–574, 1986.

[11] D. B. van Dam and C. Le Clerc. Experimental study of the impact of an ink-jet printed droplet on a solid substrate. *Physics of Fluids*, 16(9), SEP 2004.

[12] S. Mandre, M. Mani, and M. P. Brenner. Precursors to splashing of liquid droplets on a solid surface. *Phys. Rev. Lett.*, 102:134502, Mar 2009.

[13] M. Mani, S. Mandre, and M. P. Brenner. Events before droplet splashing on a solid surface. *Journal of Fluid Mechanics*, 647:163–185, 2010.

[14] M. M. Driscoll, C. S. Stevens, and S. R. Nagel. Thin film formation during splashing of viscous liquids. *Phys. Rev. E*, 82:036302, Sep 2010.

[15] P. D. Hicks and R. Purvis. Air cushioning in droplet impacts with liquid layers and other droplets. *Physics of Fluids*, 23(6), JUN 2011.

[16] R. C. A. van der Veen, T. Tran, D. Lohse, and C. Sun. Direct measurements of air layer profiles under impacting droplets using high-speed color interferometry. *Phys. Rev. E*, 85:026315, Feb 2012.

[17] T.G. Leighton. From seas to surgeries, from babbling brooks to baby scans: The acoustics of gas bubbles in liquids. 18(25):32673314, 2004.

[18] D.C. Blanchard and A.H. Woodcock. Bubble Formation and Modification in the Sea and its Meteorological Significance. *Tellus*, 9:145–158, May 1957.

[19] M. Switkes, M. Rothschild, T.a Shedd, T. A. Burnett, and M. S. Yeung. Bubbles in immersion lithography. *Journal of Vacuum Science and Technology B*, 23:2409–2412, December 2005.

[20] Y Couder, S Protière, E Fort, and A Boudaoud. Dynamical phenomena: Walking and orbiting droplets. *Nature*, 437(7056):208–208, September 2005.

[21] Y. Couder, E. Fort, C.-H. Gautier, and A. Boudaoud. From bouncing to floating: Noncoalescence of drops on a fluid bath. *Phys. Rev. Lett.*, 94:177801, May 2005.

[22] T. Gilet and J. W. M. Bush. The fluid trampoline: droplets bouncing on a soap film. *Journal of Fluid Mechanics*, 625:167–203, Apr 2009.

[23] J. Sigler and R Mesler. The behaviour of the gas film formed upon drop impact with a liquid surface. *Journal of Colloid And Interface Science*, 134(2):459–474, 1990.

[24] L. Duchemin, J Eggers, and C. Josserand. Inviscid coalescence of drops. *Journal of Fluid Mechanics*, 487:167–178, 2003.

[25] A. Marchand, T. S. Chan, J. H. Snoeijer, and B. Andreotti. Air entrainment by contact lines of a solid plate plunged into a viscous fluid. *Phys. Rev. Lett.*, 108:204501, May 2012.

[26] H. Benkreira and M.I. Khan. Air entrainment in dip coating under reduced air pressures. *Chemical Engineering Science*, 63(2):448 – 459, 2008.

[27] H. Benkreira and J.B. Ikin. Dynamic wetting and gas viscosity effects. *Chemical Engineering Science*, 65(5):1790 – 1796, 2010.

[28] K. G. Winkels, I.R. Peters, F. Evangelista, M. Riepen, A. Daerr, L. Limat, and J.H. Snoeijer Receding contact lines: From sliding drops to immersion lithography. *Eur. Phys. J. Special Topics*, 192:195–205, 2011.

[29] M. M. Driscoll and S. R. Nagel. Ultrafast interference imaging of air in splashing dynamics. *Phys. Rev. Lett.*, 107:154502, Oct 2011.

[30] J. de Ruiter, J. Min Oh, D. van den Ende, and F. Mugele. Dynamics of collapse of air films in drop impact. *Phys. Rev. Lett.*, 108:074505, Feb 2012.

[31] W. Bouwhuis, R. C. A. van der Veen, T. Tran, D. L. Keij, K. G. Winkels, I. R. Peters, D. van der Meer, C. Sun, J. H. Snoeijer, and D. Lohse. Maximal Air Bubble Entrainment at Liquid-Drop Impact. *Phys. Rev. Lett.*, 109:264501, Dec 2012.

[32] R. H. Davis, J.-M. Serayssol, and E. J. Hinch. The elastohydrodynamic collision of two spheres. *Journal of Fluid Mechanics*, 163:479–497, 1986.

[33] M. Wu, T. Cubaud, and C.-M. Ho. Scaling law in liquid drop coalescence driven by surface tension. *Phys. Fluids*, 16(7):L51–L54, 2004.

[34] J. D. Paulsen, J. C. Burton, and S. R. Nagel. Viscous to inertial crossover in liquid drop coalescence. *Phys. Rev. Lett.*, 106:114501, Mar 2011.

[35] J. C. Burton, R. Waldrep, and P. Taborek. Scaling and instabilities in bubble pinch-off. *Phys. Rev. Lett.*, 94:184502, May 2005.

[36] J. M. Gordillo and M. A. Fontelos. Satellites in the inviscid breakup of bubbles. *Phys. Rev. Lett.*, 98:144503, Apr 2007.

[37] J. Eggers, M. A. Fontelos, D. Leppinen, and J. H. Snoeijer. Theory of the collapsing axisymmetric cavity. *Phys. Rev. Lett.*, 98:094502, Mar 2007.

[38] R. Bergmann, D. van der Meer, M. Stijnman, M. Sandtke, A. Prosperetti, and D. Lohse. Giant bubble pinch-off. *Phys. Rev. Lett.*, 96:154505, Apr 2006.

6

Initial spreading of low-viscosity drops on partially wetting surfaces * †

Liquid drops start spreading directly after brought into contact with a partial wetting substrate. Although this phenomenon involves a three-phase contact line, the spreading motion is very fast. We study the initial spreading dynamics of low-viscosity drops, using two complementary methods: Molecular Dynamics simulations and high-speed imaging. We access previously unexplored length- and time-scales, and provide a detailed picture on how the initial contact between the liquid drop and the solid is established. Both methods unambiguously point towards a spreading regime that is independent of wettability, with the contact radius growing as the square root of time.

6.1 Introduction

How fast can a liquid drop spread over a surface? This basic question is relevant for applications ranging from printing and coating, to agricultural applications [1–5]. In

*Published as: K. G. Winkels, J. H. Weijs, A. Eddi and J.H. Snoeijer, "Initial spreading of low-viscosity drops on partially wetting surfaces", *Phys. Rev. E*, **85**, 055301(R) (2012).

†The experimental work in this chapter is part of the present thesis. The numerical simulations are due to Joost H. Weijs.

the final stage of drop spreading the dynamics are governed by Tanner's law, which relates the radius of the wetted area with time as $r \sim t^{1/10}$ [6, 7]. This extremely slow dynamics emerges from a balance between surface tension and viscous forces close to the contact line [3]. Much less is known about the early stages of spreading, just after a spherical drop is brought into contact with a substrate at vanishing approach velocity. In contrast to Tanner's law, this dynamics is very fast [8–12]: capillary energy suddenly becomes available when the drop touches the solid, and this energy is concentrated into a singular point of contact. It has remained unclear whether or not the wetting conditions can influence such rapid inertial flows [13–15].

The initial stages of drop spreading are strongly reminiscent of the coalescence of two spherical drops of liquid, which very rapidly merge after contact is established [16–21]. For low-viscosity liquids such as water, it is well-known that the contact area between the drops grows as $r \sim t^{1/2}$ during coalescence. This can be explained from the balance of the inertial pressure inside the drop, $\sim \rho(dr/dt)^2$, and the capillary pressure, $\sim \gamma R/r^2$. Here ρ is the density, γ the surface tension, and R the drop radius. Interestingly, an identical scaling law was observed experimentally for water drops spreading on a *completely wetting* surface [8]; apparently, the presence of a three-phase contact line does not affect the pressure balance during the initial phase of spreading. A rather different picture emerged, however, for drops spreading on *partially wetting* surfaces [9, 10, 12]. The dynamics was found to depend strongly on surface wettability, $r \sim t^{\alpha}$, with a non-universal exponent α that varies with the equilibrium contact angle [9]. This raises a number of intriguing questions: How can the contact line, and the surface chemistry, affect the "coalescence" of a drop with a surface? Are the initial stages of spreading truly non-universal, or is there a hidden regime at smaller times? How is contact established on a molecular scale?

In this chapter we reveal the initial spreading dynamics of low-viscosity drops, using two complementary methods: Molecular Dynamics simulations of Lennard-Jones nanodrops and high-speed imaging of experiments on millimeter-sized water drops [Fig. 6.1]. We access previously unexplored length- and time-scales, and provide a detailed picture on how the initial contact between the liquid drop and the solid is established. While simulations and experiments describe different dynamical regimes, both methods unambiguously point towards a universal spreading regime independent of wettability, consistent with the inertia-capillary balance $r \sim t^{1/2}$. This contrasts the scenario proposed by [9]: At very early times after contact, the spreading exponent is independent of wettability, for contact angles ranging from complete wetting to very hydrophobic.

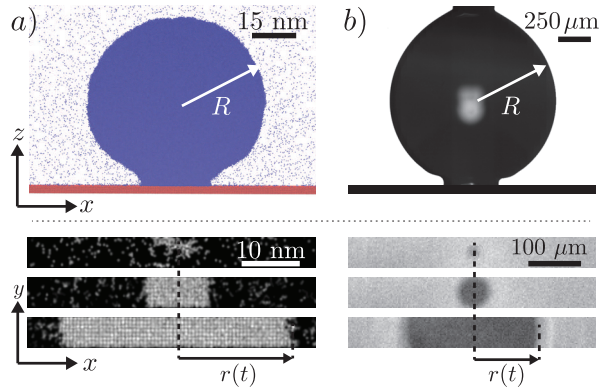

Figure 6.1: Initial stages of drop spreading on partially wetting surfaces of varying wettability. (a) Molecular Dynamics simulations of Lennard-Jones nanodrops ($R =$ 30nm), and (b) Experiments of water drops ($R = 0.5$mm). The top panels show side views of the liquid drop just after it has made contact with the partially wetting substrate. Lower panels are bottom views at times (a) $t = 10, 35, 400$ ps, and (b) $t = 4, 8, 44$ μs. The contact radius $r(t)$ can be measured in time.

6.2 Molecular Dynamics Simulations

The use of Molecular Dynamics simulations (MD) allows for studying the initial contact between a liquid drop and a solid substrate down to molecular scale. To reveal the fundamental mechanism of contact and subsequent spreading, we use a generic Lennard-Jones liquid. The advantage of the molecular approach is that, unlike continuum modeling, no assumptions on the moving contact line singularity [3] are needed. In MD, the wetting characteristics are directly controlled by the solid-liquid interaction, which determines the equilibrium contact angle θ_{eq} [22]. The challenge, however, is to achieve sufficiently large drop sizes to recover a hydrodynamic regime. We therefore study a quasi-two-dimensional geometry rather than axisymmetric drops, in which the system size in the y-direction is only 15 molecular sizes [cf. Fig. 6.1(b)]. Indeed, contact problems such as coalescence are known to be essentially 2D phenomena and the same is expected here [16, 23].

We perform simulations on binary systems, in which two types of particles exist: fluid particles that can move around either in the gas or liquid phase, and solid particles which are frozen on an fcc-lattice and constitute the solid substrate [24]. All particle interactions are defined by the Lennard-Jones potential:

$$\phi_{ij}(r) = 4\varepsilon_{ij}\left[\left(\frac{\sigma_{ij}}{r}\right)^{12} - \left(\frac{\sigma_{ij}}{r}\right)^{6}\right] . \tag{6.1}$$

Here, ε_{ij} is the interaction strength between particles i and j and σ_{ij} the characteristic size of the atoms. This size is the same for all interactions, $\sigma_{ij} = \sigma = 0.34$ nm. The potential function is truncated at $r_c = 5\sigma$ (1.7 nm) where ϕ_{ij} is practically zero. The mass of the atoms was set at 20 amu, and a timestep of 1.75 fs was found to be sufficient to accurately model these systems. The interaction strengths between the fluid atoms are $\varepsilon_{ll} = 1.2k_BT$, with k_B the Boltzmann constant and T the temperature. The simulations are done in the NVT-ensemble, where the temperature is held at 300K using a thermostat, which is below the critical point for a Lennard-Jones fluid with the interaction strengths used. The fluid particles (amount: $N_l = 304,192$) are initially positioned on an fcc-lattice (shaped with a cubic outline) far from the substrate ($N_s = 78,300$), but are free to move around and relax towards an equilibrium drop shape. Periodic boundary conditions are present in the lateral directions. The dimensions of the quasi-2D system are 240 nm, 5.1 nm and 120 nm in the x-, y- and z-directions respectively (Fig. 6.1). The depth of the system is short enough to suppress the Rayleigh-Plateau instability and leads to an infinitely long cylindrical-cap shaped drop.

The interaction strength between the solid and fluid defines the contact angle [22]. We considered four different wettabilities (thus, four different values of ε_{sl}): $\varepsilon_{sl} = (0.3, 0.4, 0.8, 1.2)k_BT$, giving $\theta_{eq} = (115^\circ, 100^\circ, 60^\circ, 0^\circ) \pm 10^\circ$. The liquid density was measured to be $\rho = 664$ kg/m^3, and the surface tension γ was measured in a separate, planar system at $\gamma = 0.017$ J/m^2. The viscosity of the liquid was measured in another separate system (Poiseuille-geometry) to be $\eta = 3.64 \cdot 10^{-4}$ kg/(m·s).

The following procedure was used to bring the drop into contact with the substrate. First, the liquid is allowed to equilibrate far away (32 nm) from the substrate. During this stage, the drop will assume its cylindrical shape ($R = 30$ nm) and the liquid equilibrates with the vapour phase. Next, a body force is briefly applied on the fluid atoms until the drop moves towards the substrate. Just before the drop comes into contact with the substrate, the center-of-mass velocity of the drop is subtracted from the atom velocities such that the drop now 'hovers' above the substrate. Due to the close proximity of the substrate (around 1 nm) the thermal fluctuations of the interface lead to first contact between the drop and the substrate after which the drop starts to spread. Using this method, the approach velocity of the drop towards the substrate is zero and is not a parameter in this problem.

What happens during the initial contact? In these early stages one cannot yet speak about a continuous liquid phase in contact with the solid. Instead, one first

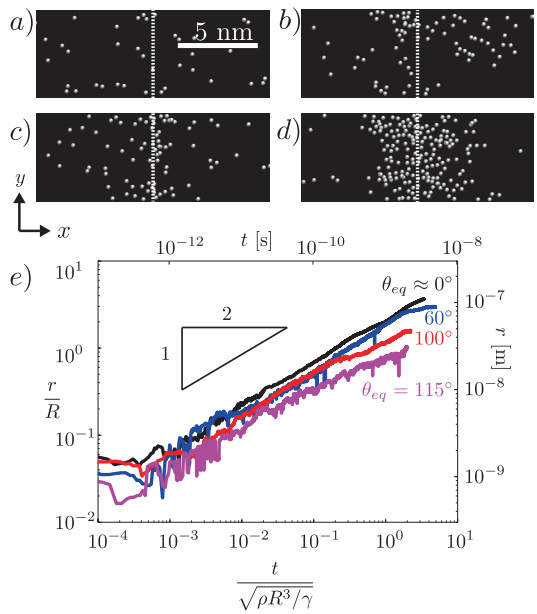

Figure 6.2: Molecular Dynamics results. (a-d) "Bottom views" showing the molecules within 0.5nm from the substrate just prior to and after initial contact ($t = -70$ ps, -25 ps, -5 ps and 35 ps, respectively). (a) A small number of molecules from the vapor phase is close to the substrate. (b,c) Some fluctuating patches of higher density form. (d) A region of high liquid density nucleates at the substrate, from which one can measure $r(t)$. (e) Radius of wetted area as a function of time for varying substrate wettabilities θ_{eq}. Once the contact is established, we observe a power-law with exponent 1/2 for all values of θ_{eq}. Results are displayed in SI-units on the right and top axis, and displayed in dimensionless form on the left and bottom axis. Contact radius r is rescaled with the initial drop radius R, time is rescaled with the inertial time scale $\tau_\rho = \sqrt{\rho R^3/\gamma}$.

encounters the discrete, molecular nature of the fluid. Figures 6.2(a-d) show snapshots of the molecules that are within 0.5 nm from the substrate, represented as white dots. First a number of vapor molecules is randomly distributed over the surface [Fig. 6.2(a)]. As time progresses, more molecules come into contact and form fluctuating "patches" of high liquid density at the substrate [Figs. 6.2(b,c)]. The boundaries of these patches is extracted by computing the number density field of atoms near the surface, and taking the iso-density contour half-way between the liquid and vapor density. Eventually, the patch becomes sufficiently large to span the entire depth

of the quasi-2D simulation domain, from which we define the time of contact [Fig. 2(d)]. The exact definition of $t = 0$ does not influence our main conclusions below. From that moment, we track the boundaries of this wetting patch, which are the moving contact lines. The contact lines become sharper and are well-defined during the spreading, as can be seen in Fig. 6.1(a). Note that while the average vapor density close to the surface is slightly larger than in the bulk, the surface coverage is very low and does not represent a precursor film.

The key result of our MD simulations is that, once the liquid drop has established contact with the surface, the spreading follows a single power law. Figure 6.2(e) shows the contact radius r versus time on surfaces with varying wettability. For all contact angles θ_{eq} we observe a scaling consistent with $r \sim t^{1/2}$ (best-fit exponent: 0.48). It turns out that the contact angle of the substrate θ_{eq} does have an influence on the spreading, but only through the prefactor: the exponent is always very close to 1/2. The prefactor increases as the contact angle decreases, such that drops spread faster on the more hydrophilic surfaces.

Despite the very small length- and time-scales in these simulations, the spreading appears to be consistent with the hydrodynamic picture of inertia-dominated coalescence [16, 18] The left axis and bottom axis in Fig. 6.2(e) represent the data in dimensionless units, where lengths are scaled with the initial drop radius R and time with the inertial scale $\tau_\rho = \sqrt{\rho R^3/\gamma}$. In these units, the data span a range similar to previous experiments on millimeter-sized water drops [8, 9].

6.3 Experiments

To verify whether the spreading behavior observed in MD is also found experimentally, we carried out experiments in a previously unexplored regime. The required spatial and temporal resolution is achieved by high-speed recording of drop spreading *from below*, using transparent substrates and recording rates up to 600,000 frames/second. Typical images are shown in Fig. 6.1b. The high-speed camera (Photron SA 1.1) is connected to a microscope (Zeiss Axiovert 25), which in combination with a 10X microscope objective (Zeiss A-plan, 10X) and reflective illumination gives a maximum resolving power of 2 μm/pixel. To capture a large period of the spreading process, frame rates used are in the range of 10-600kfps. Quéré *et al.* [8] and Bird *et al.* [9], have shown that data for different drop sizes collapse by inertial rescaling. As here we focus on the influence of wettability, we consider only one drop radius $R = 0.5 \pm 0.01$ mm.

To investigate the effect of wettability on the spreading, we performed experiments with water drops on three different substrates with different equilibrium con-

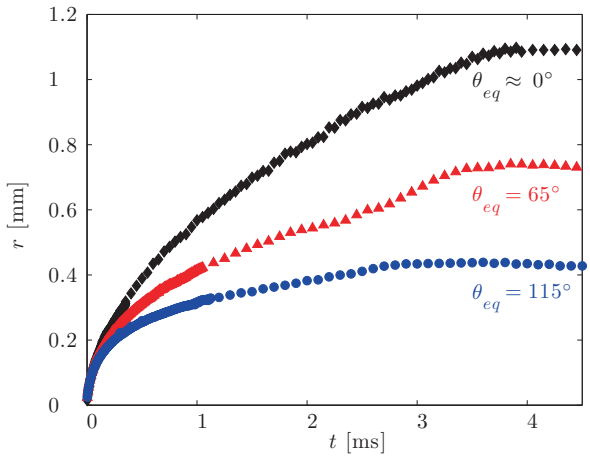

Figure 6.3: Experimental measurements of contact radius r plotted as function of time t for different substrate wettabilities. Results for three different equilibrium contact angles are plotted: clean glass ($\theta_e \approx 0°$; ◆), coated glass ($\theta_e = 65°$; ▲), teflon coated glass ($\theta_e = 115°$; ●). The curves represent averaged data of repeated measurements (five or more for each θ_{eq}) per substrate for drops with radius $R = 0.5$ mm, showing the reproducibility of the experiments.

tact angle θ_{eq}: clean glass (almost perfectly wetting, $\theta_{eq} \approx 0°$), coated glass ($\theta_r = 55°$; $\theta_a = 75°$; $\theta_{eq} = 65°$) and teflon coated glass ($\theta_r = 110°$; $\theta_a = 120°$; $\theta_{eq} = 115°$). In order to avoid any condensation effects prior to spreading, the surrounding air is saturated with nitrogen gas. A thin needle is fixed at height $D = 1 \pm 0.02$ mm above the substrate, thereby setting the initial radius R of the spreading drop (height $D = 2R$). With a syringe pump set at a constant volume rate of 1μl/min a pendant drop is grown at the needle tip, until it touches the substrate. This generates approach velocities $< 2 \cdot 10^{-5}$ m/s, so that the outer gas dynamics has a negligible influence on the contact process. The radius of contact $r(t)$ is determined from images as in Fig. 6.1b, using a custom-made edge-detection algorithm in Matlab that finds the maximum image intensity slope in every frame.

Our experiments confirm a single power law during the initial stages of contact. The measurements of the contact radius $r(t)$ are shown in Fig. 6.3 on linear axes. One observes that the data fall onto three different curves, corresponding to the three values of θ_{eq}. The curves separate about 0.1 ms after contact, showing a dependence on wettability at later times. However, the early-time dynamics are independent of wettability. This is revealed in Fig. 6.4, which shows the same data on

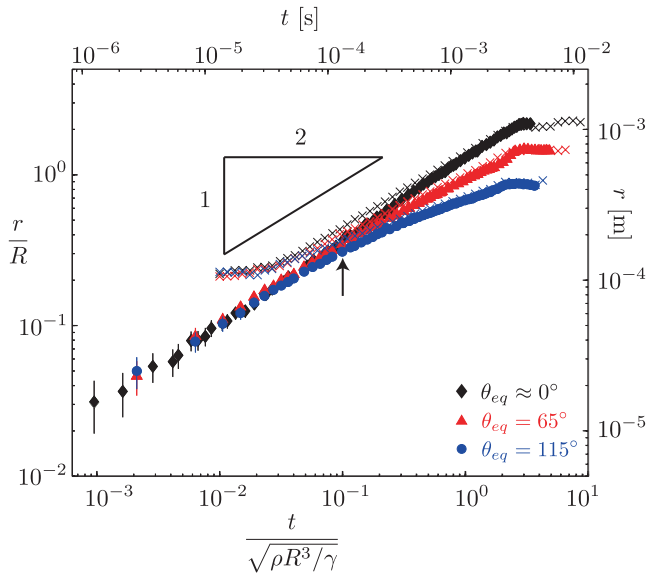

Figure 6.4: Experimental results. Contact radius r measured as a function of time (top and right axis) for three different equilibrium contact angles: clean glass ($\theta_e \approx 0°$; ◆), coated glass ($\theta_e = 65°$; ▲), and teflon coated glass ($\theta_e = 115°$; ●). The data shown, is an average of at least 5 measurements. The error bars denote the statistical error, which is larger than the measurement accuracy. On the left and bottom axis the data is normalized by the drop radius R and inertial time $\tau_\rho = \sqrt{\rho R^3/\gamma}$ respectively. A new regime is observed at earlier times, where the spreading is *independent* of the equilibrium contact angle. The colored crosses are reprinted data by Bird et al. [9] (corresponding with: $\theta_{eq} = 3°$, ×; 43°, ×; and 117°, ×). The arrow indicates the smallest times that were accurately resolved in the study by Bird *et al.*

log-log scale. We find that our data for different θ_{eq} perfectly collapse at early times ($t/\tau_\rho < 0.04$), and display an exponent close to $1/2$ (best fit: 0.55). We reprinted the data by Bird *et al.* [9] (crosses) for completeness, and find a perfect agreement with our data at $t/\tau_\rho > 0.1$, which is the range of accurate resolution in ref. [9]. The upper/right axis represent SI-units, while for the lower/left axis we employ the inertial scaling. Thus, the key point is that our measurements reveal a regime where wettability has no effect on the spreading at early times, not even in the prefactor.

6.4 Discussion

We have shown that early stage spreading of low-viscosity drops on a partially wetting substrate is independent of wettability. The wetted area is found to grow as $r \sim t^{1/2}$, for all considered wettabilities: we find no influence on the spreading exponent by the presence of a contact line. This suggests that the mechanism of capillary wave generation, invoked to explain θ_{eq}-dependent spreading exponents [9], cannot be the dominant factor at very early times. Still, such capillary waves could be relevant for explaining the later stages of spreading in Fig. 6.4, where a departure from the 1/2 scaling is observed. However, this departure first arises when $r/R \gtrsim 0.2$, in which case self-similarity of the bridge connecting the liquid drop and the substrate is lost, and scaling cannot be assumed a priori. It therefore remains a challenge to explain the moment when the effect of θ_{eq} becomes apparent in the experiments. There is, however, a subtle difference between the MD simulations and the experiments regarding the prefactor of the spreading law. For the experiments we observe a perfect collapse of the data on a single curve at early times. By contrast, the MD curves do not collapse, but the prefactor increases with decreasing θ_{eq}. We can point out at least two possible origins for this difference. First, the time- and length-scales of the two systems differ by orders of magnitude. In addition the simulations and experiments are not dynamically similar. While the rescaled results of Fig. 6.2 and 6.4 are very close, the Reynolds numbers defined as $\mathrm{Re} = \rho r(dr/dt)/\eta$ are very different: it is order unity in MD and order 100 in experiments. This suggests that the MD could be influenced by viscous effects, and it would be interesting to further investigate spreading for highly viscous liquids [11, 21]. Another key difference is the importance of thermal fluctuations at molecular scales. These are known to have a dramatic effect on the dynamics of drop pinch-off [25, 26], and it would be interesting to further explore their influence on spreading in the molecular simulations.

Finally, although wettability does not affect the initial rapid inertial flow in drop spreading, other cases are known to be strongly influenced by surface properties [13, 15, 27]. From a more general perspective, the combination of such inertial flows with a three-phase contact line therefore remains a challenge.

References

[1] H. Wijshoff, “The dynamics of the piezo inkjet printhead operation”, Physics Reports **491**, 77–177 (2010).

[2] P. Simpkins and V. Kuck, “On air entrainment in coatings”, J. Coll. Int. Sci. **263** (2003).

[3] D. Bonn, J. Eggers, J. Indekeu, J. Meunier, and E. Rolley, "Wetting and spreading", Rev. Mod. Phys. **81**, 739–805 (2009).

[4] V. Bergeron, D. Bonn, J. Y. Martin, and L. Vovelle, "Controlling droplet deposition with polymer additives", Nature **405** (2000).

[5] P. G. de Gennes, "Wetting: statics and dynamics", Rev. Mod. Phys. **57**, 827–863 (1985).

[6] L. Tanner, "The spreading of silicone oil drops on horizontal surfaces", J. Phys. D: Appl. Phys. **12**, 1–14 (1979).

[7] S. Rafaï, D. Sarker, V. Bergeron, J. Meunier, and D. Bonn, "Superspreading: Aqueous surfactant drops spreading on hydrophobic surfaces", Langmuir **18**, 10486–10488 (2002).

[8] A.-L. Biance, C. Clanet, and D. Quéré, "First steps in the spreading of a liquid droplet", Phys. Rev. E **69**, 016301 (2004).

[9] J. C. Bird, S. Mandre, and H. A. Stone, "Short-time dynamics of partial wetting", Phys. Rev. Lett. **100**, 234501 (2008).

[10] L. Courbin, J. C. Bird, M. Reyssat, and H. A. Stone, "Dynamics of wetting: from inertial spreading to viscous imbibition", J. Phys.: Condens. Matter **21**, 464127 (2009).

[11] A. Carlson, G. Bellani, and G. Amberg, "Universality in dynamic wetting dominated by contact-line friction", Phys. Rev. E **85**, 045302 (2012).

[12] A. Carlson, M. Do-Quang, and G. Amberg, "Dissipation in rapid dynamic wetting", J. Fluid Mech. **682**, 213–240 (2011).

[13] C. Duez, C. Ybert, C. Clanet, and L. Bocquet, "Making a splash with water repellency", Nat. Phys. **3**, 180 – 183 (2007).

[14] J. Eggers, "Fluid dynamics: Coupling the large and the small", Nat. Phys. **3**, 145–146 (2007).

[15] C. Duez, C. Ybert, C. Clanet, and L. Bocquet, "Wetting controls separation of inertial flows from solid surfaces", Phys. Rev. Lett. **104**, 084503 (2010).

[16] J. Eggers, J. R. Lister, and H. A. Stone, "Coalescence of liquid drops", J. Fluid Mech. **401**, 293–310 (1999).

[17] L. Duchemin, J. Eggers, and C. Josserand, "Inviscid coalescence of drops", J. Fluid Mech. **487**, 167 (2003).

[18] M. Wu, T. Cubaud, and C.-M. Ho, "Scaling law in liquid drop coalescence driven by surface tension", Phys. Fluids **16**, L51–L54 (2004).

[19] S. T. Thoroddsen, K. Takehara, and T. G. Etoh, "The coalescence speed of a pendent and a sessile drop", Journal of Fluid Mechanics **527**, 85–114 (2005).

[20] S. C. Case and S. R. Nagel, "Coalescence in low-viscosity liquids", Phys. Rev. Lett. **100**, 084503 (2008).

[21] J. D. Paulsen, J. C. Burton, and S. R. Nagel, "Viscous to inertial crossover in liquid drop coalescence", Phys. Rev. Lett. **106**, 114501 (2011).

[22] J. H. Weijs, A. Marchand, B. Andreotti, D. Lohse, and J. H. Snoeijer, "Origin of line tension for a lennard-jones nanodroplet", Phys. Fluids **23**, 1–12 (2011).

[23] J. C. Burton and P. Taborek, "Role of dimensionality and axisymmetry in fluid pinch-off and coalescence", Phys. Rev. Lett. **98**, 224502 (2007).

[24] D. V. der Spoel, E. Lindahl, B. Hess, G. Groenhof, A. Mark, and H. Berendsen, "Gromacs: Fast, flexible, and free", J. Comput. Chem. **26**, 17011718 (2005).

[25] M. Moseler and U. Landman, "Formation, stability, and breakup of nanojets", Science **289**, 1165–1169 (2000).

[26] J. Eggers, "Dynamics of liquid nanojets", Phys. Rev. Lett. **89**, 084502 (2002).

[27] P. Tsai, R. C. A. van der Veen, M. van de Raa, and D. Lohse, "How micropatterns and air pressure affect splashing on surfaces", Langmuir **26**, 16090 (2010).

7

Short time dynamics of viscous drop spreading *

Liquid drops start spreading directly after coming into contact with a solid substrate. Although this phenomenon involves a three-phase contact line, the spreading motion can be very fast. We experimentally study the initial spreading dynamics, characterized by the radius of the wetted area, for viscous drops. Using high-speed imaging with synchronized bottom and side views gives access to 6 decades of time resolution. We show that short time spreading does not exhibit a pure power-law growth. Instead, we find a spreading velocity that decreases logarithmically in time, with a dynamics identical to that of coalescing viscous drops. Remarkably, the contact line dissipation and wetting effects turn out to be unimportant during the initial stages of drop spreading.

7.1 Introduction

Liquid drops start spreading directly after coming into contact with a solid substrate. This process is relevant for many applications, from printing and coating to agriculture [1–5]. More precisely, we will consider here a drop of initial radius R that is

*A. Eddi, K.G. Winkels, and J.H. Snoeijer, "Short time dynamics of viscous drop spreading" (accepted for publication in *Physics of Fluids*).

gently brought into contact with a flat substrate (see fig. 7.1). The liquid has a surface tension γ, a viscosity η and a density ρ, while the interaction with the substrate is characterized by the equilibrium contact angle θ_{eq}. During spreading, the contact line moves radially outwards from the contact point and the drop wets a circular area of radius, $r(t)$. For the late times of spreading, the drop assumes the shape of a spherical cap (see fig. 7.1(b)). The dynamics is governed by viscous effects near the contact line and characterized by an apparent (dynamic) contact angle. When the substrate is completely wetting, this is described by the so-called Tanner's law [6–8]

$$\frac{r}{R} \sim \left(\frac{\gamma t}{\eta R}\right)^{1/10} . \tag{7.1}$$

It is well-known that the flow near the moving contact line is singular, since the viscous stresses diverge in a liquid wedge with a no-slip boundary condition [9]. This singularity can be regularized by introduction of a cut-off length at molecular scales to avoid the divergence. Once regularized, the visco-capillary balance near the contact line gives rise to the Cox-Voinov law for the apparent contact angle [10, 11]. Combined with the spherical cap geometry of the drop, one naturally obtains Eq. (7.1). While Tanner's law predicts the late time behavior of spreading for viscous drops, it does not apply at short times. In that case the geometry of the drop is completely different (fig. 7.1(a)). Just after contact, the drop shape is highly curved close to the contact point, with a meniscus characterized by a small length ζ as indicated in the sketch. This strongly curved meniscus generates a rapid flow inside the drop. In fact, the initial contact represents a singularity in itself: the meniscus size $\zeta \to 0$ as $r \to 0$, inducing diverging capillary stresses.

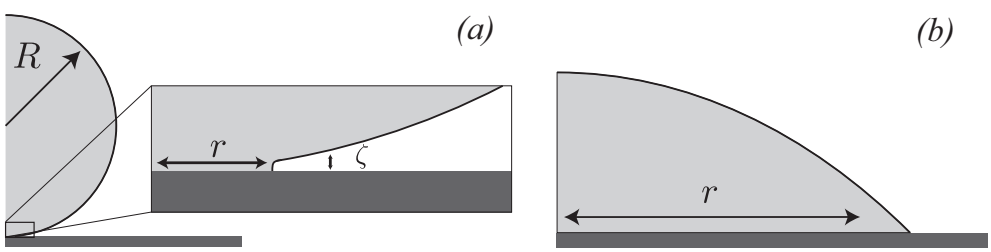

Figure 7.1: (a) Schematics presenting the geometry of a drop with initial radius R during the initial stages of spreading. The width of the narrow gap ζ determines the local curvature and thus the driving force. It depends on the radius of the wetted area r. (b) Schematics showing the geometry of the drop during the late stages of spreading.

Interestingly, the geometry in fig. 7.1(a) is strongly reminiscent to the coales-

cence of two spherical drops, if we consider the substrate to act as a mirror-plane for the flow. This analogy was first employed by Biance et al. [12], who compared the spreading to the well-studied growth of the neck when two identical drops coalesce [13–17]. This approach has proven very successful in the low-viscosity limit. The coalescence of water drops [13] shows the same dynamics as water drops spreading in total wetting conditions [12, 18–20]. In both cases it was found that $r \sim t^{1/2}$, with prefactors in agreement with potential flow calculations [21].

A natural question that arises is whether the spreading-coalescence analogy also holds for drops of high viscosity. In this limit, coalescence experiments [17] are in good agreement with predictions based on Stokes flow calculations [22–24]. The driving force depends on the radius of curvature ζ in the neck, and the speed u of the neck is given by [24]

$$u = \frac{dr}{dt} \simeq -\frac{1}{2\pi}\frac{\gamma}{\eta}\ln\frac{\zeta}{r} \ . \tag{7.2}$$

This result is essentially the Stokeslet solution in a two-dimensional flow, where the meniscus gap ζ provides the inner cutoff length for the point force. It was shown analytically that $\zeta \sim r^3/R^2$ when the surrounding fluid has no viscosity [23], while $\zeta \sim r^{3/2}/R^{1/2}$ when the outer fluid is viscous [24]. In the latter case, the radius of the neck in between the two drops is described asymptotically by

$$r \simeq -\frac{1}{4\pi}\frac{\gamma}{\eta}\, t\, \ln\frac{r}{R} \ . \tag{7.3}$$

Hence, the neck radius r grows linearly in time with logarithmic corrections. The same law is obtained when the outer fluid viscosity is negligible, the numerical prefactor being 4 times larger.

In this chapter we present an experimental investigation of viscous drop spreading on a substrate. In Sec. 7.2, we first introduce the experimental set-up that allows for an increased resolution both in time and space with respect to previous experiments. In Sec. 7.3, we discuss the qualitative and quantitative nature of this improvement. This is a crucial step in order to access a sufficient number of decades to reveal the initial spreading dynamics. Section 7.4 summarizes the experimental results obtained for water-glycerin mixtures. We investigate the influence of the initial drop radius R, the equilibrium contact angle θ_{eq}, and the viscosity η. Our key findings are that the viscous spreading dynamics is not a simple power-law of the type $r \sim t^{\alpha}$, and that the initial stages of spreading are independent of the substrate wettability. Instead, the spreading is consistent with the coalescence-prediction given in Eq. (7.3). In Sec. 7.5, we further discuss our findings in the light of this comparison between drop coalescence and drop spreading.

Mixture	η (mPa.s)	γ (mN.m^{-1})	ρ (kg.m^{-3})
Pure Glycerine	1120 ± 30	63.1 ± 0.2	1262 ± 5
Glycerine/Water – 90/10%	220 ± 5	63.4 ± 0.2	1238 ± 5
Glycerine/Water – 79/21%	50 ± 2	64.7 ± 0.2	1204 ± 5
Glycerine/Water – 60/40%	$11.5 \pm .5$	67.3 ± 0.2	1153 ± 5

Table 7.1: Properties of the different water-glycerine mixtures used in the experiment

7.2 Experimental set-up

The initial stages of drop spreading are investigated using the set-up shown in fig. 7.2. A drop of liquid is created at the tip of a needle and inflated quasi-statically. The needle is fixed at a distance D above a glass slide, so that the drop touches the substrate when it reaches a radius $R = D/2$. The fluid is injected using a syringe pump Picoplus (Harvard Apparatus, USA) set at a minimal outflux. We check that the approach speed at contact is lower than 10 μm.s^{-1}, eliminating any initial dynamics. We use water-glycerin mixtures in order to vary the viscosity of the liquid. The viscosity ranges from $\eta = 11.5$ to 1120 mPa.s. Surface tensions and contact angles are measured using a OCA 15PRO tensiometer (Dataphysics, Germany). Viscosity is measured using a Rheolab QC rheometer (Anton Parr, Austria) and density using a DMA 35 densimeter (Anton Parr, Austria). Physical properties of the various water-glycerine mixtures are summarized in table 7.1.

In most experiments, we use glass substrates that are completely wetted by the liquids. Microscope glass slides (Menzel, Germany) are cleaned using ethanol and acetone, then submerged in an ultrasonic bath for 15 mn and dried with filtered nitrogen gas. For partial wetting experiments, we coated glass substrates. The advancing contact angles for these substrates are presented in section 7.4.B.

We use two synchronized high-speed cameras to image the spreading dynamics of the drop (see fig. 7.2). An APX-RS camera coupled to a long-range microscope (Navitar 12X Zoom coupled with a 2X adapter tube) allows for a side view of the spreading drop (see fig. 7.2(b)). The spatial resolution is 3.5 μm/pixel, and the acquisition rate is 10 000 frames/s. A Photron SA1.1 camera coupled to an inverted microscope (Zeiss Axiovert 25, objective Zeiss A-plan 10 $\times$ magnification) records a bottom view of the wetted area (see fig. 7.2(c)). This allows for high speed recording

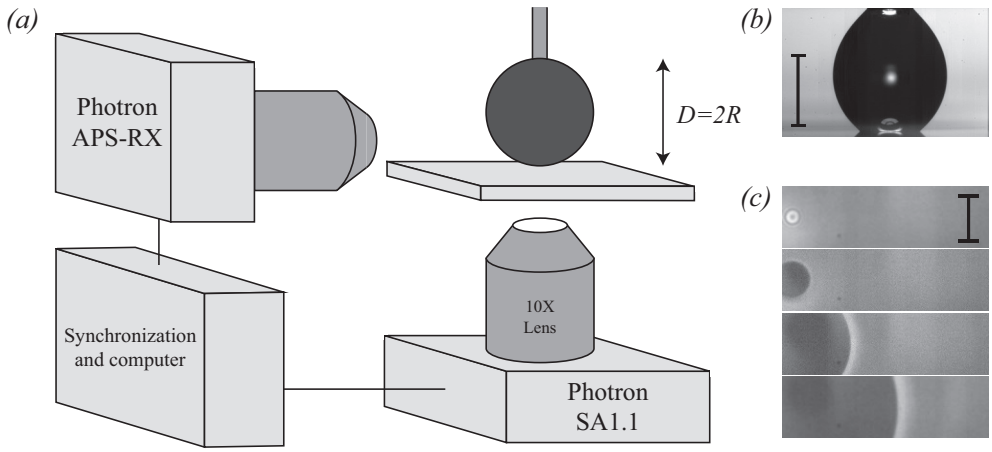

Figure 7.2: (a) Sketch of the experimental set-up. A drop of water-glycerine mixture attached to the tip of a needle is brought in contact with a glass substrate. Two high-speed cameras allow for synchronized bottom view and side view recordings. (b) Typical side view image of a spreading drop (the black bar indicates 1 mm). (c) Series of bottom view snapshots of a spreading drop, on the last frame before contact and at times $9 \cdot 10^{-5}$ s, $1.7 \cdot 10^{-4}$ s and $4.9 \cdot 10^{-4}$ s after contact (the black bar indicates 100 μm). Prior to contact, we observe an interference pattern at the location where the drop will touch the substrate. After contact, we observe the growth of a circular dark area corresponding to the wetted area on the glass substrate.

of the spreading, up to 250 000 frames/s, with a spatial resolution of 2 μm/pixel. Before contact, the drop is pendant a few microns above the glass surface, and we can observe circular fringes. After contact, we see a circular dark area (the wetted surface) growing with time. Contact occurs between the last frame where fringes can be seen and the first frame where the dark area appears. In order to minimize the error on the contact time, we set $t = 0$ half way between these two recorded frames.

The recorded images are processed using custom Matlab routines in which the position of the contact line of side and bottom view images is detected using a convolution procedure [25]. The contact line is located at the place were the intensity profile (in gray scale levels) presents its maximum slope. We repeated each experiments several times. Results turn out to be extremely reproducible and the main uncertainty at short times results from spatial resolution rather than from differences between successive experiments. The error bars given in the plots correspond to an uncertainty of 1 pixel in the detected radius.

In summary, this set-up gives access to 6 decades of time resolution, from a few

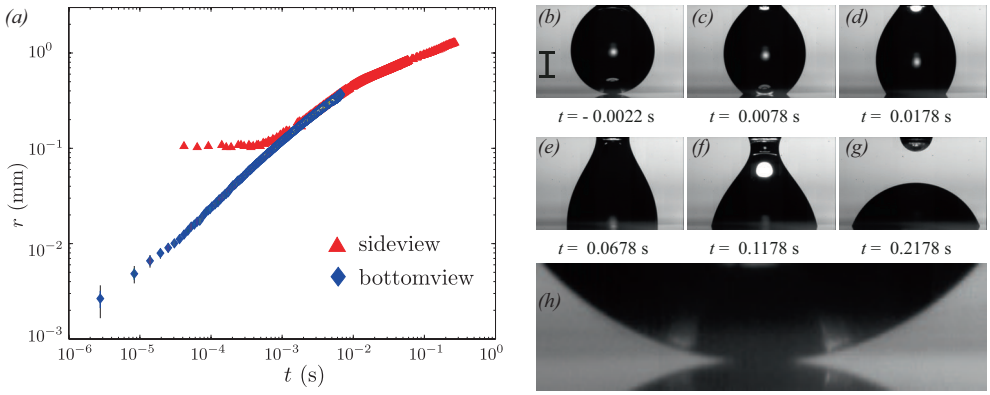

Figure 7.3: Evolution of the spreading radius r as a function of time. The radius is simultaneously determined from the bottom view (blue diamonds) and from the side view (red triangles). Both measurements agree at times larger than 10^{-3} s, but there is a large discrepancy at shorter times. The side view data present a horizontal plateau whereas the bottom view data suggest that r vanishes as $t \to 0$. (b-g) Series of side view snapshots of a spreading drop. The black bar represents 0.5 mm. (h) Magnified side view of the drop at the last frame before contact ($t = -0.0022$ s). The drop and its mirror image in the glass plate are already merged. This leads to a non-zero value of r before contact, and thus to an over-estimation of the contact radius at short times.

microseconds up to a few seconds, and 3 decades of space resolution, from a few microns up to a few millimeters.

7.3 Side view and bottom view

Most of the spreading experiments in which high speed imaging was used where done using only side view recordings [12, 18, 26–28]. We recently introduced a bottom view imaging that highly enhances the spatial resolution and thus significantly improves the temporal resolution of such experiments [20]. When looking at previous experimental studies based on side view measurements, all cases exhibit a plateau at short times corresponding to a non vanishing wetted radius at contact. Here, we would like to discuss the origin of this plateau.

Fig. 7.3 shows the radius r of the wetted area for a drop of water-glycerin mixture with viscosity $\eta = 220$ mPa.s. The blue squares indicate the bottom view and red triangles the synchronized side view. We see that, for times $t < 10^{-3}$ s, measurements disagree, so that the side view present the same plateau as in former studies, whereas

the bottom view suggests that r vanishes when $t \to 0$. It is only later, at times larger than 10^{-3} s that the two curves collapse.

The discrepancy can be understood as follows. Fig. 7.3b to 7.3g present a series of side view images extracted from this recording. It is important to note that the first image corresponds to a time before the actual contact between the drop and the substrate (determined from the bottom view). Fig. 7.3 (g) is a magnification of this image around the contact point. Even though there is no contact at that time (we still see fringes on the corresponding bottom view images), it looks as if the drop already touches the substrate. Due to the presence of a narrow gap and optical limitations, the drop image merges with its own optical reflexion on the glass substrate. This effect is enhanced by the circular shape of the drop: only a few pixels of merging in the vertical direction dramatically increases the measured radius r. All these reasons lead to an overestimation of r and thus to the observed plateau. It is only at later times, when the radius r becomes larger than a few hundreds of microns (being of the same order as the macroscopic radius of the drop) that this optical effect can be neglected and that the side view measurements give identical results as the bottom view. The bottom view does not suffer from this artifact: both $t = 0$ and r can be determined accurately. Hence, all our experimental results will be based upon bottom view measurements for radii $r < 300$ μm.

7.4 Experimental results

When the viscous drop spreads on the substrate, we can clearly distinguish two regimes in the spreading. Fig. 7.3(a) shows the radius of the wetted area as a function of time for a drop of initial radius $R = 0.5 \pm 0.02$ mm and viscosity $\eta = 220$ Pa.s. As expected from Tanner's law, the spreading is rather slow at late times ($t > 10^{-2}$s), with contact line speeds smaller than 1 mm.s^{-1} in the range of our experiments. By contrast, during the first stages the dynamics is much quicker, with a contact line speed measured up to ~ 0.5 m.s^{-1}. The cross over in between these two regimes occurs at time $t \simeq 10^{-3}$ s after contact, for a radius $r \simeq 0.4$ mm. These features (two regimes and a cross-over) can be observed in all our experiments. The precise time and radius at which the cross-over occurs depends on the experimental parameters, namely the droplet initial radius R, the liquid viscosity η and the surface wettability. In this section, we will systematically investigate the role of these parameters. In addition, the spatio-temporal resolution of our setup will enable us to characterize the spreading dynamics for the initial stages after contact.

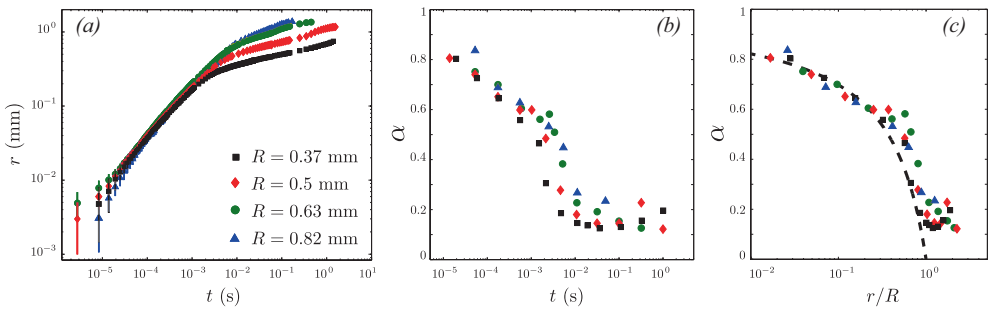

Figure 7.4: (a) Evolution of the radius r of the wetted area as a function of time t for drops with viscosity $\eta = 50$ mPa.s and initial radius $R = 0.37$ mm (Black squares), $R = 0.5$ mm (Red diamonds), $R = 0.63$ mm (Green circles) and $R = 0.82$ mm (Blue triangles). (b) Evolution of the apparent exponent $\alpha = \frac{d\ln r}{d\ln t}$ as a function of time for the same drops as in (a). (c) Evolution of α as a function of the adimensional radius r/R of the wetted area for the same drops as in (a). The dashed line is the prediction from Eq. (7.5).

7.4.1 Radius dependence

We will first look at the effect of the initial drop radius R for a given liquid viscosity. Figure 7.4(a) shows the evolution of the radius of the wetted area as a function of time for drops of viscosity $\eta = 50$ mPa.s for four different initial drop radii R. At short times, r follows quantitatively the same dynamics for all drop radii R, and all the curves collapse on each other. During this first regime of spreading, $r(t)$ does not seem to depend on the drop size. Around a cross-over time t_C and a cross-over radius r_C, each of the experimental curves undergoes a transition and present a sharp change to a slower dynamics. The values of t_C and r_C depend on the initial radius R: the cross-over occurs later for larger values of R.

A common approach to characterize the spreading dynamics is to look for a power-law dynamics, $r \sim t^{\alpha}$. To investigate whether our experiments indeed display power-law spreading regimes, we define the apparent exponent

$$\alpha = \frac{d\ln r}{d\ln t}\,, \tag{7.4}$$

and determine it from our experimental data by computing twice the value of α per decade of time. Figure 7.4(b) presents the evolution of α as a function of time t for four different values of the drop radius R. At short times, there is a fast dynamics with an apparent exponent $0.5 < \alpha < 1$.

Note that the values at early times are significantly larger than the slope 0.5 that was measured in recent experiments [28]. This difference can be explained from the improved spatio-temporal resolution of our bottom view setup, giving access to earlier dynamics. In all cases, α slowly decreases in the first regime and abruptly decreases at a time t_C. Later on, the apparent exponent reaches a plateau with a value $0.1 < \alpha < 0.2$, which is consistent with Tanner's law (Eq. (7.1)).

Interestingly, the early stage is not characterized by a single exponent α: the apparent exponent is slowly decreasing with time. We emphasize that the cross-over to Tanner's regime is much more abrupt than this slow decrease at early times. Hence, we infer that the slowly decreasing α is not simply a cross-over effect, but an intrinsic property of the initial spreading dynamics. This becomes even more apparent in fig. 7.4(c), where we plot α as a function of the dimensionless radius r/R. For all initial radii R, we observe a collapse of the curves. The sharp transition to Tanner's regime occurs for a dimensionless radius $r_c/R \simeq 0.8$. This value of r_c/R can be understood from the geometry of the spreading drop (see fig. 7.1). At short times, the wetted area is located under a nearly spherical drop whereas, at late times, we recover a spherical cap of liquid that slowly spreads. The cross-over in-between these two geometrical configurations occurs when the radius of the wetted area is of the same order as the initial drop radius R, in good agreement with the observed value $r_c/R \sim 1$.

Let us now compare the short-time dynamics with the prediction provided by viscous drop coalescence [24]. Equation (7.3) is not a pure power-law, since it displays a logarithmic correction. Applying the definition Eq. (7.4), the effective exponent for coalescence can be derived as

$$\alpha = \frac{\ln \frac{r}{R}}{\ln \frac{r}{R} - 1}. \tag{7.5}$$

The dashed line in fig. 7.4(c) shows this prediction, which is in quantitative agreement with the experimental observations at early times. In particular, it captures the slow decrease of the exponent. This is a first indication that the initial dynamics of viscous drop spreading is similar to the coalescence of spherical drops.

7.4.2 Wettability dependence

In order to check the wettability dependence of spreading, we performed experiments on three other substrates presenting various equilibrium contact angles θ_{eq}. We used untreated glass that gives $\theta_{eq} \simeq 30^\circ$. The two other substrates are glass slides covered by fluorinated coatings that increase the hydrophobicity of the substrate, limiting the spreading of the drop and imposing a finite equilibrium radius. The first one gives $\theta_{eq} \simeq 85^\circ$, and the second one (Novec 1700, 3M) leads to $\theta_{eq} \simeq 105^\circ$. Fig. 7.5 presents r as a function of time for these four different substrate wettabilities. All

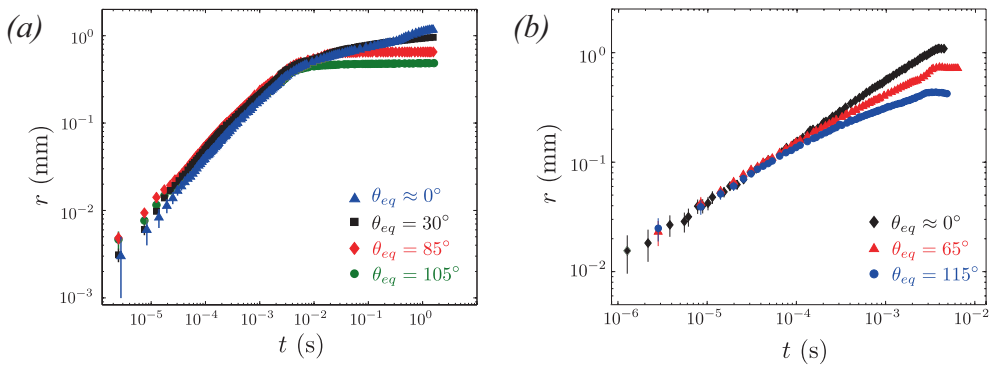

Figure 7.5: (a) Evolution of r as a function of t for droplets with viscosity $\eta =$ 50 mPa.s and initial radius $R = 0.5$ mm for 4 different substrates. Blue triangles: cleaned glass ($\theta_{eq} \simeq 0°$), black squares: raw glass ($\theta_{eq} = 30°$), red diamonds: fluorinated coating ($\theta_{eq} = 85°$) and green circles: 3M coating ($\theta_{eq} = 105°$). The initial dynamics is identical for all θ_{eq} within experimental error. (b) Evolution of r as a function of time for pure water drops and 3 different substrates with equilibrium contact angles $\theta_{eq} = 3°, 65°$ and $115°$ [20].

the curves follow the same dynamics in the first regime, subsequently the spreading slows down and eventually stops when the drop reaches its equilibrium shape. The wettability has indeed almost no effect on the first regime, and it is only later that a deviation can be observed.

These observations are consistent with the hypothesis that the initial spreading dynamics is similar to coalescence: the independence of wettability suggests that the solid wall is unimportant at the initial stages. Let us emphasize that the same conclusion was previously drawn for the case of pure water, which have a much lower viscosity [12, 20]. The spreading experiments for water are reported in fig. 7.5(b). For three different wettabilities, the spreading dynamics is identical at short times [20]. In this case, the dynamics is characterized by a well-defined exponent $\alpha = 1/2$. This agrees with the law for inertially dominated coalescence that predicts

$$\frac{r}{R} = D_0 \left(\frac{t}{\sqrt{(\rho R^3/\gamma)}} \right)^{\frac{1}{2}} . \tag{7.6}$$

The value of the prefactor $D_0 = 1.14$ has been determined experimentally [13]. For water drops spreading on a substrate [20], $D_0 = 1.2 \pm 0.1$, in excellent agreement with the coalescence case.

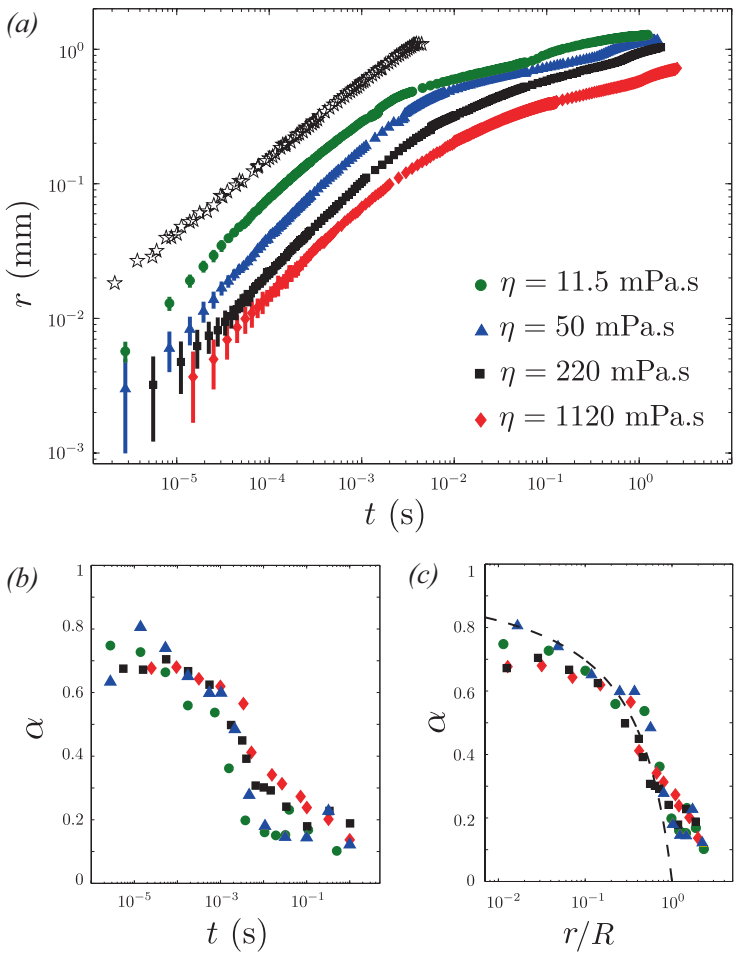

Figure 7.6: (a) Evolution of the radius r of the wetted area as a function of time t for drops in complete wetting with initial radius $R = 0.5$ mm with viscosity $\eta =$ 11.5 mPa.s (Green circles), $\eta = 50$ mPa.s (Blue triangles), $\eta = 220$ mPa.s (Black squares) and $\eta = 1120$ mPa.s (Red diamonds). The open stars are data obtained for pure water [20]. (b) Evolution of the measured apparent exponent α as a function of the time for the same data as in (a). (c) Evolution of α as a function of r/R for the same data as in (a). The dashed line is the prediction from Eq. (7.5).

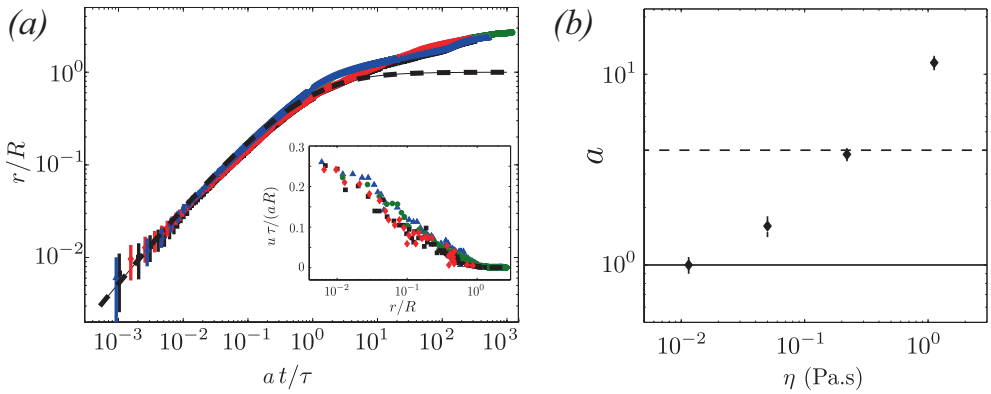

Figure 7.7: (a) Dimensionless radius r/R as a function of dimensionless time at/τ, with $\tau = 4\pi\eta R/\gamma$ for data from fig. 7.6. The dashed line is the theoretical prediction from Eq. (7.3). Inset: dimensionless contact line speed $u\tau/(aR)$ as a function of the adimensionnal radius r/R. The collapse agree with the logarithmic decay prediction by Eq. (7.2). (b) Values of the fitted prefactor a for different liquid viscosities η.

7.4.3 Viscosity dependence

We now investigate how viscosity affects the spreading dynamics. Fig. 7.6(a) shows the evolution of $r(t)$ for drops with initial radius $R = 0.5$ mm and five different viscosities. The closed symbols are experiments for water-glycerine mixtures, while for completeness we also report the inertia-dominated case of pure water (open symbols) [20]). For the viscous drops, all curves again exhibit the same qualitative behavior, characterized by two regimes. As expected, the dynamics is much slower for the drops of higher viscosity. Once more, there is no clear spreading exponent at early times. This can be seen from fig. 7.6(b) showing the evolution of α as a function of time t. The apparent exponent slowly decreases during the first regime, and reaches a plateau around $\alpha \simeq 0.15$. The time for the cross-over depends on the viscosity. The cross-over appears at earlier times and is sharper for lower viscosities. However, this effect of viscosity can be eliminated when plotting α as a function of the dimensionless radius r/R (fig. 7.6(c)). We observe a collapse of the data onto the a master curve, again in quantitative agreement with the prediction from Eq. (7.5). This strongly suggests that the dynamics of viscous drop spreading depends on the geometry (given by the dimensionless radius r/R) at short times, in a manner consistent with the coalescence of viscous drops.

Finally, based on the prediction Eq. (7.3), we scale the data to the form

$$\frac{r}{R} = -a\frac{t}{\tau}\ln\frac{r}{R}, \quad \text{with} \quad \tau = \frac{4\pi\eta R}{\gamma}, \tag{7.7}$$

where a is used as an adjustable parameter. In coalescence of spherical drops, the parameter $a = 4$ in the case where the gas viscosity can be neglected, while it is predicted that $a = 1$ for the case of non-neglible gas viscosity [24]. Figure 7.7(a) reveals that an excellent collapse to this form can be achieved for the initial spreading. The prefactors a for the various viscosities are reported in Figure 7.7(b). Interestingly, the value of a is not universal, but increases significantly with η. Qualitatively, this is similar to viscous coalescence, for which a is expected to increase for increasing liquid viscosity. However, the effect is stronger than expected from coalescence theory, which predicts that a should remain within the boundaries from 1 to 4.

Finally, it should be noted that Eq. (7.3) relies on the fact that the spreading speed $u = dr/dt$ is imposed by the Stokeslet solution [24], and is of the form

$$u = -\frac{aR}{\tau}\ln\frac{r}{R}. \tag{7.8}$$

Hence, the spreading velocity should decrease logarithmically as r/R increases. We indeed find such a decrease in spreading velocity, as can be seen from the inset on fig. 7.7(a). The collapse was obtained with the same values of the fitting parameter a. Let us note that the dynamics of Eqs. (7.3) and (7.8) are equivalent only asymptotically, and that for finite ratio r/R there are small (logarithmic) differences. In practice, this leads to 30% underestimation of the velocities with respect to Eq. (7.8).

7.5 Discussion

The initial spreading of low-viscosity drops exhibits a well-defined exponent $r \sim t^{1/2}$ over several decades [12, 20]. In this case, the spreading was found identical to that of the dynamics of coalescence of two low-viscosity drops [13], which exhibits the same exponent and the same prefactor. In this chapter we have shown that for viscous drops spreading on a substrate, the evolution of the wetted area is not characterized by a simple power-law growth, as was recently proposed [28]. During the initial spreading stages, the apparent exponent $\alpha = d\ln r/d\ln t$ is observed to slowly decrease from about 0.8 to 0.5. Once more, it turned out fruitful to compare the spreading dynamics to the coalescence of viscous drops. Namely, the coalescence is characterized by a slowly decreasing velocity [23], and such a dynamics agrees quantitively with all our spreading experiments. The analogy with coalescence of freely suspended

drops suggests that the presence of the wall has no significant influence on the flow. This picture is confirmed by our observation that the initial spreading is completely independent of the wettability of the substrate. This is particularly surprising since the flow develops singular viscous stresses near the contact line [9]. It thus appears that the singularity due to the initial contact, when the spherical drop first touches the flat substrate, completely dominates over the contact line singularity. It is only later, when the drop enters in Tanner's regime, that the contact line dissipation controls the spreading dynamics.

While the data for different viscosities can be collapsed onto the form predicted for coalescence (see fig. 7.7(a)), the typical spreading velocity does not simply scale as $\sim 1/\eta$. This can be seen from the prefactor a, which still displays a dependence on viscosity η (see fig. 7.7(b)). A similar observation was made recently by Carlson et al. [28]. They noticed that the spreading data cannot be collapsed using a simple viscous scaling, and introduced additional friction at the contact line to explain this result. Here we suggest that such a dependence can (at least partly) be explained from the influence of the outer fluid. The effect of the gas was previously taken into account for the coalescence problem [24], indeed giving rise to non-universal values of the prefactor a. However, the values of a necessary to fit our data explore a wider range than predicted for coalescence – in particular in the large viscosity regime where the outer fluid should be negligible. We nevertheless find prefactors that are comparable to other coalescence experiments [17], so that experimentally the "spreading–coalescence" analogy might still be fully quantitative. Interestingly, the strong influence of the gas was also emphasized for air entrainment by advancing contact lines [29]. In that case the speed dependence on liquid viscosity was found much weaker than $1/\eta$, in a way comparable to the present experiments. Similarly, impact experiments were collapsed using a $1/\sqrt{\eta}$ speed-dependence [30]. It thus seems that the confinement of the air near the contact line has a major effect, but the details have remained unresolved.

The key open question is why the spreading–coalescence analogy provides such an accurate description of the experiment. Even though the flow during the coalescence of two spherical drops exhibits a mirror-plane, there is still a substantial flow along this plane of symmetry. For spreading, this plane coincides with the wall and one would have expected that the no-slip condition strongly impedes the motion of the contact line. A possible interpretation could be that slip is enhanced due to the singular geometry of the initial contact.

References

[1] H. Wijshoff, *The dynamics of the piezo inkjet printhead operation*, Physics Reports **491**, 77 (2010).

[2] P. Simpkins and V. Kuck, *On air entrainment in coatings*, J. Coll. Int. Sci. **263**, (2003).

[3] D. Bonn, J. Eggers, J. Indekeu, J. Meunier, and E. Rolley, *Wetting and spreading*, Rev. Mod. Phys. **81**, 739 (2009).

[4] V. Bergeron, D. Bonn, J. Y. Martin, and L. Vovelle, *Controlling droplet deposition with polymer additives*, Nature **405**, (2000).

[5] P. G. de Gennes, *Wetting: statics and dynamics*, Rev. Mod. Phys. **57**, 827 (1985).

[6] L. Tanner, *The spreading of silicone oil drops on horizontal surfaces*, J. Phys. D: Appl. Phys. **12**, 1 (1979).

[7] P. G. de Gennes, F. Brochard-Wyart, and D. Quere, *Capillarity and Wetting Phenomena: Drops, Bubbles, Pearls, Waves* (Springer, New York, ADDRESS, 2003).

[8] S. Rafaï, D. Sarker, V. Bergeron, J. Meunier, and D. Bonn, *Superspreading: aqueous Surfactant Drops Spreading on Hydrophobic Surfaces*, Langmuir **18**, 10486 (2002).

[9] C. Huh and L. E. Scriven, *Hydrodynamic model of steady movement of a solid/liquid/fluid contact line*, J. Coll. Int. Sci. **35**, 85 (1971).

[10] O. V. Voinov, *Hydrodynamics of wetting*, Fluid Dyn. **11**, 714 (1976).

[11] R. G. Cox, *The dynamics of the spreading of liquids on a solid surface*, J. Fluid Mech. **168**, 169 (1986).

[12] A.-L. Biance, C. Clanet, and D. Quéré, *First steps in the spreading of a liquid droplet*, Phys. Rev. E **69**, 016301 (2004).

[13] D. G. A. L. Aarts, H. N. W. Lekkerkerker, H. Guo, G. H. Wegdam, and D. Bonn, *Hydrodynamics of Droplet Coalescence*, Phys. Rev. Lett. **95**, 164503 (2005).

[14] M. Wu, T. Cubaud, and C.-M. Ho, *Scaling law in liquid drop coalescence driven by surface tension*, Phys. Fluids **16**, L51 (2004).

[15] S. T. Thoroddsen, K. Takehara, and T. G. Etoh, *The coalescence speed of a pendent and a sessile drop*, J. Fluid Mech. **527**, 85 (2005).

[16] S. C. Case and S. R. Nagel, *Coalescence in Low-Viscosity Liquids*, Phys. Rev. Lett. **100**, 084503 (2008).

[17] J. D. Paulsen, J. C. Burton, and S. R. Nagel, *Viscous to Inertial Crossover in Liquid Drop Coalescence*, Phys. Rev. Lett. **106**, 114501 (2011).

[18] J. C. Bird, S. Mandre, and H. A. Stone, *Short-Time Dynamics of Partial Wetting*, Phys. Rev. Lett. **100**, 234501 (2008).

[19] L. Courbin, J. C. Bird, M. Reyssat, and H. A. Stone, *Dynamics of wetting: from inertial spreading to viscous imbibition*, J. Phys.: Condens. Matter **21**, 464127 (2009).

[20] K. G. Winkels, J. H. Weijs, A. Eddi, and J. H. Snoeijer, *Initial spreading of low-viscosity drops on partially wetting surfaces*, Phys. Rev. E **85**, 055301 (R) (2012).

[21] L. Duchemin, J. Eggers, and C. Josserand, *Inviscid coalescence of drops*, J. Fluid Mech. **487**, 167 (2003).

[22] R. Hopper, *Plane Stokes flow driven by capillarity on a free surface.*, J. Fluid Mech. **213**, 349 (1990).

[23] R. Hopper, *Coalescence of two viscous cylinders by capillarity: Part I. Theory.*, J. Am. Ceram. Soc. **76**, 2947 (1993).

[24] J. Eggers, J. R. Lister, and H. A. Stone, *Coalescence of liquid drops*, J. Fluid Mech. **401**, 293 (1999).

[25] A. Marchand, Ph.D. thesis, University Paris Diderot, 2011.

[26] L. Chen, G. K. Auerhammer, and E. Bonaccurso, *Short time wetting dynamics on soft surfaces*, Soft Matter **7**, 9084 (2011).

[27] A. Carlson, M. Do-Quang, and G. Amberg, *Dissipation in rapid dynamic wetting*, J. Fluid Mech. **682**, 213 (2011).

[28] A. Carlson, G. Bellani, and G. Amberg, *Universality in dynamic wetting dominated by contact line friction*, Phys. Rev. E **85**, 045302 (R) (2012).

[29] A. Marchand, T. Chan, J. H. Snoeijer, and B. Andreotti, *Air entrainment by contact lines of a solid plate plunged into a viscous fluid.*, Phys. Rev. Lett. **108**, 204501 (2012).

[30] J. de Ruiter, J. M. Oh, D. van den Ende, and F. Mugele, *Dynamics of Collapse of Air Films in Drop Impact*, Phys. Rev. Lett. **108**, 074505 (2012).

8

Levitated drops on an air cushion *

The levitation of drops on an air cushion is studied experimentally by high speed imaging. Using a porous medium with a superhydrophobic top layer, drops of two different viscosities are levitated by a prescribed air flow. By varying the air flow velocity and drop size, the excitation threshold for the formation of drop oscillations is studied, which for water results in star-drops. Our experiments show that the phenomenon of star oscillations does not require any thermal effects, as previously thought from Leidenfrost drops. It is observed that for increasing flow rate the threshold drop size reduces. We find a weak dependence of the threshold on the liquid viscosity. By contrast, the oscillatory dynamics is markedly different for the two viscosities: the viscous drops develop purely axi-symmetric modes, while the water drops display chaotic modes or modes similar to classical Leidenfrost stars.

8.1 Introduction

Drops of water can levitate above a very hot plate due to the so-called 'Leidenfrost' effect [1]. In this effect drops float on a thin layer of water vapor resulting from evaporation in between the hot substrate and the drop. The shape and dynamics of the vapor layer can be quite complex [2] and can be used to move liquid along a surface

*To be submitted as part of: W. Bouwhuis, K.G. Winkels, I. R. Peters, P. Brunet, D. van der Meer, and J. H. Snoeijer, *Oscillating and faceted star-shaped drops levitated by an airflow*.

with the help of unevenly textured substrates [3–5]. Under some conditions, such as large enough drop size or high enough temperature, drops spontaneously start to oscillate and develop 'star-shapes' or 'faceted shapes' [8–12]. Recently, it has been found that this phenomenon does not only occur in the case of Leidenfrost drops, but also for drops levitated on a steady uniform airflow at room temperature [6]. Figure 8.1 shows examples of star-drops obtained for water drops on a prescribed air flow, taken from [6]. The origin of the oscillatory instability has remained unclear, but the striking similarities with the Leidenfrost stars suggest a common mechanism based only on hydrodynamics and free-surface dynamics, without invoking any thermal effects.

Drops with facetted shapes have been observed in various different systems with a periodic forcing frequency close to the eigenmodes of the drop. Such drop shapes arise for drops sitting on vertically vibrated hydrophobic substrates [20, 21], acoustically levitated drops with low-frequency modulated pressure [22], liquid metal drops subjected to an oscillating magnetic field [23], or drops on a pulsating air cushion [24, 25]. Using simple arguments [26], the appearance of these stars can be explained by the temporal modulation of the eigen frequency of the drop, due to the external forcing, thus inducing a parametric forcing. Rayleigh and Lamb [15] already predicted that for small enough deformations and for inviscid spherical drops, the resonance frequencies of spherical drops are equal to:

$$f_n = \frac{1}{2\pi}\left(\frac{n(n-1)(n+2)\gamma}{\rho_l R^3}\right)^{1/2} \tag{8.1}$$

where f_n stands for the resonance frequency of the n^{th} mode of oscillation, R is the radius, γ and ρ_l are the liquid surface tension and density. When the drop shape is different from the ideal spherical case, the resonance frequencies are modified with much more complex expressions, but in the case of a liquid puddle of radius R much larger than the averaged drop height H_d, the eigenfrequencies take the following simple expression [26] :

$$f_n = \frac{1}{2\pi}\left(\frac{n(n^2-1)\gamma}{\rho_l R^3}\right)^{\frac{1}{2}}, \tag{8.2}$$

where n is now the number of waves on the drop. Note that in practice, the frequencies predicted by eq. 8.1 and 8.2 are very similar. Thus it becomes clear that a parametric instability should occur when the drop radius is modulated periodically in time. The same happens when due to a periodic external forcing, the drop stands in a time-periodic acceleration field. In that case the height of the cylindrical liquid puddle H_d also varies periodically, as for a non-wetting condition (contact-angle being close to 180°) this height is simply equal to twice the effective capillary length

$\ell_c = \sqrt{\frac{\gamma}{\rho_l a}}$, a being the instantaneous acceleration (without forcing, a is equal to the gravity constant g). By volume conservation, a time dependence of H_d results into an oscillation of the radius R. Assuming small deformations, R will have the same time-periodicity as the external forcing. Then, the occurrence of star shaped oscillations by parametric forcing often have a frequency equal to half of the driving (vertical oscillation) frequency [26].

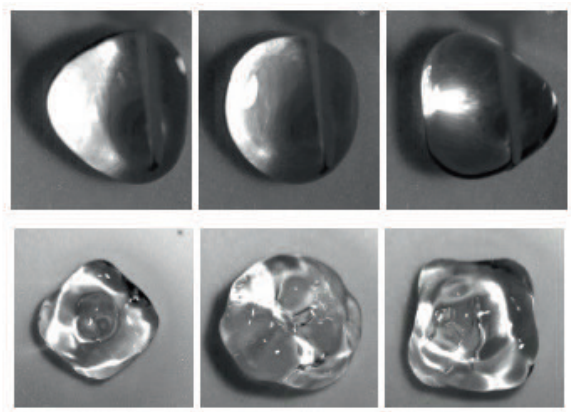

Figure 8.1: Star drops levitated by a non-pulsed airflow. Top: mode n=3; bottom: mode n=4. Figure from Ref. [6].

In the case of non-pulsed air cushion or Leidenfrost levitation, the key open question is to identify the origin of the oscillations: What are the mechanisms that induce a time-periodic instability which in turn give rise to vertical oscillations of the drop center-of-mass and shape? Recent experiments of star drops levitated on a non-pulsed air cushion (Fig. 8.1) suggest that these star-drops do not result from a temperature gradient-induced instability, contrary to what was previously hypothesised [14]. Once the origin of this instability is explained, the appearance of star drops is quite obvious.

Apart from the oscillatory instability, a levitated drop can develop a “chimney”, for which an air bubble develops below the drop and pierces through the drop [19]. This phenomenon has been explained theoretically and reproduced numerically in the case of highly viscous drops [7, 18]. Interestingly the numerics for viscous drops did not display any oscillatory instability. This is reminiscent of the suppression of Faraday waves, for increased viscosity. The role of viscosity for levitated drops is yet not addressed, while it has been pointed out to be detrimental for several applications like molten glass manufacturing [18].

In this research we will study the instability of levitated drops on a prescribed airflow. We will determine the threshold for levitated drop instability, and show how this depends on drop size, flow rate and liquid viscosity. To answer these questions, two types of liquids are used: water (low viscosity) and water-glycerine mixture (high viscosity). The Chapter is organized as follows, first the setup, measurement method and measurement procedure are explained in section 8.2. Then the results, typical image sequences and measured dynamics, for low-viscosity drops (water) are shown in subsection 8.3.1. In subsection 8.3.1, a similar characterisation is applied for the higher viscosity drops (water-glycerine mixture). In the last section (8.4), the main experimental results will be compared and discussed. We will show that there is a weak dependence of the instability behaviour on viscosity, while there is a strong difference in the resulting dynamics.

8.2 Experimental setup

It is well known that in case of Leidenfrost drops, the drops are levitated by a vapor layer. The vapor, coming directly from the drop, generates a cushioning layer for levitation due to the build up of a lubrication pressure between the lower part of the drop and the substrate. Hence, the cushioning layer results from temperature effects that could give rise to strong surface tension gradients. To avoid temperature effects and directly control the layer gas flux, another experimental method was introduced in Ref. [6]. In this experimental method, which will also be used in this Chapter, the air cushion is created by an ascending compressed airflow (Fig. 8.2). The airflow is forced through a porous glass medium (Duran Group, Filter Funel, porosity 3, inner diameter 56 mm) that is covered by a coarse grid. The grid is made superhydrophobic (electroless galvanic deposited metal [27]) to avoid imbibition of the hydrophilic porous medium. The large pressure load on the porous medium creates an approximately homogeneous outflow, which is assumed to be hardly affected by the small pressure load of the drop. Consequently, if the airflow Q is large enough, a lubricating layer (air cushion) can emerge and support the complete weight of the drop. There exists a threshold drop size R and gas flow rate Q at which the drops become unstable and start to oscillate, i.e. the instability threshold. The airflow is controlled with an Aalborg flow meter (range: 0 - 60 l/min). Since the drop is very mobile in the levitated state, it is necessary to hold it by a needle. This fixates the drop at a constant location on the substrate, but it should be noted that the presence of the needle might affect the drop dynamics. The same needle is used to supply and subtract liquid from the drop via a syringe. To study the drop behavior for various flow rates Q and drop sizes R, the drop motions are recorded from top view, with a

high speed camera at 1000 fps (Phantom V9). Using a macro lens (Nikon Aspherical Macro, 1:2) with extension tubes, a resolution of 42 μm/pixel is obtained (see Fig. 8.2). Reflective illumination (IDT, LED lightsource) is realised via a 45 degrees tilted beam splitter.

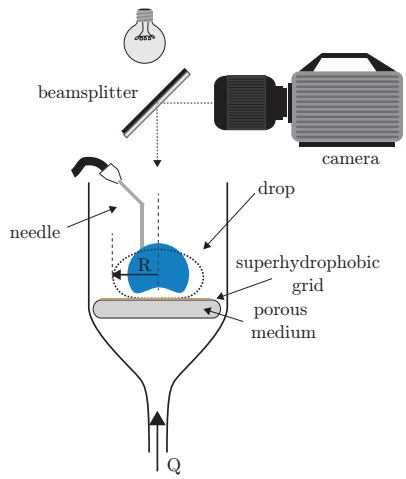

Figure 8.2: Sketch of the experimental setup. Illumination and camera view are obtained using a beamsplitter. A flow rate Q is prescribed through a porous medium. Since the levitated drop is very mobile, it is held in position by the liquid supply needle.

The aim of this work is to study the instability threshold (appearance of drop oscillations) for levitated drops. To verify reproducibility of the experiment, each measurement is repeated multiple times and by the following two different procedures. In the first method, each measurement starts with a new constant flow rate $Q = Q_t$ and a small drop size R. Then the drop is gradually expanded in size, by slowly increasing the drop volume. This continues and the drop reaches a floating state ($R < R_t$) which finally becomes unstable once the drop size equals the threshold size R_t for flow rate Q_t. The volume increase of the drop is directly stopped and subsequently, the dynamics of the unstable drop at the threshold value is recorded with the camera. Note, that the threshold for levitation and the appearance of oscillations is very close. A second method to determine the instability threshold is measurement of Q_c, obtained after the first method. For a drop with fixed drop size R_t, starting in unstable state $Q = Q_t$, the air flow is slowly reduced to a value which results in a stable state: $Q = Q_c$. This second threshold Q_c turns out to be a bit smaller than Q_t. However, this difference is comparable to the accuracy of our experiments, so we

cannot make any definite statements on whether the instability is hysteric or results from practical subtleties, for example, sticking of the drop to the substrate. In what follows we therefore plot the mean threshold Q_m, obtained upon increasing the drop size and variation of the flow rate. Q_m is determined as: $(Q_t + Q_c)/2$. The error bar gives an indication of the difference between the two measurement procedures.

After measurement of Q_c the complete measurement for one drop is finished by further reducing the flow rate which finally results in a sessile drop state again. A snapshot is made at this zero flow rate (i.e. sessile drop Fig. 8.4a) and the drop size R is determined as the maximum radius of the sessile drop in top view. There exist local variations in the flow with position on the substrate. To reduce the influence of any possible airflow fluctuations coming from e.g. variations in the substrate or hydrophobic grid fixation, all data points are measured at a fixed position on the substrate. To study the influence of viscosity on the drop dynamics, two liquids are used: water (1 cP) and water-glycerine mixture ($\sim$ 60 cP). The resulting dynamics is characterised by liquid viscosity η, drop size R, flow rate Q and oscillation frequency f.

8.3 Observations

8.3.1 Low viscosity drops

In this section we will study the stability and dynamics of levitated water drops ($\eta_{low} = 1$ cP). Some of the results can be compared directly to the classical Leidenfrost drops, levitated above a hot substrate [19]. By varying the drop radius R and air flow rate Q, the threshold for drop oscillations (R_t,Q_m) is determined. Results for water are plotted in Fig. 8.3, as circles. The blue points are oscillations without detachment from the needle. In these cases, the size of the drop is measured in sessile state. While, the green points correspond to violent oscillations or a chimney, which led to detachment from the needle. The size is then approximated in the unstable levitated state. Clearly, the threshold drop size R decreases with flow rate. The smallest drops investigated here are stable up to very high flow rate, while the largest drops destabilize even at very small Q. A chimney was for example observed for the smallest flow rate and largest drop size $R \sim 9.6$mm (green circle in Fig. 8.3). This point is very close to the blue dashed line that indicates the onset of the chimney instability for water drops, as determined for thermal Leidenfrost drops by Biance et al. [19] ($R_c = 4.0\ell_c$, where ℓ_c is the capillary length). Interestingly such an instability was predicted to occur even at vanishing flow rate [7]. However constraints in the control of extreme small flow rates limited measurements at smaller Q.

For all levitated drops, a recording is taken of the oscillating motion at the thresh-

old flow rate Q_t. Typical images obtained in the experiments are shown in Fig. 8.4. Fig. 8.4a is a sessile water drop, with $Q = 0$, while panel (c-h) correspond to oscillating drops at non-zero flow rates. Once the water drops are unstable, the oscillations appear to be rather chaotic, i.e. a combination of modes (Fig. 8.4c). However, in few cases also one distinct mode was observed ranging from mode $n = 2$ to $n = 6$, as is shown in Fig. 8.4d-h. In case of these well-defined modes, the oscillation fre-

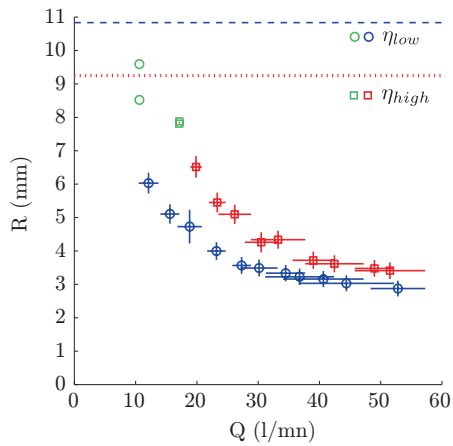

Figure 8.3: Measured instability threshold Q_m, for levitated drops. Data represents all data points for water- and water/glycerine drops, in circles (○ and ○) and squares (□ and □), respectively. Since for the smallest flow rate the drop size could not be measured (it detaches from the needle), R is measured in levitated state instead of sessile state. These points are therefore indicated with a different color (□ and ○). Note that point □, corresponds to the chimney instability from Fig. 8.6b. The theoretical prediction of the critical radius for chimney instability is indicated by the blue dashed line and red dotted line for the used water and water-glycerine mixture respectively.

quency can be determined and compared to the prediction of Eq. 8.1. The results are shown in figure 8.5. For mode $n = 3$, seven different drops are measured with $R = 3.2 - 6.1$ mm. Rescaling indeed collapses the data. Additionally the order of magnitude and trend are in quite good agreement with theory (red solid line) for all modes, i.e. rescaled frequency increases with mode number.

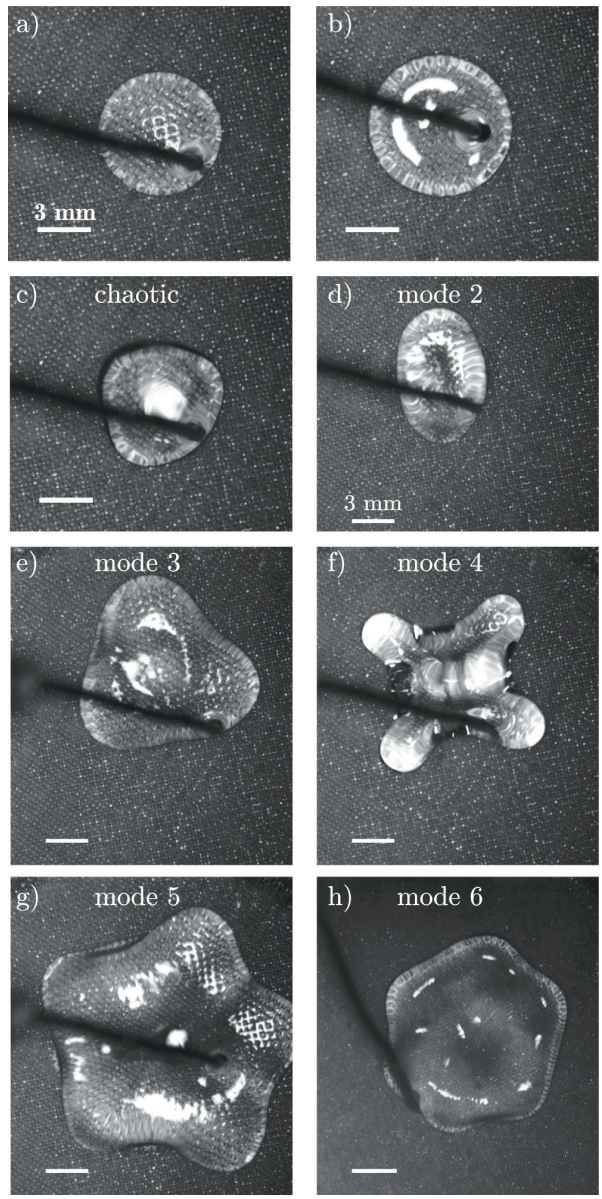

Figure 8.4: Examples of levitated drop instabilities. All images show water drops, except for (b) which is a water-glycerine drop. (a) Sessile water drop. (b) Levitating water-glycerine drop. (c) Chaotic mode water drop oscillation. (d) Water drop, mode $n = 2$ ($R = 4.1$ mm, $f = 13.8$ Hz). (e) Water drop, mode $n = 3$ ($R = 6.1$ mm, $f = 14.2$ Hz). (f) Water drop, mode $n = 4$ ($R = 5.2$ mm, $f = 17.8$ Hz). (g) Water drop, mode $n = 5$ ($R = 8.6$ mm, $f = 14.3$ Hz). (h) Water drop, mode $n = 6$ ($R = 6.1$ mm, $f = 30.9$ Hz).

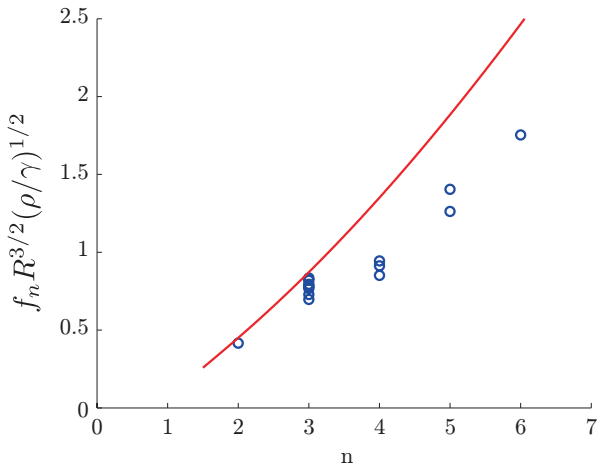

Figure 8.5: The frequency measured for faceted drops as shown in the images of figure 8.4. Each data point ○, corresponds to one water drop measurement. The red solid line is the prediction by Rayleigh and Lamb, eq. (8.1).

8.3.2 High viscosity drops

In this section the viscosity of the drop is increased to investigate whether damping of the inner drop flow indeed suppresses star oscillations. Experiments shown in this section are carried out with liquid drops of water-glycerine mixture ($\eta_{high} \sim 60$ cP). Again the drop size R and flow rate Q are varied to determine the instability threshold for drop oscillations. The result are included in Fig. 8.3. The data points for large liquid viscosity are indicated with red and green squares (□,□), to make a distinction with the water drop data. For the green squared data points, a chimney instability is observed, for which an air bubble pierces through the center of the drop. This is shown in Fig. 8.6b. These violent dynamics result in a detachment of the drop from the needle. The size of the drop could therefore only be determined from a drop in levitated state.

Comparing the threshold of high viscosity drops with water drops, we observe a clear increase of the threshold. However, the dependence on viscosity is relatively weak, given that the liquid viscosity was increased by a factor ~ 60. By contrast, the dynamics is strongly affected by the liquid viscosity. While the oscillations of water drops at threshold is chaotic and non-axisymmetric, the viscous drops only display axisymmetric oscillations: we observe clear 'breathing' modes (Fig. 8.4b), for which the levitated drop remains circular in top view while oscillating. The large viscosity of the liquid drop apparently damps all higher mode oscillations and the

formation of star-drops is completely suppressed. A more detailed picture illustrating this dynamics is shown in figure 8.6a. Consecutive snapshots (top row) all depict circular drops and a space-time diagram of the drop edge illustrates the radial oscillating motion. This regular dynamics makes it relatively easy to measure the main

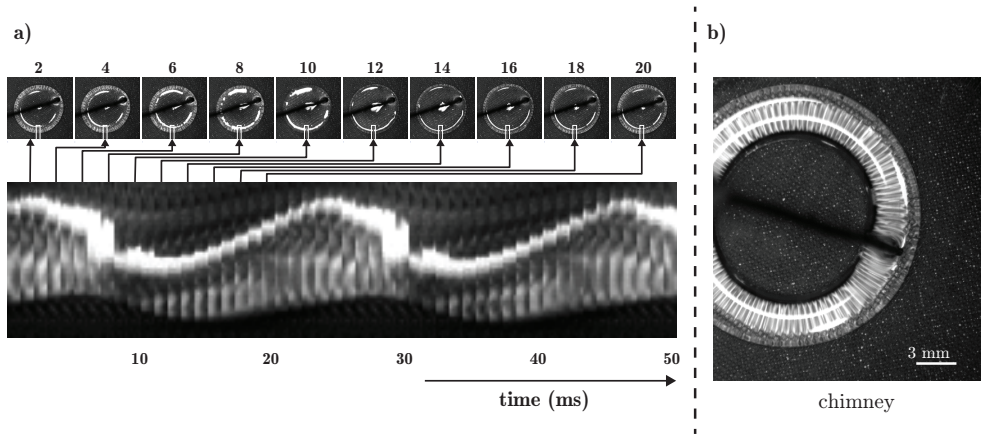

Figure 8.6: (a) Top row: an image sequence of the breathing mode oscillation of a large-viscosity drop (water glycerine, ~ 60 cP). As the oscillation amplitude is rather small, a space-time diagram is shown as well, which is built from slices similar to the white boxes indicated in the images. (b) For larger drop sizes we observe the formation of a chimney.

oscillation frequency for all data along the threshold curve (see Fig. 8.7). Note that in this measurement the frequency therefore is a function of $R(Q_t)$. Hence, small radius in this figure automatically also means relative large flow rate Q_t and vice versa (see Fig. 8.3).

Apart from very contrasting shape deformations, also the measured oscillation frequencies are different from water drops.

Frequencies for high viscosity drops are higher, by a factor two or more, than the lowest mode (n=2) of the *inviscid* Rayleigh Lamb frequency for a drop of the same size (see solid line in Fig. 8.7). One possible interpretation is that the gas flow and the liquid flow act as a coupled dynamic system that oscillates. In case of water this driving directly leads to star oscillations well described by eq. 8.1. However, viscosity suppresses or affects star oscillations in high viscosity drops. As a result one essentially observes the driving frequency that only weakly depends on drop size. Thus, although the dynamics changes, the coupling of the flow in the gas layer with the inner drop flow is still present and results in oscillations.

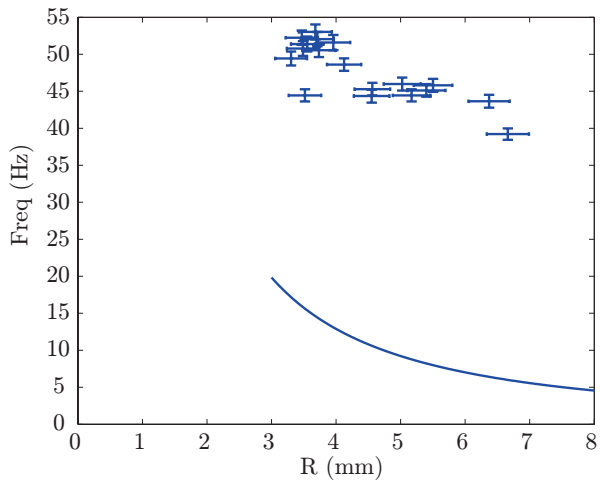

Figure 8.7: Measured oscillation frequency at threshold for high viscous drops (see Fig. 8.3). The blue solid line represents the prediction, for the lowest oscillation mode (n=2), by the *inviscid* theory of Rayleigh and Lamb, eq. (8.1).

Finally, we again observe chimneys when the drop size becomes too large, $R \approx$ 8 mm (see right panel of Fig. 8.6). Since the capillary length for the used water-glycerine mixture is, $\ell_c \sim 2.3$ mm, the chimney occurs at about $\sim 3.5\ell_c$. This is consistent with earlier experiments on water drops [19] and theory [7] for which the critical radius $R_c \approx 4.0\ell_c$ (R_c for the water-glycerine mixture is indicated by the red dotted line in Fig. 8.3)

8.4 Discussion

The levitation of drops on an air cushion is studied experimentally with high speed imaging. Contrarily to Leidenfrost drops, which float on their own vapor, the air is injected from below through a porous medium. Yet, dynamics is very similar. Drops either have stable shapes, oscillate or display a 'chimney' instability for which a gas pocket breaks through the drop. Hence, it is verified that the phenomenon of star oscillations does not require any thermal driving, contrarily to previous suggestions [14]. Not only chaotic oscillations but also distinct oscillation modes from $n = 2$ to $n = 6$ are observed for water drops. This confirms the preliminary experimental observation [6] that the origin of drop oscillations are purely governed by fluid dynamics.

Our results show that for both high-viscosity and low-viscosity drops, the thresh-

old flow rate continuously increases when decreasing the drop size. At very low Q, however, there is a maximum drop size for which the chimney instability sets in, as predicted by Snoeijer et al. [7]. The trends are very similar for both viscosities, but the threshold is slightly higher at high viscosity. However, this dependence on viscosity is relatively weak in our experiments, since the viscosity was increased by a factor 60. By contrast, the drop dynamics *is* strongly influenced by viscosity. Non-axisymmetric modes and chaotic oscillations could be observed near threshold in oscillating water drops, while in the high viscosity case, *only* the 'breathing' mode is observed. From these oscillatory axisymmetric modes we can infer that the breaking of the azimuthal symmetry is not the origin of the spontaneous appearance of oscillations.

The picture that emerges is that the oscillations appear due to an instability of the coupled system of the lubricating gas flow and the deformable drop. Once the oscillations appear, 'stars' naturally develop as a parametric instability for low-viscosity drops, in a way similar to water drops placed on an oscillating plate [26]. At higher viscosity, the star formation is suppressed by viscous damping and only axisymmetric modes appear. This is similar for the onset of Faraday waves, induced by periodic forcing of a horizontal free-surface [17]. Indeed, a large viscosity suppresses the appearance of the parametric instability that leads to Faraday waves. We therefore propose that faceted star shapes are a result of parametric excitation that can only appear a sufficiently small damping.

The exact mechanism that leads to the oscillation remains to be identified. Interestingly, the Reynolds number for these high viscosity drops are relatively small $Re \sim 0.1RfR\rho/\eta \approx 1$ (where we estimate the oscillation amplitude as 10% of R) and still spontaneous oscillations are observed above a threshold radius and gas flow rate. Previous numerical simulations based on Stokes flow for both the drop and the gas displayed no oscillations [7]. This raises the question of whether oscillations indeed cease to exist when further reducing the Reynolds number, i.e. by increasing the liquid viscosity. It will be a challenge to investigate this regime experimentally due to practical difficulties of working with such a highly viscous liquid.

References

[1] J.G. Leidenfrost, *De Aquae Communis Nonnullis Qualitatibus Tractatus* (Duisburg on Rhine, 1756).

[2] J.C. Burton, A.L. Sharpe, R.C.A. van der Veen, A. Franco and S.R. Nagel, *Geometry of the Vapor Layer Under a Leidenfrost Drop*, Phys. Rev. Lett., **109**, 074301 (2012).

[3] H. Linke, B.J. Alemán, L.D. Melling, M.J. Taormina, M.J. Francis, C.C. Dow-Hygelund, V. Narayanan, R.P. Taylor, and A. Stout, *Self-propelled Leidenfrost droplets*, Phys. Rev. Lett. **96**, 154502 (2006).

[4] G. Lagubeau, M. Le Merrer, C. Clanet and D. Quéré, *Leidenfrost on a ratchet*, Nat. Phys. **7**, 395-398 (2011).

[5] A. Wurger, *Leidenfrost Gas Ratchets Driven by Thermal Creep*, Phys. Rev. Lett. **107**, 164502 (2011).

[6] P. Brunet and J.H. Snoeijer, *Star drops formed by periodic excitation and on an air cushion A short review* Eur. Phys. J. Spec. Top. **192**, 207-226 (2011).

[7] J.H. Snoeijer, P. Brunet, J. Eggers, *Maximum size of drops levitated by a air cushion*, Phys. Rev. E **79**,. 036307 (2009).

[8] K. Adachi and R. Takaki, *Vibration of a flattened drop. I. Observation*, J. Phys. Soc. Jap. **53**, 4184-4191 (1984).

[9] R.Takaki and K. Adachi, *Vibration of a Flattened Drop. II. Normal Mode Analysis* J. Phys. Soc. Jap. **54**, 2462-2469 (1985).

[10] N.J. Holter and W.R. Glasscock, *Vibrations of evaporating liquid drops*, J. Acous. Soc. Am. **24**, 682-686 (1952).

[11] D.E. Strier, A.A. Duarte, H. Ferrari and G.B. Mindlin, *Nitrogen stars: morphogenesis of a liquid drop*, Physica A **283**, 261-266 (2000).

[12] A. Snezhko, E. Ben Jacob and I.S. Aranson, *Pulsating-gliding transition in the dynamics of levitating liquid nitrogen droplets*, New J. Phys. **10**, 043034 (2008).

[13] M.A. Goldshtick, V.M. Khanin and V.G. Ligai, *A liquid drop on an air cushion as an analogue of Leidenfrost boiling*, J. Fluid Mech. **166**, 1-20 (1986).

[14] N. Tokugawa and R. Takaki, *Mechanism of self-induced vibration of a liquid drop based on the surface tension fluctuation*, J. Phys. Soc. Jap. **63**, 1758-1768 (1994).

[15] H. Lamb, Hydrodynamics *Cambridge University Press, 6th edition, 1957*

[16] Pozrikidis, C. Introduction to theoretical and computational fluid dynamics *Oxford University Press, 1997*

[17] K. Kumar and L.S. Tuckerman, *Parametric instability of the interface between two fluids*, J. Fluid Mech. **279**, (1994) 49-68.

[18] L. Duchemin, J.R. Lister and U. Lange, *Static shapes of levitated viscous drops*, J. Fluid Mech. **533**, 161-170 (2005).

[19] A.-L. Biance, C. Clanet and D. Quéré, *Leidenfrost drops*, Phys. Fluids **15**, (2003) 1632-1637.

[20] X. Noblin, A. Buguin and F. Brochard-Wyart, *Triplon modes of puddles*, Phys. Rev. Lett **94**, (2005) 166102.

[21] M. Okada and M. Okada, *Observation of the shape of a water drop on an oscillating Teflon plate*, Exp. Fluids **41**, (2006) 789-802.

[22] C.L. Shen, W.J. Xie and B. Wei, *Parametrically excited sectorial oscillation of liquid drops floating in ultrasound*, Phys. Rev. E **81**, (2010) 046305.

[23] Y. Fautrelle, J. Etay and S. Daugan, *Free-surface horizontal waves generated by low-frequency alternating magnetic fields*, J. Fluid Mech. **527**, (2005) 285-301.

[24] M. Papoular and C. Parayre, *Gaz-film levitated liquids: shape fluctuations of viscous drops*, Phys. Rev. Lett. **78**, (1997) 2120-2123.

[25] M. Perez, Y. Brechet, L. Salvo, M. Papoular and M. Suery, *Oscillation of liquid drops under gravity: Influence of shape on the resonance frequency*, Europhys. Lett. **47**, (1999) 189-195.

[26] N. Yoshiyasu, K. Matsuda and R. Takaki, *Self-induced vibration of a water drop placed on an oscillating plate*, J. Phys. Soc. Jap. **65**, (1996) 2068-2071.

[27] I.A. Larmour,S.E.J. Bell and G.C. Saunders, *Remarkably Simple Fabrication of Superhydrophobic Surfaces Using Electroless Galvanic Deposition*, Angewandte Chemie,**119**, 10 (2007), 1521-3757.

9 Conclusions and outlook

When a fluid displaces another immiscible fluid across a solid surface there is a contact line involved that should move as well. This is a very common phenomenon in both nature, such as water drops sliding down a leaf, and industrial processes in for example printing, coating and immersion lithography. As in many physical phenomena, boundary conditions can strongly affect the macroscopic fluid dynamics. This is particularly true for the contact line: the triple phase line can dictate the hydrodynamics up to macroscopic scales.

The work presented in this thesis is part of the FOM Industrial Partnership Program "Contact line control during wetting and dewetting" in collaboration with ASML and Océ. This dissertation focusses on fast contact line motion and related phenomena both from a fundamental and industrial perspective. In particular we concentrate on questions relevant for ASML, related to Immersion Lithography systems. Essentially the chapters can be divided into two parts: contact line dynamics in the context of immersion lithography (Chapter 2-5) and droplet spreading at very short time scales (Chapter 6-7). Apart from the studies on phenomena close to the contact line, also oscillations of levitated drops are investigated in the final chapter, Chapter 8.

In Chap. 2, we have investigated receding contact line dynamics in two different systems. We first provided a detailed comparison between sliding drops and the moving contact line in a system that resembles an Immersion Lithography environment. Using high speed cameras and detailed imaging of the receding contact line, we have characterised the contact line dynamics by dynamic contact angle, corner angle and

tip radius of curvature, as a function of sliding velocity. Despite the differences in driving (gravity or motion imposed by a motor) and liquids (water or silicon oil), we found very similar dynamics in both systems. For the dynamic contact angle, a clear deviation from the standard Cox-Voinov relation is observed, once the receding contact line becomes corner like. This arises when the tip becomes very sharp, with a curvature that increases exponentially with velocity. Comparison of the experimental data with corner models by Limat and co-workers [1–4] show good agreement. However there is a remarkable quantitative difference observed between water and silicon oil. For silicon oil, the observation could be fully explained by a model based on the Cox-Voinov theory. For water, the dependence of the dynamic contact angle on velocity is stronger by a factor 2, which cannot be explained by varying the microscopic parameter. This factor 2 is very important in the context of immersion lithography: the critical speed at which liquid is lost is lower by a factor 2 than expected. At present there is no full explanation for this effect.

Results from the former chapter imply, that the corner formation is a generic mechanism for fast moving receding contact lines. Interestingly such a shape change effectively increases the critical contact line velocity. It is however not only high velocities that could affect the stability of the contact line but also the steadiness of motion. To get to know more about unsteady contact line motion, we have studied unsteady effects in Chap. 3, using the quasi-steady assumption. In this assumption, the contact line is only characterized by its position and the instantaneous speed with respect to the substrate. We carried out experiments with different droplet volumes, needle heights and accelerations. Indeed for accelerations up to 0.5 m/s^2, the maximum acceleration used in these experiments, the dynamic contact angle does not change and the quasi-steady assumption still holds. However there is a significant difference in critical velocity with droplet volume and needle height. The results imply that the outer geometry sets the critical velocity which is beyond the standard Cox-Voinov prediction. From Eggers, Snoeijer and co-workers [5–8] it is known that matching of the inner and outer scale of the liquid flow will determine the transition towards liquid deposition, i.e. critical velocity. Here also, results suggest that the outer drop shape determines whether a drop remains stable or reaches a state where it leaves liquid behind on the substrate. This qualitative agreement emphasizes the strong connection between local microscopic contact line dynamics that needs to match an outer scale flow. Essentially, both boundary conditions are important in determining the critical velocity of dewetting. For future research it would be interesting to extend this study and explore regimes of higher accelerations. Secondly, this approach could well be used to study the effect of outer flow on contact line dynamics.

Once a contact line is forced to move above the critical speed, liquid is deposited in the form of droplets on the substrate. In Chapter 4, we have characterized this instability experimentally using high speed imaging with the aim of understanding the size of the emitted droplets. The dewetting corner emits a thin rivulet above the critical speed. The size of the rivulet turns out to increase continuously with sliding velocity and approaches vanishing sizes close to the critical velocity. As a result the corner is connected with a slender tail, that finally breaks-up into droplets of size R and separation distance λ. By rescaling our data, we have found that both R and λ are determined by the rivulet width w. A first thought about instabilities and surface tension brought us to a comparison with Rayleigh-Plateau instability. However, we found that the measured separation distance λ between drops is significantly larger than predicted for the instability of rivulets [9]. A similar result was observed by Diez et al.[10] who studied the break-up of finite-sized rivulets. A closer look at the break-up process revealed that break-up always occurs at the tip and is not very similar to a pure growing instability as in Rayleigh-Plateau break-up. This is why the drops are slightly larger than expected, although their size is still proportional to the rivulet width. After pinch-off the droplets are ellipsoidal instead of circular, which can be explained from the contact line dynamics, i.e. receding contact angle in the direction of motion and advancing contact angle in the direction perpendicular to it. The next step is to model such dynamics, including contact line motion. This could lead to a more complete picture of the exact break-up mechanism and exact predictions of the resulting droplet sizes.

In the former chapters we have studied drop deposition on a substrate. When these sessile drops on a substrate collide with an advancing meniscus, bubble entrainment might occur. In Chapter 5, we have investigated this situation since the bubble size and understanding of the underlying bubble formation mechanism is highly relevant for Immersion Lithography. We identified and explain two different mechanisms for bubble entrapment, which result in very distinct types of bubbles. Depending on the impact height h above the moving contact line, i.e. the location of the first single contact point, coalescence could result in: i) floating bubbles if $h = 0$, and ii) sticking bubbles if $h > 0$. The first bubble type (i) results from the entrapment of a lubricating air film. When the distance between the impacting drop and a meniscus decreases, a lubricating pressure builds up in the separating and lubricating air gap. Depending on the speed and size of the impacting drop this pressure opposes either the capillary pressure (capillary regime) or the inertial pressure (inertial regime) inside the liquid drop. In case of the experiments shown for droplet-meniscus collision, only the capillary regime is explored. We have found an increase of bubble volume V_{bub} with capillary number ($Ca = U\eta_g/\gamma$; impact velocity) and impacting drop volume

V_{drop}, consistent with scaling arguments: $V_{bub}/V_{drop} \sim Ca$. The second bubble type, (ii) sticking bubbles, appear to be independent of impact velocity and are attached to the substrate. We have shown that the entrapment mechanism is, due to the impact height $h > 0$ condition, very reminiscent of bubbles formed in axisymmetric bubble pinch-off processes. Due to the fast coalescence process, the impact velocity actually has no influence on the bubble formation.

Interestingly, the same mechanism for bubble entrapment is relevant for a drop impacting on a solid wall – in which case the lubricating air film is trapped inside the drop. For this drop impact, we were able to explain both the capillary regime and inertial regime. At low speeds the bubble size increases with velocity while at high speeds the bubble size decreases with velocity. This result is verified experimentally and numerically. Remarkably, without details of film drainage or coalescence dynamics, bubble sizes can be predicted, including a *maximum* bubble entrainment in the crossover between the capillary regime and inertial regime. The results are highly relevant for industry such as inkjet printing and immersion lithography, where bubbles can be advantageous or disadvantageous. Further research is necessary to understand the effect of inclined impact, effect of geometry on impact, air film drainage or coalescence dynamics. For printing it would be interesting to extend the study to impact on porous media to further investigate the build up of lubricating pressures.

In the field of contact line motion, droplet spreading is a very common and wide studied phenomenon. However, it was only less than a decade ago that also the short time dynamics of drop spreading was first investigated [11, 12]. With high speed bottom view imaging we have experimentally accessed previously unexplored length- and time-scales of the short time spreading dynamics of low viscous drops (Chap. 6) and viscous drops (Chap. 7) on wetting and partially wetting substrates. We have studied the case of spreading drops with approximately zero impact velocity. In Chapter 6, we have shown that the initial spreading dynamics is not affected by the wetting characteristics of the substrate. For the considered wettabilities ($\theta_{eq} \approx 0°$, $65°$ and $115°$) the radius of wetted area r, all grow as $r \sim t^{1/2}$, independent of substrate wettability. This contrasts previous work [12], for which a wettability-dependent exponent was reported. The improved resolution of our experiment, however, revealed an initial regime with a spreading exponent of 1/2. This dynamics can be explained from a balance between inertial pressure in the liquid and the capillary driving forces, similar to the coalescence of two freely suspended liquid drops. Only at radii of $r/R \sim 0.2$, the spreading dynamics changes and shows different behaviour for different equilibrium contact angle θ_{eq}. Detailed and valuable information about first contact was obtained with Molecular Dynamics simulations (MD).

To better understand the surprising result of wettability independent dynamics of

drop spreading we extended our research to more viscous drops. In Chapter 7, we have supplemented our experimental setup with simultaneous high speed side view imaging. This enabled us to access spreading dynamics over 6 decades of time resolution. The observed dynamics is different from the low-viscosity spreading. Instead of a constant power-law exponent we found a continuous decreasing exponent. At short times, we did not find a clear dependence on substrate wettability ($t < 10^{-3}$ s). Once again this is consistent with the coalescence of two freely suspended viscous drops, for which the spreading velocity slowly decreases with time. However the velocity does not simply scale with $1/\eta$, as also observed by Carlson [13]. Due to the strong analogy with coalescence at short times (pre-factors and slowly decreasing spreading velocity) we suggest that the results can be explained from the influence of the outer fluid. The necessary prefactor (that change of viscosity) covers a slightly wider range than predicted from theory, but is of similar order of magnitude. It thus seems that the confinement of the air near the contact line has a major effect, but the details have remained unresolved. In a way comparable to the present experiments, the speed dependence on liquid viscosity was found much weaker than $1/\eta$ by Marchand et al.[14]. Also, impact experiments were collapsed using a $1/\sqrt{\eta}$ speed-dependence by de Ruiter et al. [15].

It still remains an open question why there exists such a quantitative analogy between spreading dynamics and coalescence of drops. Namely, this suggests that the presence of the substrate does not play a role in this regime. A possible explanation is that the singular character of first contact effectively affects the slip over the substrate.

In the final chapter (Chapter 8) we have experimentally studied the dynamics of drops levitated by a prescribed gas flow. This situation is very similar to Leidenfrost drops but then at room temperatures, i.e. the phenomenon no longer relies on evaporation effects. The drops levitate on a lubricating air cushion, that is supplied through a porous medium. In this system, water drops behave very similar to water drops in Leidenfrost state. Above threshold conditions which depends on the drop size and the imposed air flow rate, we observe chaotic and distinct star oscillations (modes from $n = 2$ to $n = 6$) which are in correspondence with Rayleigh-Lamb equation. Under the assumption that the complete system is at room temperature, these results suggest that oscillations are not induced by thermal effects but purely by hydrodynamics. To investigate the effect of liquid viscosity on the instability, we also increase the viscosity of the liquid (factor 60). The instability threshold displays a similar trend and only weakly increases. Remarkably, the drop dynamics *is* strongly influenced by viscosity. Instead of surface modes, only axi-symmetric 'breathing' modes are observed close to threshold. This shows that the breaking of the azimuthal axi-symmetry is not the origin of the oscillatory instability. As predicted by theory,

chimney instabilities are observed for large droplets [16]. Here, the key challenge remains to explain the origin of the oscillations. Our results suggest that oscillations appear due to a coupling of the lubricating gas flow with the liquid flow inside the droplet. Once oscillations appear, stars appear naturally by parametric instability for low viscous drops.

References

[1] L. Limat and H. A. Stone, "Three-dimensional lubrication model of a contact line corner singularity", Europhys. Lett. **65**, 365 (2004).

[2] H. A. Stone, L. Limat, S. K. Wilson, J. M. Flesselles, and T. Podgorski, "Corner singularity of a contact line moving on a solid substrate", C. R. Physique **3**, 103–110 (2002).

[3] J. H. Snoeijer, E. Rio, N. Le Grand, and L. Limat, "Self-similar flow and contact line geometry at the rear of cornered drops", Phys. Fluids **17**, 072101 (2005).

[4] J. Snoeijer, N. Le Grand, L. Limat, H. A. Stone, and J. Eggers, "Cornered drop and rivulets", Phys. Fluids **19**, 042104 (2007).

[5] J. Eggers, "Hydrodynamic theory of forced dewetting", Phys. Rev. Lett. **93**, 094502 (2004).

[6] J. H. Snoeijer, B. Andreotti, G. Delon, and M. Fermigier, "Relaxation of a dewetting contact line part 1: A full-scale hydrodynamic calculation", J. Fluid Mech. **579**, 63 (2007).

[7] G. Delon, M. Fermigier, J. H. Snoeijer, and B. Andreotti, "Relaxation of a dewetting contact line part 2: Experiments", J. Fluid Mech. **604**, 55 (2008).

[8] J. Ziegler, J. H. Snoeijer, and J. Eggers, "Film transitions of receding contact lines", Eur. Phys. J. Special Topics **166**, 177 (2009).

[9] J. A. Diez, A. G. González, and L. Kondic, "On the breakup of fluid rivulets", Physics of Fluids **21**, 082105 (2009).

[10] A. G. González, J. Diez, R. Gratton, and J. Gomba, "Rupture of a fluid strip under partial wetting conditions", EPL (Europhysics Letters) **77**, 44001 (2007).

[11] A.-L. Biance, C. Clanet, and D. Quéré, "First steps in the spreading of a liquid droplet", Phys. Rev. E **69**, 016301 (2004).

[12] J. C. Bird, S. Mandre, and H. A. Stone, "Short-time dynamics of partial wetting", Phys. Rev. Lett. **100**, 234501 (2008).

[13] A. Carlson, G. Bellani, and G. Amberg, "Universality in dynamic wetting dominated by contact-line friction", Phys. Rev. E **85**, 045302 (2012).

[14] A. Marchand, T. S. Chan, J. H. Snoeijer, and B. Andreotti, "Air entrainment by contact lines of a solid plate plunged into a viscous fluid", Phys. Rev. Lett. **108**, 204501 (2012).

[15] J. de Ruiter, J. M. Oh, D. van den Ende, and F. Mugele, "Dynamics of collapse of air films in drop impact", Phys. Rev. Lett. **108**, 074505 (2012).

[16] J. H. Snoeijer, P. Brunet, and J. Eggers, "Maximum size of drops levitated by an air cushion", Phys. Rev. E **79**, 036307 (2009).

Summary

Wetting and dewetting are important phenomena in both nature and applications. In this thesis we studied fast contact line motion as part of the FOM Industrial Partnership Program "Contact line control during wetting and dewetting" in collaboration with ASML and Océ. In particular we concentrate on questions relevant for ASML, in the context of immersion lithography systems.

In chapter 2 and 3, we have studied receding contact line motion below the critical velocity. First we compared the cases of sliding drops and immersion lithography systems, and we have showed that the dynamics is very similar. Results imply that a corner formation is a generic mechanism for fast moving receding contact lines. However quantitatively there are clear differences which result in unexpected critical speeds. Extension of the investigation of critical velocities, show that there is a dependence on drop volume and fixation height. Secondly for small accelerations, ~ 0.5 m/s^2 (which is the maximum used in the experiments), unsteady contact line dynamics appeared to be well described by a quasi-steady approach.

Once the critical velocity is exceeded, the receding contact line becomes unstable. In chapter 4, we have investigated this instability process. Above the critical speed, a rivulet is ejected from the corner structure which continuously increases in width as a function of velocity. We show that this rivulet breaks up into smaller droplets that move with the substrate after pinch-off. The distance between the sessile drops and the size of the droplets behave proportional to the width of the rivulet. The picture that emerges is that the rivulet is an alternative solution to the stable corner structure, in which the net outflux (in the moving reference frame) is no longer zero. A rivulet is ejected and the width depends on the velocity of the receding contact line. Then an instability occurs which results in the topological change of the rivulet into droplets.

In chapter 5, we experimentally show two types of bubble entrainment during the collision of a drop and an advancing meniscus. The resulting size and type depends on the location where the drop first comes into contact with the meniscus. If this first contact happens at the substrate, i.e. at zero impact height, floating bubbles can form as a result of the entrapment of a lubricating air sheet. Using scaling analysis, we predicted the size as a function of impacting velocity and drop size. In case

the first single contact takes place at a position above the moving contact line, a sticking bubble is formed by a process significantly faster than the investigated impact velocities. Typical bubble sizes found have radii $\sim 10\mu$m. This research is extended with a study on bubble entrainment by impact of a drop on a solid substrate. With an experimental, theoretical and numerical approach we show that there exists two regime with a maximum entrapped bubble size in the crossover.

Apart from forced contact line motion, we also studied fast contact line motion in the simple axisymmetric system of drops naturally spreading on (partial) wetting substrates after a first contact. In Chapter 6, we first studied the short time spreading dynamics of low viscosity drops (water) using experiments and Molecular Dynamic simulations. We show that immediately after contact (when the drop is still spherical) the spreading is independent of substrate characteristics. Independent of equilibrium contact angle, the radius of wetted area grows with the square root of time. Only at later times, the wettability effect becomes apparent. Surprisingly, the results suggest a close analogy (qualitative and quantitative) with the coalescence of freely suspended drops. To further understand this analogy, we carried out experiments with more viscous liquid in chapter 7. Also in this case the spreading after contact (fast spreading regime), no clear wettability effects are observed. It turns out that also in the viscous case the analogy with coalescence is remarkably accurate. However the dependence on viscosity is slightly different. It seems that the confinement of the air near the contact line has a major effect, but the details have remained unresolved

In Chapter 8, we have investigated drops levitated by a prescribed air flow. Above a threshold flow and drop size, instabilities finally arise. For water, we have shown experimentally that the oscillation frequencies and observed star-oscillations are alike drop instabilities in a Leidenfrost state, for which a drop levitates on its own vapor above a hot substrate. To investigate the effect of viscosity, we repeated the experiments with drops of water/glycerine mixture, 60 times more viscous than water. Only a weak increase of the threshold instability is observed, while the oscillation dynamics is clearly different. At threshold only axisymmetric oscillations are observed with oscillation frequencies almost independent of drop radius. Our results could exclude two possible mechanisms behind the formation of star drops. First, thermal effects are presumably not needed for instabilities to occur, and second, the breaking of axisymmetry is not the origin of the spontaneous appearance of oscillations.

Samenvatting

Bevochting van vaste oppervlakken door vloeistoffen speelt een grote rol, zowel in de natuur als in industriële toepassingen. In dergelijke processen speelt de scheidslijn tussen verschillende fases, ook wel de contactlijn genoemd, een grote rol. In dit proefschrift hebben we de dynamica van snelle contactlijnen onderzocht in het kader van het FOM Industrial Partnership Program " Contactlijncontrole tijdens bevochtiging en ontvochtiging" in samenwerking met ASML en Océ. Hierbij hebben we ons met name gericht op vragen relevant voor ASML, in de context van immersie lithografie systemen.

In hoofdstuk 2 en 3, bestuderen we terugtrekkende contactlijnen die voortbewegen met snelheden onder de kritische snelheid. Dit hebben we onderzocht voor zowel glijdende druppels van siliconen olie als voor immersie lithografie systemen gebaseerd op water. We laten zien dat beide systemen soortgelijke dynamica vertonen ondanks het verschil in vloeistof en systeem. De terugtrekkende contactlijn vertoond een generieke oplossing in de vorm van een puntvormige staart. De dynamica van de glijdende druppel van grote viscositeit is te beschrijven met standaard Cox-Voinov theorie, terwijl voor water een sterker effect wordt waargenomen. Voor water neemt de dynamische contacthoek twee maal zo snel af, wat niet te verklaren valt met typische microscopische lengteschalen in the Cox-Voinov theorie. Mogelijk zou dit beïnvloed kunnen zijn door inertie aangezien de Reynoldsgetallen van de orde 100 zijn. Aangezien acceleraties en veranderlijke bewegingen een grote rol spelen in immersie lithografie systemen, bestuderen we in hoofdstuk 3 veranderlijk terugtrekkende contactlijnen. Ondanks de lage viscositeit van water vinden we dat het gedrag van accelererende contactlijnen hetzelfde is (tot 0.5 m/s^2, de maximum acceleratie gebruikt in deze experimenten) als contactlijnbeweging op constante snelheid en kan beschreven worden met een 'quasi-onveranderelijke' beschrijving. Opmerkelijk is, dat zowel het volume van de druppel als de afstand van de naald tot het substraat, de vlieghoogte, een grote invloed blijkt te hebben op de kritische snelheid. Een groter volume of lagere vlieghoogte resulteren beiden in een lagere kritische snelheid waarop vloeistof depositie plaatsvindt. Geometrie zou hier een belangrijke rol kunnen spelen.

Wanneer de kritische snelheid wordt overschreden, wordt de teruglopende contactlijn instabiel. In hoofdstuk 4, bestudeerden we dit instabiele proces. In dit geval ontstaat uit de puntvormige staart een uitstroom van vloeistof. We laten zien dat de uitstroom een breedte heeft die toeneemt als functie van de snelheid. De stroom blijft echter niet stabiel en breekt op in separate druppels die vervolgens meebewegen met het substraat. De afstand tussen deze afgebroken druppels en de druppelgrootte staan in verhouding tot de breedte van de stroom uit de staart. De interpretatie van de resultaten is dat het stroompje een alternatieve oplossing is voor de stabiele puntvorm van de druppelstaart, waarin de netto uitstroom (in het bewegende referentieframe van de druppel) niet langer nul is. Een kleine hoeveelheid vloeistof, bepaald door de mate van overschrijding van de kritische snelheid, stroomt met constant debiet uit de druppel. De breedte van de uitstroom is dus afhankelijk van de snelheid van de terugtrekkende contactlijn. Dit stroompje breekt vervolgens op in druppeltjes. De grootte van deze druppels is proportioneel met de breedte van het stroompje, en kan heel klein worden vlakbij de kritische snelheid.

In hoofdstuk 5, identificeren we twee mechanismes voor het invangen van bellen in een vloeistof. Indien een druppel meebeweegt met een substraat en botst met een meniscus, kan tijdens 'coalescentie' een bel worden gevormd. De resulterende grootte en type is afhankelijk van de hoogte van het eerste contact ten opzichte van het substraat. Als het eerste contact plaatsvindt op de contactlijn, kan een sferische bel worden gevormd die vrij rondzweeft in de vloeistof. De grootte van de bel neemt toe met de botssnelheid en inkomende druppelgrootte. Dit valt te verklaren aan de hand van het 'smeereffect' van de tussenliggende luchtlaag – de visceuze luchtstroom kan niet direct ontsnappen tussen de druppel en de meniscus en wordt ingesloten tijdens coalescentie. Met schalingsanalyse kunnen we de belgrootte als functie van de snelheid en druppelgrootte voorspellen. Als het eerste contact plaatsvindt boven de contactlijn kan nog steeds hetzelfde effect optreden, echter vindt ook een ander type luchtinvanging plaats. Een vloeistof/gas oppervlak beweegt in dit geval naar het substraat toe. De configuratie die ontstaat, breekt waarbij een bel op het substraat ontstaat van de orde 10μm. Dit proces is aanzienlijk sneller dan de onderzochte botsingssnelheid en is daarom onafhankelijk van de botssnelheid. Dit onderzoek is uitgebreid met een studie naar het invangen van bellen tijdens de botsing van druppels met een vlak substraat. Met experimentele, theoretische en numerieke aanpak laten we zien dat er twee regimes bestaan met een maximale ingesloten luchtbelgrootte in het overgangsgebied van de twee regimes.

Naast contactlijn-dynamica in immersie lithografie georiënteerde systemen hebben we ook onderzoek gedaan naar snelle contactlijnbewegingen in een eenvoudig axisymmetrisch systeem: de spreiding van druppels op gecoate substraten. In hoofdstuk

6, hebben we de spreiding van laag viskeuze druppels (water) onderzocht met behulp van zowel experimenten, als computer simulaties op basis van moleculaire dynamica. We laten zien dat kort na contact (als de druppel nog bolvormig is) de bevochtiging van het substraat onafhankelijk is van hoe hydrofiel het substraat is. Ondanks een grote variatie van evenwichtscontacthoeken ($\theta_{eq} \approx 0^\circ, 65^\circ, 115^\circ$) nemen we voor de vroegste momenten van spreiding eenzelfde dynamica waar: de straal van het bevochtigde gebied groeit als $r \sim t^{1/2}$. Alleen op latere tijdstippen, wordt de invloed van de evenwichtscontacthoek zichtbaar. Verrassend is dat de resultaten een grote overeenkomst vertonen (kwalitatief en kwantitatief) met de coalescentie van sferische druppels. Om meer inzicht te krijgen in het fenomeen en de invloed van dissipatie, hebben we ook experimenten uitgevoerd met meer viskeuze vloeistoffen (water-glycerine mengsels). Dit onderzoek presenteren we in hoofdstuk 7. Ook in dit geval zien we in de dynamica kort na het eerste contact geen duidelijke invloed van de hydrofiliteit van het substraat. Het blijkt dat ook voor viskeuze druppels een sterke overeenkomst met coalescentie zichtbaar is. Echter, de afhankelijkheid van viscositeit is sterker dan verwacht op basis van coalescentie theorie. Dit duidt op een sterke invloed van de stroming in de lucht, maar een gedetailleerde beschrijving van dit effect ontbreekt nog.

In hoofdstuk 8, bestuderen we de stabiliteit van druppels die zweven op een luchtstroom. Boven een drempelwaarde van debiet en druppelgrootte, ontstaan instabiliteiten. In deze experimentele studie laten we zien dat de oscillatiefrequenties en waargenomen ster-oscillaties vergelijkbaar zijn met Leidenfrost druppels, die zweven boven een heet oppervlak. Om het effect van viscositeit te onderzoeken, hebben we de experimenten herhaald met druppels bestaande uit een mengsel van water en glycerine, dat 60 keer meer viskeus is dan water. We meten slechts een kleine verhoging van de drempelwaardes voor instabiliteiten, terwijl de oscillatie dynamica duidelijk verandert. Op de drempelwaarden vinden we enkel axi-symmetrische trillingen. Hieruit blijkt dat het breken van de azimutale symmetrie niet de oorsprong is van het spontaan ontstaan van trillingen.

Acknowledgements

All the work presented in this thesis could not have been done without help and support of many people around me. Here I would like to thank everybody and mention some in particular.

First, I would like to thank my promotor Detlef for giving me the opportunity to work in such an excellent group. It is a great and challenging environment with everything available for beautiful research. For this I would of course also like to thank my direct supervisor Jacco. Jacco, you have been the most important person in this work. The first years felt as a warm welcome, when you and Danielle invited me to come by at home to discuss or to have a BBQ, I am very grateful for this. I also enjoyed our discussions and conversations very much. Although we did not always directly agree, we had many good discussions. I am impressed by your talent of explaining things in a comprehensive way without oversimplifying it. Your suggestions, ideas and opinions were always extremely valuable and I learned a lot from you. Thank you very much!

As the reader of this thesis knows, the research is part of a FOM industrial partnership programme (FOM-IPP). In my opinion a great idea to set up collaborations between academia and industry. Here I would like to acknowledge all members of the research programme 'Contact Line Control during Wetting and Dewetting' (CLC): FOM, which is financially supported by NWO, and the companies ASML and Océ that co-financed this programme. Many thanks also to other participants and organisers of the FOM IPP project. In particular thanks to Frieder Mugele, Dirk van de Ende, Dieter 't Mannetje, Chandra Murade and Mariska van der Weide-Grevelink from the PCF group for the support and sharing of the experimental setup.

Special thanks goes to ASML. It was always a great pleasure for me to come to Veldhoven and have an insight in such a large and high-tech company with outstanding research, good scientists and engineers. Many thanks to Ramin Badie, I would like to thank you here for all your support and help in the past years. Michel Riepen, it was a great pleasure working with you, with your enthusiasm about physics and your own view on topics, I enjoyed very much the (informal) meetings we had. During my PhD I had the luck to make a good start also due to Fabrizio Evangelista.

Later the good collaboration continued with Hein Castelijns in a project about the bubble entrapment. Fabrizio and Hein, thanks a lot!

Last year I was privileged to go to Paris for a short period, where I was hosted for one part by Philippe Brunet and Laurent Limat at Université Paris Diderot, Matière & Systèmes Complexes. Philippe thanks for guiding me around and for the nice (scientific) discussions. Laurent, thank you for the very nice discussions we had in for example Leiden, Florence and Paris. Also I am grateful for your enthusiasm about the tail break-up. The second part of my stay, was at the Laboratoire de Physique et Mécanique des Milieux Hétérogénes, ESPCI, where I worked together with Bruno Andreotti and Antonin Marchand on 'extremely slow' contact line motion. It was only a short period, but I learned many good experimental techniques and image processing methods. Bruno and Antonin, thank you very much.

It was great working with all colleagues from the group Physics of Fluids. It is always a very pleasant group to work in. During four years of PhD work, there was one team always prepared to help as well. A very good and valuable team for the whole group. Whether it is computers, experimental setups, administrative matters etc., Bas, Gert-Wim, Martin and Joanita, many thanks for all your help! I would like to thank my old housemate and officemate Álvaro, my other office mates Marlies, Wim, Laura, Claas-Willem and Henri, for the good time, nice chats and discussions. In the lab I worked together a lot with Antonin Eddi, on various topics like the drop spreading, tail break-up and inertial coalescence of sessile drops. We had good discussions on interpretation of data and ideas for experiments. Antonin, for me it was always a great pleasure working with you, thank you very much for the good collaborations. Also I would like to thank Wilco Bouwhuis, Álvaro Marín, Oscar Enríquez for the collaborations on bubbles and freezing drops.

I also had the luck to be involved in some graduation projects. Dimitrios Razis, it was great to work with you on the levitated droplets over spherical substrates. Diederik Keij, most of the time you were stationed in Veldhoven with ASML, but the meetings we had and experiments we did together were always very efficient and clear. I enjoyed the bubble project with you very much. Chapter 6 started with some interesting ideas and preliminary experiments. Many thanks to Roeland van der Veen, Matthias van de Raa and Jon Brons, for their exploratory work. Another part of my time was not spend on research but on education. I was involved in the course Physics of Fluids, taught by Jacco. It was a good experience and I enjoyed very much the corrections, tutoring, and preparations for the course with Edip Can, Ceyda Sanli and Joost Weijs.

If I checked correctly, at the moment of writing this, Shing will be travelling in Peru. Shing, conversations on contact line motion, life, travelling and all other

subjects were always very nice. Many thanks for this, and for the good collaboration.

My time in Enschede would not have been so pleasant, without the warmth, friendship and support of friends and family around me in and outside Enschede. Of course I would like to thank all flatmates of Pauperzicht. I hope there will be many reunions in the near future. Many thanks also to Joost and Tess, for the nice dinners, evenings, the introduction to climbing and support in everything. As well I would like to thank Christian, Elbert and Erik for the enjoyable and fun 'stef-stuntpiloot' evenings, and the nice years we studied together. Poi vorrei ringraziare Andrea. Andrea sei un vero amico, apprezzo sempre tanto la tua visione delle cose. Anche per te: "fammi sapere, solo due ore prima va bene". Grazie mille! Hanneke, we have been together for a part of our PhD. As someone once said: "Time is the most valuable thing that a man can spend", and I feel lucky I could spend it with you, I would like to thank you for all shared moments. Of course I also would like to thank two very close friends who will support and assist me during the defence as paranymphs. Koen and Rinke, thank you very much, I appreciate it a lot! Last, I would like to thank the most important persons in my life, my parents Herman and Cecilia, and my brother Otto. Thank you for all support, trust and confidence you give to me, no matter what I do. It is impossible to describe in words what it means to me.

Koen Winkels
Enschede, The Netherlands
January 2013

About the author

Koen Gerhardus Winkels was born on the 8th of July 1984 in Warnsveld, The Netherlands. There he grew up and attended high school at the Isendoorn College. In 2002, he graduated and started to study Applied Physics at the University of Twente. During his studies he did a minor in Biomedical Engineering and organised, with other students, an excursion to Jena and Berlin. In his masters he started exploring more parts outside the Netherlands. He went to England, to do an internship in Southampton at the Institute of Sound and Vibration Research with Prof. T. Leighton and Dr. P. Birkin. In Southampton he investigated the rise-time of Faraday waves on the wall of an acoustically excited bubble. Shortly after he went to Rome to study one semester at Università degli Studi di Roma – La Sapienza. In 2008 he obtained his MSc. degree in the group Physics of Fluids on the design and testing of a microfluidic bubble pump. Not much later he started his PhD research in the same group under supervision of Jacco Snoeijer on contact line dynamics, in collaboration with ASML. Apart from his interest in physics and fluid dynamics, he likes cycling and running very much. Especially cycling in the mountains, abroad or in good company.